NTNU
Norwegian University of
Science and Technology

# Satellite mapping of particle precipitation effects on the Antarctic middle atmosphere

Martin Lisa

Physics
Submission date: May 2011
Supervisor: Patrick Joseph Espy, IFY

Norwegian University of Science and Technology
Department of Physics

**Faculty of Natural Science and Technology**
**Department of Physics**

NTNU
Norwegian University of
Science and Technology

# MASTER'S THESIS FOR

**MARTIN LISA**

Thesis started: 23. August 2010
Thesis submitted: 15. May 2011

## DISCIPLINE: Physics

Title: *"Satellite mapping of particle precipitation effects on the Anctarctic middle atmosphere"*

This work has been carried out at Department of Physics, under the supervision of Prof. Dr. Patrick J. Espy

---

# Acknowledgments

First I want to thank my supervisor Patrick Espy for his enthusiasm and ilustrative talks about everything between Earth and atmosphere. Thank you too for the discussions and help of Nora Kleinknecht at the beginning of my thesis, and for Marianne Daaes help with inversions and data from her work. I also appreciate the help of Terje Røsten for solving the large number of computer problems I ran into. I am also grateful for the data provided by the European Space Agency, the Odin/SMR science team at Chalmers University and the Aura/MLS science team at NASA. Finally I want to thank my family, for the encouragement and patience of my wife Rachel, the contagious energy and joy of my oldest son Leo, and my ever smiling youngest son, Yann, who was born in the middle of this thesis.

# Abstract

The aim of this thesis is to study the effects of particle precipitation on $O_3$ and OH caused by a moderate geomagnetic storm in late July 2009. The basis is data retrieved over Antarctica from the Odin and Aura satellites for an eleven day period. Vertical profiles were extracted from scans at the limb every 165 Km (Aura) and 500 Km (Odin) covering latitudes on the SH extending to $82^oS$. Geographical variability of $O_3$ and sparse satellite coverage made it difficult to observe storm effects on a latitudinal/longitudinal scale. Zonal means post-storm show a considerable drop of ozone (30-50%) below 80 Km, and a distinct increase (50%) at altitudes above 80 Km. Comparison of the zonal means of $O_3$ and OH reveal high concordance between areas of rising hydroxyl and areas of ozone depletion, suggesting that the increase of OH production during the storm is the main cause of $O_3$ depletion. The extent of the $O_3$ and OH changes occur from geomagnetic latitudes greater than $60^o$ S and extend into the polar regions. The zonal means indicate that the OH causes the initial $O_3$ loss, and then hydroxyl disappears rapidly. The $O_3$ remains depleted for four days descending in the polar vortex suggesting contribution from other species ($NO_x$). Time series binned around geomagnetic latitude $62^o$ were compared with ground-based microwave observations from the Troll station, Antarctica. The two data sets are consistent, showing ozone losses in the order 30-50% and a gradual poleward descent of this depletion.

# Contents

# Chapter 1

# Introduction

Stratospheric ozone has been an intense research area for the last forty years due to its important implications for life on Earth. The objective has mainly been to understand the anthropogenic influences on the stratospheric ozone depletion observed in the last decades. On the other hand, the ozone concentration of the mesosphere has only recently received moderate attention by the scientific community.

The problem of ozone depletion is complex and involves a variety of factors such as: photochemistry, atmospheric transport and dynamics, sources and sinks of trace constituents, and the intensity and variability of solar radiation. Furthermore, the sun emits energetic particles and solar wind plasma that end up as particle precipitation into the Earth's atmosphere. The solar emissions can lead to Energetic Electron Precipitation (EEP) ranging 10 keV to 1 MeV which deposit their energy in the mesosphere, or to solar proton events (SPE) that penetrate down to the stratosphere, both causing ionization of atmospheric species. Despite the low energy of EEPs compared to SPEs produced at solar maxima these occur more frequently and are therefore equally important in disturbing the dynamics and chemistry of the mesosphere.

Due to atmospheric coupling, perturbations in the upper mesosphere composition can propagate to other atmospheric regions. They can affect the circulation patterns altering the zonal winds at lower altitudes. This can produce an exchange of momentum for vertical waves and horizontal winds of similar speeds, causing a cascading effect that propagates the perturbations downwards through the atmosphere.

The ionization effect of particle precipitation can result in an increase of $NO_x$ and $HO_x$ species which are important catalysts of ozone in the middle atmosphere. The work of authors like *Jackman et al.* [2001]; *Codrescu et al.* [1997]; *Saetre et al.* [2004] have shown that at high latitudes in winter, the $NO_x$ induced by ionization can have long lifetimes causing catalytic destruction of ozone over prolonged periods of time. The ionized-induced $HO_x$ on the other hand has a large devastating effect on the mesospheric ozone, but since it is short lived (on the order of hours below 80 Km) it has received less attention.

The background for this thesis was a geomagnetic storm of low to medium energy particles registered in late July 2009 over Antarctica. This storm was observed from a ground-based microwave radiometer located at the Troll station in Antarctica (-72$^o$ S, 2.5$^o$ E) in the middle of the polar winter. From ground-based observations it was estimated that the storm contributed with up to 30% ozone depletion in the middle atmosphere [*Daae*, 2010].

This thesis studies the impact of this storm on hydroxyl and ozone over Antarctica at altitudes from 50-90 Km, as observed from the Odin and Aura satellites. The motivation for this work was to address the following questions:

- Is the $O_3$ loss caused by the geomagnetic storm on the 22 July 2009 visible from instruments other than the ground-based microwave radiometer located at Troll?
- Can we see the geographical extent of $O_3$ losses in global maps of the region over Antarctica?
- How does OH produced in a geomagnetic storm behave and what role does it play in the observed $O_3$ decrease?

The area of the mesosphere-thermosphere is a very dynamic region which makes observations and models a challenging task. The work on this project is based on satellite observations which sample the atmosphere at different heights and locations at the same time each day. This gives a good global coverage of data but is not necessarily the best method for observing dynamic processes, and should be complemented by other methods such as photochemical models that follow a parcel.

This thesis is divided in a theory chapter covering the physics of the atmosphere, ozone photochemistry, particle precipitation, and methodology for remote sounding and data retrieval from the satellites. Following this are two chapters describing the instrumentation of the satellites. The main results are then presented, followed by a discussion and comparison of the findings with previous work. Finally a summary with concluding remarks is presented.

# Chapter 2

# Theory

## 2.1 The atmosphere

### 2.1.1 Composition and hydrostatic equilibrium

The theory of this subchapter is primarily based on the textbooks of *Andrews* [2000]; *Houghton* [2002]; *Wayne* [2000]; *Brasseur and Solomon* [2005]; *Salby* [1995]; *Eriksson and Merino* [1997].

The atmosphere of a planet is the gaseous envelope that surrounds it and it is held in place by the force of gravity. The atmosphere of the Earth consists of a mixture of gases with the most abundant species being $N_2$ (78% by volume) and $O_2$ (21% by volume). Minor species such as argon, ozone, carbon dioxide, water vapor and other exist only in small quantities (1% by volume). Nevertheless they have a significant influence on the heat transfer processes occurring on the Earths atmosphere. The concentration of the minor species is usually described using the mixing ratio by volume (VMR) in parts per million (ppm).

The constituents of the Earths atmosphere can be approximated by theoretical ideal gases which follow the so called ideal gas law $p = \rho RT$, where $p$ is the pressure, $\rho$ stands for density, $T$ for temperature and $R$ is the gas constant per unit mass. From a macroscopic view the atmosphere is a continuous fluid, and with some approximations the laws of fluid dynamics apply.

If we ignore the vertical acceleration caused by dynamics, each portion of the atmosphere is in hydrostatic equilibrium. This means a balance between vertical pressure gradients and the gravitational force per unit volume

$$\frac{dp}{dz} = -\rho\, g$$

In other words the vertical pressure gradient of the Earth's atmosphere is balanced by the

weight of a column of air of unit cross-sectional area. Eliminating the density by the ideal gas law and integrating we can calculate the pressure at any height

$$p = p_o \, exp[-\int_0^z \frac{dz}{H(z)}]$$

where $p_o$ is the surface pressure and the quantity $H(z)$ represents the distance over which the pressure drops with a factor 1/e, also called the scale height

$$H(z) = \frac{RT(z)}{g}$$

Assuming that the atmosphere is isothermal it follows that pressure and density fall exponentially with height. In a real non-isothermal atmosphere the pressure and density drop with height is close to this e-folding height.

The atmosphere is stratified in a number of layers by the force of gravity. In each of these layers buoyancy is the restoring force that acts on an air parcel towards stability. Considering the atmosphere as a group of layers, the thickness of each layer can be calculated by the hypsometric equation

$$z_2 - z_1 = \frac{R\overline{T}}{g} \, ln(\frac{p_1}{p_2})$$

where $\mathbf{z_1}$ and $\mathbf{z_2}$ are the heights of the pressure $\mathbf{p_1}$ and $\mathbf{p_2}$ and $\overline{\mathbf{T}}$ is the mean temperature of the layer. We can also calculate the height $\mathbf{z_2}$ of a given pressure $\mathbf{p_2}$ if we set $\mathbf{z_1}$ to zero and $\mathbf{p_1}$ to the surface pressure. Then the mean temperature $\overline{\mathbf{T}}$ corresponds to the mean temperature of all the layers from the Earths surface to the layer of pressure $\mathbf{p_2}$.

### 2.1.2 Structure

A formal division of the regions of the atmosphere is commonly based on the temperature structure. The atmosphere is divided in horizontal regions confined in height by temperature turning points. These altitudes where the temperature profile changes direction are also named 'pauses' and their altitudes can vary with latitude and season. The temperature profile divides the atmosphere into four regions depicted in figure 2.1:

- The troposphere (0-12 Km), followed by the tropopause: the troposphere is the region of the atmosphere with most vertical mixing and it is heated from below. This is because the surface of the earth emits infrared radiation and releases latent heat. Air will rise from the surface of the earth by convection and with the decreasing pressure it will expand and cool, which explains the negative temperature profile of the troposphere. When the temperature of a parcel of air has dropped below the surrounding temperature the parcel will have greater density than the surrounding air and will start sinking. In this way the temperature profile of the troposphere restricts the exchange of air between the troposphere and the stratosphere. The cold tropopause condenses and freezes out water vapor (with soluble gases and particles) so that air reaching the stratosphere is very dry

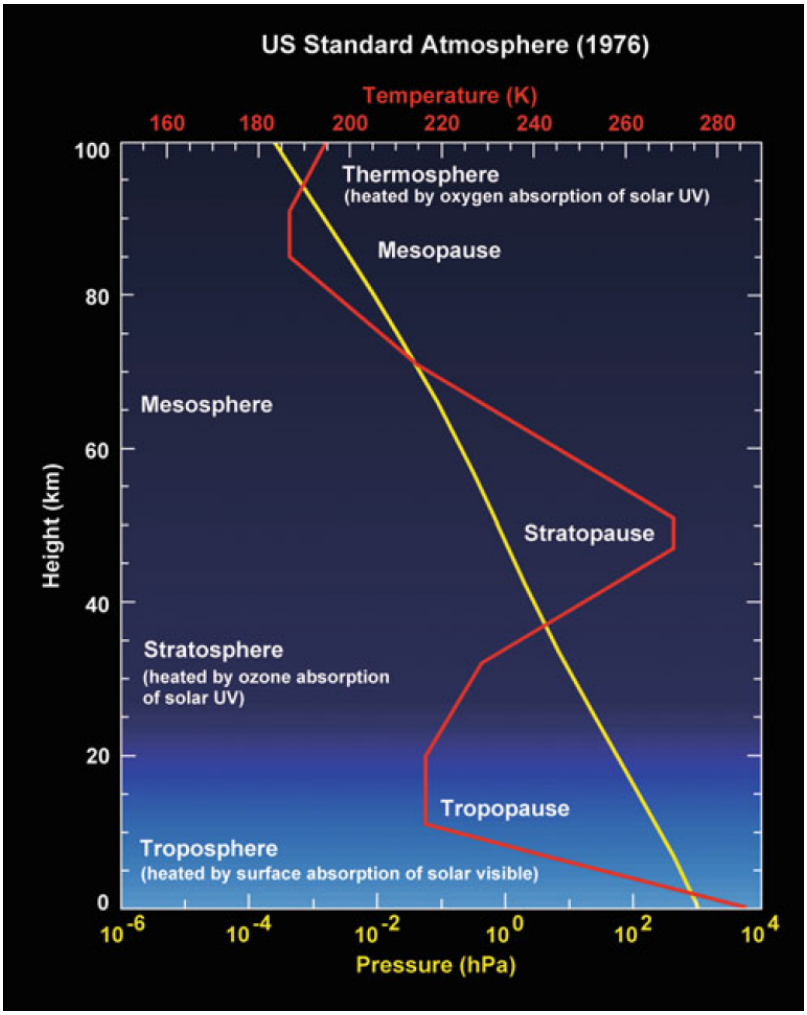


Figure 2.1: Atmospheric structure by temperature. From *Bychkov et al.* [2010]

- The stratosphere (20-45 Km), followed by the stratopause: temperature increases with altitude in the stratosphere and this heating is produced mainly when ozone and molecular oxygen absorb UV and visible radiation. Creation and photo-dissociation of ozone causes the so called ozone heating and the rising temperature profile implies a stable atmospheric region with little vertical mixing.

- The mesosphere (50-85 Km), followed by the mesopause: The temperature of the mesosphere decreases with altitude due to less ozone heating (less density of ozone) and the cooling to space effect of carbon dioxide. The mesopause reaches the coldest temperatures of the atmosphere.

- The thermosphere (>90 Km): Above 90 Km the incoming solar radiation is so intense that it breaks up most molecular bonds of $O_2$ and $N_2$. This creates a rapid temperature increase with altitude resulting in a plasma of ions and great amounts of atomic oxygen and nitrogen.

The middle atmosphere is often used to denote the regions of the stratosphere and mesosphere together.

### 2.1.3 Dynamics

The earths axial tilt and elliptical orbit around the sun creates uneven solar heating on the surface of the earth depending on the season of the year and the time of the day. This variation creates strong latitudinal energy gradients heating up mostly at equator and creating energy deficit at the poles. The atmosphere seeks an equilibrium state and transports energy poleward by dynamical processes such as thermal winds. These are produced when different parts of the atmosphere differ in temperature with the warmest part having the highest pressure. Horizontal winds will then flow from the warm part (high pressure) to the cool part (low pressure) of the atmosphere with strength proportional to the temperature gradient. Since the atmosphere is hydrostatic, vertical accelerations are small at most latitudes except at the equator. Here, warm air rises up to the tropopause and flows poleward cooling, condensing and descending at the tropics (the so-called Hadley cells).

The different heating rates, the spin of the earth and the photochemistry of the atmosphere causes a temperature field which promotes zonal winds both in the troposphere and in the middle atmosphere as depicted in figure 2.2. In the troposphere these winds are the

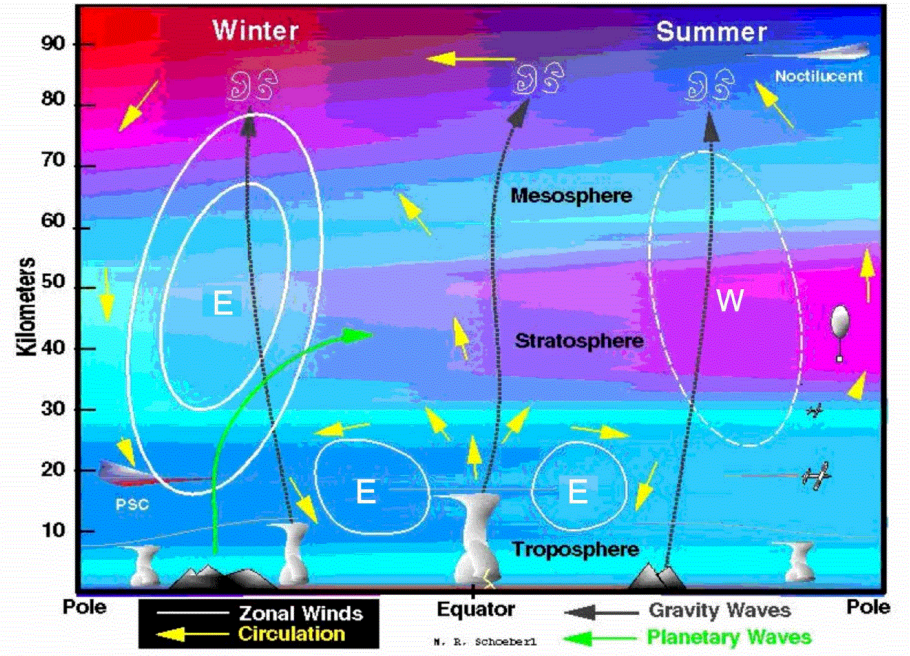


Figure 2.2: Circulation in the middle atmosphere. From *Todaro* [2003]

*jet streams* that flow eastward at mid-latitudes. At the stratosphere and mesosphere the zonal winds are eastward in the wintertime and westward in summer. The zonal winds

of the middle atmosphere can filter *gravity waves*, which are sinusoidal wind fluctuations that propagate creating temperature and density fluctuations. These small perturbations, created in the lower atmosphere, can propagate over long distances and connect different parts of the atmosphere. They gradually grow with altitude reaching high amplitudes at the mesosphere and thermosphere due to decreasing density. At these altitudes they dominate atmospheric dynamics and contribute to the energy and momentum budget by the effect of viscous damping. Gravity waves include *tidal waves* which are gravity waves with a specific horizontal scale and period driven by solar heating. Wave activity in the large planetary scale is referred to as *planetary waves* or *Rossby waves* and are caused by the variations of the Coriolis force with latitude.

### 2.1.4 Solar energy and zenith angle

The solar energy that reaches the Earth varies during the day (diurnal cycle) and during the season depending on the geographical location. The rotation of the earth around its axis causes the diurnal cycle. The seasonal variations are caused by the Earths elliptical orbit around the Sun (eccentricity) and the inclination of the Earths equator plane respect to the plane of rotation around the sun. The elliptical orbit of the earth causes the earth to be closer to the sun during the northern hemisphere winter than the southern hemisphere winter. This explain why the Southern Hemisphere experiences more extreme seasonal changes.

The inclination of the earth affects the incident solar intensity averaged over a day. The day length depends on the latitude and date, also determining the Suns maximum elevation angle. The elevation angle relative to having the Sun overhead is known as the solar zenith angle (SZA), $\theta$. This angle is minimum at noon and maximum at sunrise/sunset and is particularly large in the winter season. The SZA reduces the solar radiation intensity by a factor $\sec(\theta)$, so at night, when $\theta \geq 90^o$, the solar radiation is absent. Another effect of a large zenith angle is the increased absorption and scattering of the incoming light. For an atmosphere of depth $d_a$ normal to the earths surface, an oblique ray will travel a longer path of depth $d_a sec(\theta)$. In reality the atmosphere is curved and the optical path increases less than this factor. Larger zenith angles will generally create more absorption in the upper layers of the atmosphere and less radiation will reach the lower layers. Also the upper layers may be illuminated while the lower layers will be in shadow.

The line separating the illuminated and the dark part of the earth is called the terminator. This line is an approximation to the fading area dividing day and night and its orientation depends on the season. The polar night terminator is the region near the poles where the solar zenith angle is near $90^o$.

## 2.2 Atmospheric radiation

Solar photons collide continuously with the atmosphere at wavelengths from the ultraviolet to the infrared. Some of these photons are scattered back by atmospheric gases and other are reflected back from clouds and the earths surface. The remaining photons are either absorbed by molecules in the atmosphere or by the earths surface. Atmospheric radiation deals with the energy transfer of these photons (mainly solar 0.1-0.4 $\mu$m and thermal 4-100$\mu$m) and their interaction with atmospheric gases.

### 2.2.1 Radiative transfer

Absorption of a photon's energy results in either to:

- Rotational, vibrational or electronic excitation of the molecule. The molecule will either re-radiate energy in an arbitrary direction or make collisions before it can radiate, transfering its internal energy to the kinetic or internal energy of the colliding species.
- Dissociation, where the molecule is split up and the fragments carry the excess energy as kinetic and internal energy. Any remaining internal energy in the fragments will do the same.

The transfer of collisional and radiative energy such that internal energy states maintain a boltzman distribution whilst the photons mantain a Planck distribution is called Local Thermodynamic equilibrium. It depends on the photon energy (its wavelength), lifetime and the collision frequency of the molecules.

Parts of the atmosphere are heated when certain species absorb the incoming solar photons such as oxygen and ozone in the ultraviolet or when water vapor and carbon dioxide absorb radiation from the Earth's surface in the infrared. These species also cause emission of infrared photons to other layers of the atmosphere and to outer space. This continuous heat transfer process is usually known as the radiative transfer and can be described by the radiative-transfer equation (Schwarzschild's equation). Assume a beam of radiation of unit cross-sectional area traveling in the vicinity of the direction $s$ through atmospheric gases. In a small distance $ds$ along this path the spectral radiance $L_\nu$ will decrease proportionally to the number of photons absorbed and scattered. The sum of the absorption and scattering coefficients at a given temperature and pressure is known as the extinction coefficient $k_\nu$. Furthermore, the absorbed energy is equal to the emitted energy following *Kirchhoff's Law*. A gas can therefore emit radiation at discrete frequencies reinforcing the spectral radiance of the beam along its path. This added power per unit area can be approximated by a source function $J_\nu(s)$ and depends on the temperature of the gas. The radiative transfer equation as a function of distance $s$ can then be expressed as:

$$\frac{dL_\nu}{d\chi_\nu} + L_\nu = J_\nu \tag{2.1}$$

$$where\ \chi_\nu(s) = \int_{s_o}^{s} k_\nu(s')\rho_a(s')ds' \tag{2.2}$$

$$J_\nu(s) = k_\nu B_\nu(T) \tag{2.3}$$

The optical path $\chi_\nu$ is the total amount of absorbing scattering material in the distance $s_o - s$ where $\rho_a$ is the density of the radiative active gas. The source term $J_\nu(s)$ is proportional to the term $B_\nu(T)$ which is the black body spectral radiance for an atmosphere in thermodynamic equilibrium given by Planck's function:

$$B_\nu(T) = \frac{2h\nu^3}{c^2[exp(h\nu/k_bT) - 1]} \tag{2.4}$$

where $h$ is Planck's constant and $k_b$ is the Boltzmann constant. A solution to the radiative transfer equation given the radiance at any point s is given by

$$L_\nu(s) = L_{\nu 0}\, e^{-\chi_\nu} + \int_0^{\chi_\nu} J_\nu(\chi')\, e^{-(\chi_\nu - \chi')}\, d\chi' \tag{2.5}$$

where $L_{\nu 0}$ is the spectral radiance at the point $s_0$. This solution contains two terms, the first representing the attenuation of the spectral radiance $L_{\nu 0}$ over the optical path and the second term includes the contribution of the sources of each layer attenuated by the remaining optical path.

An atmospheric region is said to be *optically thick* at a frequency when its optical path $\chi_\nu$ is greater than one and *optically thin* if smaller than one. The probability of absorption or scattering in an optically thick region is very high compared to an optically thin region. At high altitudes it is possible to measure weak emissions by limb remote sensing since they traverse optically thin regions. This is more difficult to measure from the ground where the emitted radiation has to traverse the optically thick troposphere.

At microwave frequencies the wavelengths are large enough to neglect scattering. The atmospheric radiation is governed by absorption and the rotational transitions are the predominant absorbing processes. This simplifies the calculation except for the fact that at these wavelengths refraction plays a role on the path direction. By applying the Rayleigh-Jeans approximation $h\nu \ll kT$ to Planck's function in the microwave frequencies the black body spectral radiance is

$$B_\nu(T) \approxeq \frac{2\nu^2 kT}{c^2} = \frac{2kT}{\lambda^2} \tag{2.6}$$

where $\lambda$ is the wavelength. Rearranging equation 2.6 and inserting equations 2.3 and 2.5 we can define the brightness temperature $T_b$ as

$$T_b(\nu) = \frac{\lambda^2}{2k_b} L_\nu \tag{2.7}$$

The brightness temperature $T_b$ is more often used in microwave radiometry than the spectral radiance. It differs from the physical temperature of a black body as a function of frequency with the largest discrepancies at high frequency.

### 2.2.2 Spectroscopy and line broadening

A molecule will absorb or emit thermal photons depending on energy differences between vibrational or rotational excited states. These differences and hence photon frequencies are discrete in nature following the quantum-mechanical selection rule. For pure vibrational transitions the emitted wavelengths are about 1-20 $\mu$m (infrared) and for pure rotational transitions the wavelengths are in the range $10^2$-$10^4$ $\mu$m (in the infrared to radio frequency range).

Due to the discrete nature of the transitions the extinction coefficient $k_\nu$ will in theory disappear but near the transition frequencies. However, each line will have a narrow natural width determined by the radiative lifetime of the excited state of the molecule. All the transitions of a molecule will create a discrete line spectrum and it can be regarded as a footprint of the species. In practice these discrete lines get broadened by a number of mechanisms as seen on the atmospheric spectrum from figure 2.3. These broadening

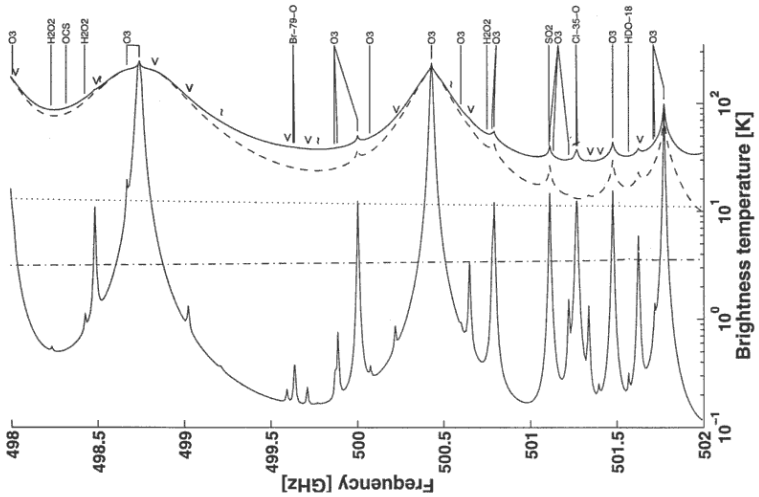


Figure 2.3: Figure of simulated spectrum for the Odin SMR instrument in the range 498-502 GHz. The upper solid curve shows the total emission at tangent altitude 20 Km and the lower solid curve for a tangent altitude of 40 Km. The dashed curve shows only ozone at tangent altitude 20 Km. From *Eriksson and Merino* [1997]

mechanisms can be approximated by line-shape functions $f_n$ with extinction coefficients at the frequencies $\nu_n$

$$k_\nu = \sum_n S_n f_n(\nu - \nu_n) \tag{2.8}$$

where $S_n$ are the line strengths and the line-shape functions $f_n$ are normalized to unity. The spectroscopic parameters such as center frequency and line strength can usually be found in spectroscopy databases such as the spectral line catalog of the JPL [*Jet Propulsion Laboratory*, 2011b]

Even though molecules only absorb and emit photons close to the line centre frequencies, different physical processes spread the absorption to neighboring frequencies. A typical absorption/emission spectra will not look as a sequence of discrete delta peaks but rather like a continuous spectra where the peaks have wings that overlap. At the earth's atmosphere the broadening in the microwave frequencies is caused mainly by molecular collisions at high pressures (lower altitudes) and by molecular thermal motion at higher altitudes.

### 2.2.3 Pressure broadening

At high pressure, collisions between molecules shorten the lifetime of their excited energy levels. This causes uncertainty in the energy levels and causes the transition of the lines to be broadened. The pressure broadening close to the transition frequency $\nu_n$ can be described by the Lorentz function:

$$f_L(\nu - \nu_n) = \left(\frac{\gamma_L}{\pi}\right) \frac{1}{(\nu - \nu_n)^2 + {\gamma_L}^2} \quad \text{where} \quad \gamma_L = \frac{1}{2\pi\tau_c} \tag{2.9}$$

Here the constant $\gamma_L$ is the half-width at half maximum (HWHM) of the line which can be calculated from the temperature by kinetic theory and $\tau_c$ is the collisional lifetime.

Some species contribute more to the pressure broadening than other with $O_2$ and $N_2$ being the most prominent. Since pressure varies rapidly with altitude the pressure broadening indirectly gives us information about the height of the emission.

### 2.2.4 Doppler broadening

The thermal motion of the molecules causes the emitted radiation to be perceived with a frequency shift at the receiver, similar to the pitch shift of a passing ambulance for sound waves. At thermal equilibrium the molecular velocities follow the Maxwell-Boltzmann distribution and the convolution of the probability function with a delta function describes the Doppler function:

$$f_D(\nu - \nu_n) = \frac{1}{\gamma_D\sqrt{\pi}} \exp\left(-\frac{(\nu - \nu_n)^2}{\gamma_D^2}\right) \quad \text{where} \quad \gamma_D = \frac{\nu_n}{c}\sqrt{\frac{2kT}{m}} \tag{2.10}$$

here $\nu_n$ is the transition frequency, $m$ is the molecular mass, $T$ is the temperature and $k$ the Boltzmann constant.

Up to the stratosphere and mesosphere the pressure mechanism dominates the broadening but as density decreases and temperature rises, Doppler becomes equally important. At these altitudes the height information is lost since the temperature dependence of Doppler contains only information on temperature. Figure 2.4 illustrates how the line-width narrows with altitude with the Doppler broadening becoming dominant in the middle and upper mesosphere.

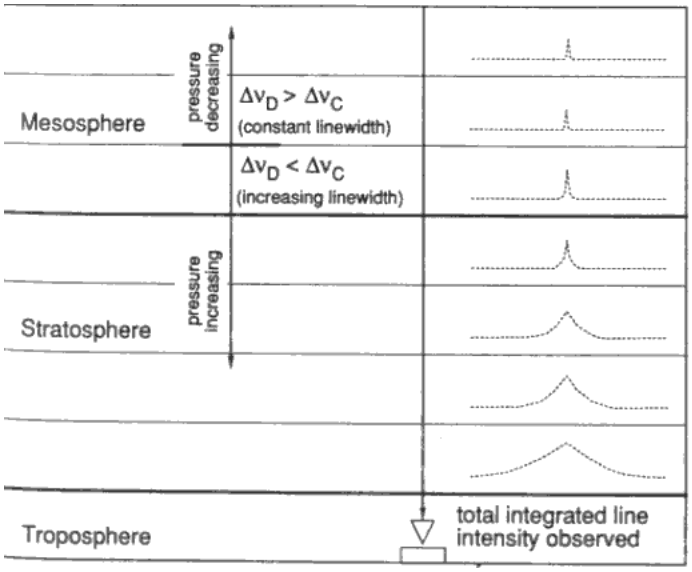


Figure 2.4: Line-shape of pressure broadening ($\Delta\nu_C$) and Doppler broadening ($\Delta\nu_D$) in the stratosphere and mesosphere from *Janssen* [1993]

At altitudes where pressure and Doppler both contribute to the broadening the two functions $f_L(\nu - \nu_n)$ and $f_D(\nu - \nu_n)$ are convolved to form the Voigt profile. This profile approaches the pure pressure function at high pressure and the Doppler function at low pressure.

## 2.3 Ozone

The stratosphere contains the highest concentration of ozone in the atmosphere which has important implications for life on earth. Ozone absorbs virtually all UV radiation of about 240-290 nm, a range which is lethal to all biological species on Earth, and reduces the radiation in the range 290-320 nm which is less harmful but still biologically damaging.

Ozone is formed photochemically from $O_2$ and is found throughout the atmosphere with the highest densities in the stratosphere and the mesosphere. The highest ratio of ozone (up to 6 ppmv) is found in the stratosphere at around 30 Km and is known as the 'First ozone maximum', popularly named the ozone layer. In the upper mesosphere, at altitudes above 90 Km another 'Second ozone maximum' has been observed and explained by several authors [*Marsh et al.*, 2001; *Kaufmann et al.*, 2003; *Brasseur and Solomon*, 2005]. The mixing ratios here vary from as much as 1 ppmv daytime to 10 ppmv nighttime. The first and second ozone maximum are relatively well understood phenomena at present. A 'third ozone maximum' was first measured by the MLS instrument (Microwave Limb Sounder) in the UARS (Upper Atmosphere Research Satellite) in 1992 [*Froidevaux et al.*, 1996] at altitudes around 72 Km in winter and near the polar night terminator. This ozone maximum is denoted the Middle Mesosphere Maximum (MMM) due to its location in the middle mesosphere, with peak values of up to 3 ppmv [*Marsh et al.*, 2001]. Several computer models such as the GCM LIMA and WACCM [*Sonnemann et al.*, 2007; *Sofieva and et al.*, 2009] are continuously being developed and are used in conjunction with satellite observations to quantify and understand this anomaly. The main topic of this thesis is related to the changes in the MMM during particle precipitation events.

### 2.3.1 Transport and dynamics

The solar flux is strongest at equator and most ozone is created in this region. But the circulation in the stratosphere moves air from low latitudes towards polar regions. The column densities measured for the year 1990 by the TOMS instrument (Total Ozone Mapping Spectrometer) are depicted in figure 2.5 showing variations with season and geographical latitude.

The Dobson Unit (DU) expresses the height in hundredths of millimeter of the compression of an ozone column to the pressure of one atmosphere and temperature $0^oC$. The ozone density is generally greater at higher latitudes and around the local winter were the sun is absent most of the day and no photo-dissociation occurs. Nevertheless there are differences between the concentrations near the two poles indicating differences in the stratospheric dynamics at each hemisphere. In the arctic region the vortex is weaker due to greater planetary wave activity and differing topography. As a result, the temperature is warmer affecting chemical production and the less stable vortex causes mixing with lower latitude, oxygen rich air.

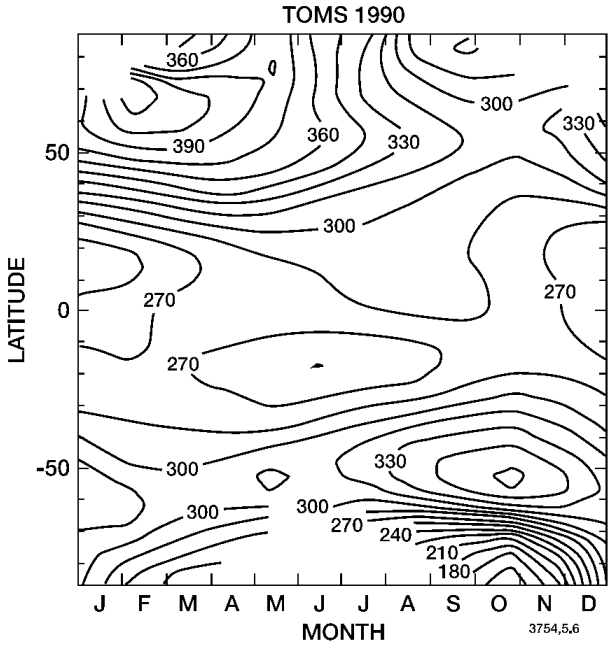


Figure 2.5: Variations of total ozone (DU) registered by TOMS in 1990. From *Brasseur and Solomon* [2005]

### 2.3.2 Ozone chemistry

The first theoretical explanation of the ozone layer was given by Chapman in 1930 who proposed a model of a pure-oxygen photochemical steady-state reaction:

$$O_2 + h\nu \rightarrow O + O \quad (2.11)$$

$$O_2 + O + M \rightarrow O_3 + M \quad (2.12)$$

$$O_3 + h\nu \rightarrow O + O_2 \quad (2.13)$$

$$O_3 + O \rightarrow 2O_2 \quad (2.14)$$

where $h\nu$ represents the absorption of a photon and M is a species that dissipates energy in collisions (e.g. $N_2$ or $O_2$ on Earth). Equation 2.12 is the only reaction acting as an ozone source and results from absorption of radiation at wavelengths between 185-242 nm (Herzberg continuum) for the first maximum and between 137-200 nm for the second maximum. [*Marsh et al.*, 2001]:

Equations 2.13 and 2.14 represent the ozone sinks. The photolysis of ozone in 2.13 happens at wavelengths less than 1140 nm and results in the creation of atomic oxygen in either the ground state $O(^3P)$ or the first excited state $O(^1D)$. Equations 2.11 and 2.13 are photolytic reactions representing sources of atomic oxygen. $O(^1D)$ is also produced by the photolysis of molecular oxygen (2.11) at wavelengths of less than 242 nm being therefore very altitude dependent. The sinks of atomic oxygen are represented by the reactions 2.12 and 2.14, the latter being strongly temperature dependent. Reactions 2.12 and 2.13 inter

convert O and $O_3$ , with life-times down to 100 s, and determine the ratio of [O]/[O3]. Reaction 2.12 becomes slower with increasing altitude due to lower density, whereas reaction 2.13 becomes faster due to increased solar radiation. This means more atomic oxygen at greater heights but less production of ozone at daytime. Ozone is continuously formed by the recombination of atomic oxygen made during the day, but not destroyed by2.13 creating the diurnal variations shown in figure 2.6.

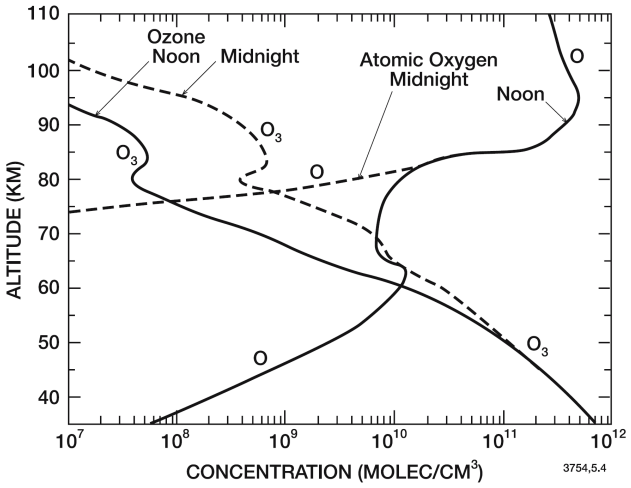


Figure 2.6: Calculated vertical distribution of ozone and atomic oxygen at noon and midnight. From *Brasseur and Solomon* [2005]

The fact that the density falls off exponentially causes more atomic oxygen than ozone in the upper mesosphere.

### 2.3.3 Catalysts

In the middle atmosphere reactive species or catalysts (X) such as odd hydrogen($HO_x$ includes H, OH, $HO_2$), odd nitrogen ($NO_x$ includes N, NO and $NO_2$), Chlorine (Cl) and Bromine(Br) contribute to a depletion of ozone and atomic oxygen through the following catalytic cycle:

$$\mathrm{X} + \mathrm{O_3} \rightarrow \mathrm{XO} + \mathrm{O_2} \quad (2.15)$$

$$\mathrm{XO} + \mathrm{O} \rightarrow \mathrm{X} + \mathrm{O_2} \quad (2.16)$$

$$\text{Net: } \mathrm{O_3} + \mathrm{O} \rightarrow 2\mathrm{O_2} \quad (2.17)$$

Chemical models and measurements of the mesosphere and upper stratosphere suggest that the odd hydrogen catalytic cycles dominate the ozone losses above 50 Km [*Grenfell et al.*, 2006; *Rohen et al.*, 2005]. An important hydroxyl catalytic cycle that reduces atomic

oxygen through reaction 2.16 in the mesosphere [*Marsh et al.*, 2001] is:

$$\begin{aligned} O + OH &\rightarrow O_2 + H && (2.18)\\ H + O_2 + M &\rightarrow HO_2 + M && (2.19)\\ O + HO_2 &\rightarrow O_2 + OH && (2.20)\\ \text{Net: } O + O &\rightarrow 2O_2 && (2.21) \end{aligned}$$

All the chemical reactions shown are connected by a set of partial differential equations with differing time constants. The speed, type and amount of catalytic cycles is highly altitude dependent. The catalytic cycles only have a limited lifetime and at some point catalysts recombine together to species that do not attack ozone, called reservoir compounds. The lifetime of odd hydrogen up to 80 Km is typically less than one hour and the lifetime of odd nitrogen is several days as shown in figure 2.7. The latter is comparable to the transport time of zonal and meridional winds in the stratosphere and similar to eddy diffusion coefficients. Ozone has a lifetime of less than a day in the mesosphere which has been documented by a number of authors [*Maeda and Aikin*, 1968; *Aikin and Smith*, 1999].

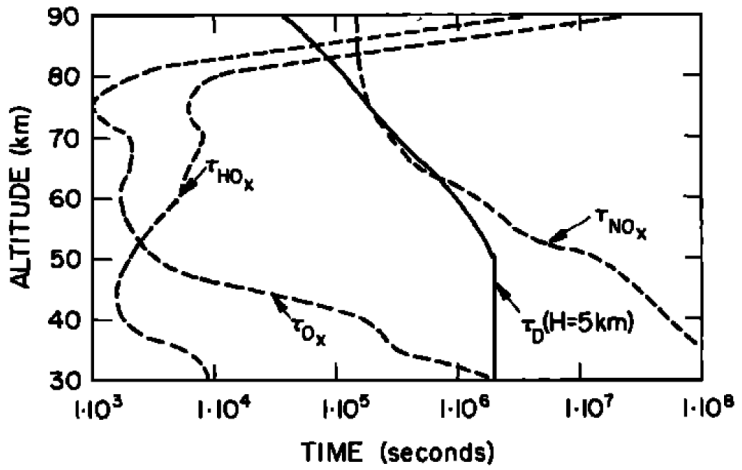


Figure 2.7: Photochemical lifetimes for the $HO_x$, $O_x$, and $NO_x$ families and the approximate diffusive lifetime for scale height of 5 Km. From *Solomon et al.* [1982]

### Odd oxygen family

A classification of chemicals according to their time constants leads to groups with similar reaction times. The odd oxygen family ($O_x$) consisting of ($O(^3P)$, $O(^1D)$ and $O_3$) undergo very fast reactions and can be studied in relation to other fast reacting families such as the odd hydrogen family ($HO_x$). The chemical reactions forming and destroying ozone (equations 2.12 and 2.14) depend on the amount of odd oxygen. The main source of atomic

oxygen is photolysis of $O_2$ (reaction 2.11) by radiation in the Schumann-Runge continuum and Schumann bands at wavelengths 137-200 nm, which takes place in the thermosphere as depicted in figure 2.8

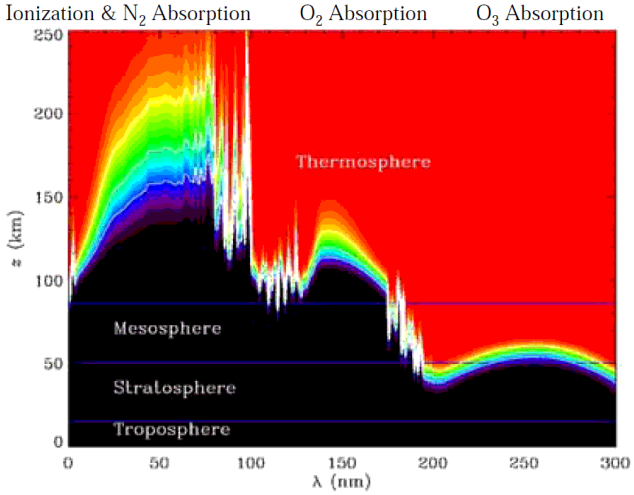


Figure 2.8: Energy deposition in the atmosphere. From J.H. Yee.

Atomic oxygen is transported downwards from the thermosphere to the mesosphere through advection (vertical winds) or through macroscopic eddy diffusion and wave mixing. The lifetime of the $O_x$ family determines if an atmospheric region is controlled by photochemistry or by transport processes. The first happens if photochemical production and destruction is in balance reaching steady state, and takes place at altitudes 30-80 Km for all latitudes except for high latitudes in the local winter (due to the polar vortex). The second occurs when the lifetime of $O_x$ is long, enabling dynamic processes to play a primary role on the composition. This takes place at high winter latitudes, particularly within the polar vortex and generally for levels above 80 Km. [*Brasseur and Solomon*, 2005]

### Odd hydrogen family

As shown previously, the family of odd hydrogen ($HO_x$) undergoes rapid reaction processes under 80 Km and is one of the most reactive catalysts in the middle mesosphere. The main source odd hydrogen is oxidation of $H_2$ and $H_2O$ and residual photolysis of water vapor. The rate of each of these processes depend on the water vapor concentration, height, latitude and season. In the mesosphere, water vapor injection is caused by upward diffusion and advection from the stratosphere (originating in the troposphere) and by production through methane oxidation. $HO_x$ is found in mixing ratios of 6 ppmv up to 70 Km decreasing to 4 ppmv at 75 km. [*Aikin and Smith*, 1999]

The oxidation and photolysis of water vapor in the upper mesosphere and thermosphere

follows the reactions:

$$H_2O + O(^1D) \rightarrow 2OH \quad (2.22)$$
$$H_2O + h\nu \rightarrow H + OH \quad (2.23)$$
$$H_2O + h\nu \rightarrow H_2 + O(^1D) \quad (2.24)$$

Where reaction 2.23 is the photo-dissociation occurring for photons of wavelengths $\lambda <$ 200 nm and reaction 2.24 only happens for wavelengths $\lambda < 147$ nm. Particularly the Lyman-$\alpha$ line at 121.6 nm is in a range of weak atmospheric absorption and can traverse the upper mesosphere. Here it is responsible for the dissociation of water vapor, carbon dioxide and methane. Odd hydrogen can also be reduced by reaction with watervapor [*Rohen et al.*, 2005]

$$OH + H_2O \rightarrow H_2O + O_2 \quad (2.25)$$

$HO_x$ can also be created by ion-molecule reactions associated with ionization of EEP precipitation. This production has to compete with the photolysis dissociation and is therefore very dependent on the water distribution. [*Solomon et al.*, 1982; *Aikin and Smith*, 1999]

### 2.3.4 Middle mesosphere maximum (MMM)

An ozone increase of up to 3 ppmv has been reported by several authors at high latitudes in the winter hemisphere. It is known as the middle mesosphere maximum (MMM) and peaks at about 72 Km altitude, at latitudes close to the polar night terminator. The MMM has its origin in an increase of atomic oxygen caused by downward transport from the thermosphere together with a reduction of hydrogen radicals that attack odd oxygen.[*Sonnemann et al.*, 2006]. This is because at grazing incidence the wavelengths that create odd hydrogen are blocked while those that dissociate $O_2$ remain. Thus there is a build up of $O_3$ near 75 Km at nightime.

During daytime the $HO_x$ catalytic cycle reduces the O amount at small zenith angles. At sunset $H_2O$ dissociation stops before O dissociation due to the different dissociation wavelengths.[*Aikin and Smith*, 1999]

At latitudes near the polar night terminator the solar radiation enters the middle mesosphere at nearly $90^o$ zenith angle. It penetrates all the layers in an optically thick atmosphere for wavelengths less than 185 nm [*Marsh et al.*, 2001]. At this grazing incidence the column density of molecular oxygen through its path is large, so a small but continuous amount of radiation is dissociating $O_2$ and $O_3$ (50% at SZA $92.3^o$) [*Hartogh et al.*, 2004]. However there is a net production of atomic oxygen in the few hours where the solar radiation enters the mesosphere at grazing incidence. The produced atomic oxygen then recombines with molecular oxygen into ozone after sunset. The absorption cross section of $H_2O$ is about three orders of magnitude greater that of $O_2$at wavelengths near the Lyman-$\alpha$ line . This implies that the radiation in the Schumann-runge bands is transmitted

deeper through the mesosphere than the radiation in the Lyman-$\alpha$ region. Since the first dissociates molecular oxygen and the latter dissociates water vapor, the net result is an almost constant production of atomic oxygen and a decrease of production of odd hydrogen. Odd hydrogen radicals being the main loss mechanism for ozone and atomic oxygen at this height, results in an accumulation of ozone in the middle mesosphere. [*Hartogh et al.*, 2004; *Kaufmann et al.*, 2003].

## 2.4 Particle precipitation and ionization

The solar energy arriving at the Earth's atmosphere is a combination of radiative energy and non-radiative energetic particles. The precipitation of these particles has an ionization and dissociation effect on the atmospheric ionosphere, and since they are charged particles, they enter the atmosphere following the Earth's magnetic field.

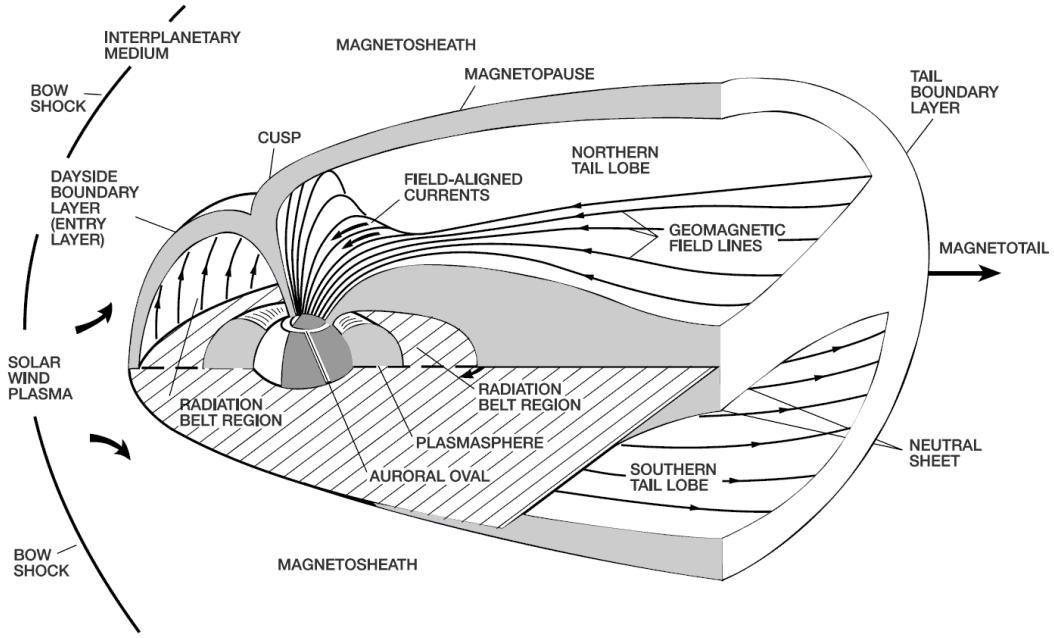


Figure 2.9: Schematic representation of the magnetosphere. [*Kelly*, 1989]

The magnetic field of the Earth extended into space is named the *magnetosphere*, resulting from the interconnection of the Earth's magnetic field and the Interplanetary Magnetic Field (IMF). The latter consists of a magnetic field transported by the *solar wind* which is composed of an ionized plasma-stream released by the sun. The magnetosphere is not symmetric around the Earth but rather compressed by the IMF on the sunward side of the Earth as shown on figure 2.9. The radiation belts (Van Allen) are torus shaped zones of energetic charged particles (plasma) surrounding the Earth, that extend from the NH to

the SH geomagnetic poles with highest density near the equator. They constitute a stable inner belt and a more dynamical outer belt where changes in the magnetosphere can cause particle precipitation to polar areas.

In periods of high solar activity the density and propagation speed of the solar wind can cause shock waves that impact the magnetosphere at certain latitudes, known as a *geomagnetic storms*. Figure 2.9 shows how some of the charged particles from the radiation belts enter the Earth's atmosphere. They move along the magnetic field lines and precipitate at the polar regions in periods of storm activity [*Kelly*, 1989].

The resulting field lines of the magnetosphere extend downstream forming the north and south tail lobes which have opposite directions separated by a neutral plasma sheet. As this sheet flows towards the earth, it creates a greater magnetic field and induces a longitudinal ring current around the Earth's equator. This ring current varies depending on the solar activity and will increase considerably in the presence of a geomagnetic storm. The ring current activity is continuously being measured from a number of observatories close to the Earth's equator. The current variations are monitored with the *Dst index* which shows negative values in the presence of a storm [*Rostoker*, 1972].

When energetic particles penetrate the Earth's atmosphere, mostly near the geomagnetic poles, they can reach down to a depth proportional to their energy and mass.

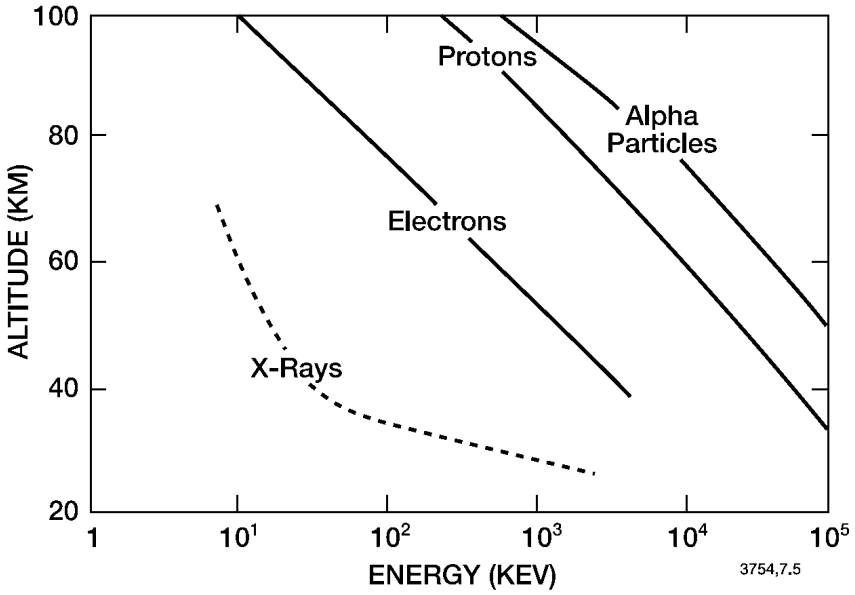


Figure 2.10: Depth of atmospheric penetration for different charged particles and X-rays as a function of energy. From *Brasseur and Solomon* [2005]

As shown in figure 2.10 the highly energetic particles penetrate deeper, and precipitating particles can be classified as:

- X-rays:

Small amounts of X-rays are created by collision between energetic particles and atmospheric gases (*bremstrahlung* process), penetrating deeper than the energetic particles themselves.

- Electrons:

  Electrons with low energies (auroral particles of 1-10 keV) can precipitate from the magnetospheric plasma-sheet at latitudes $70^o$-$75^o$ (*auroral oval*) above 100 Km.

  At high latitudes ionization can be caused by Energetic Electron Precipitation (EEP) from electrons trapped on the Earth's radiation belts with energies ranging 10 keV to 1 MeV. The electrons spiral around magnetic field lines and bounce forth and back between the magnetic poles. But under disturbance of the magnetosphere some electrons accelerate along the field lines and do not rebounce but are scattered into the 'loss cone'. They then precipitate into a denser atmosphere and deposit their energy at the mesosphere. Linked to geomagnetic storms these have a short lifetime but can happen up to 10% of the time and precipitate around the *sub-auroral oval* (latitudes lower than $70^o$). These medium energy particles cause an increase of $HO_x$, $NO_2$ and NO but a decrease of ozone in the mesosphere at the polar regions [*Codrescu et al.*, 1997; *Saetre et al.*, 2004].

- Protons:

  In periods of great solar activity, solar flares and coronal mass ejections (CME) produce Solar Proton Events (SPE) with heavy particles of energies ranging 10-500 MeV. These can collide into the Earth's atmosphere and produce ionization at the Earth's D-region, mostly at polar regions. These events occur sporadically but they last for several days altering considerably the composition of the upper and middle atmosphere.

- Alpha particles:

  These originate from galactic cosmic rays arriving from outside the solar system with energies ranging between one and several hundreds MeV.

## 2.5 Remote sounding from satellites

Remote sounding is a technique where the structure and composition of the atmosphere is measured at a distance, and not in the vicinity of the measuring device. This can be from ground-based instruments, balloons, spacecrafts or instruments on orbiting satellites. What is measured is the amount of electromagnetic radiation emitted, scattered or absorbed in the atmosphere within a limited frequency range. Remote sounding can be active, with an emitter (e.g. a radar) that sends out pulses of radiation and measures what is scattered back or passive, where the radiation received is either thermal radiation emitted from atmospheric species or solar radiation transmitted or scattered by the atmosphere. The SMR and MLS instruments are passive remote sounders located on the Odin and Aura satellites that measure the spectral characteristics and intensity of radiation emitted by atmospheric constituents.

### 2.5.1 Satellite orbits

Odin and Aura are scientific satellites with quasi-polar sun-synchronous low earth orbits (LEO) that pass a location on Earth at the same local solar time.

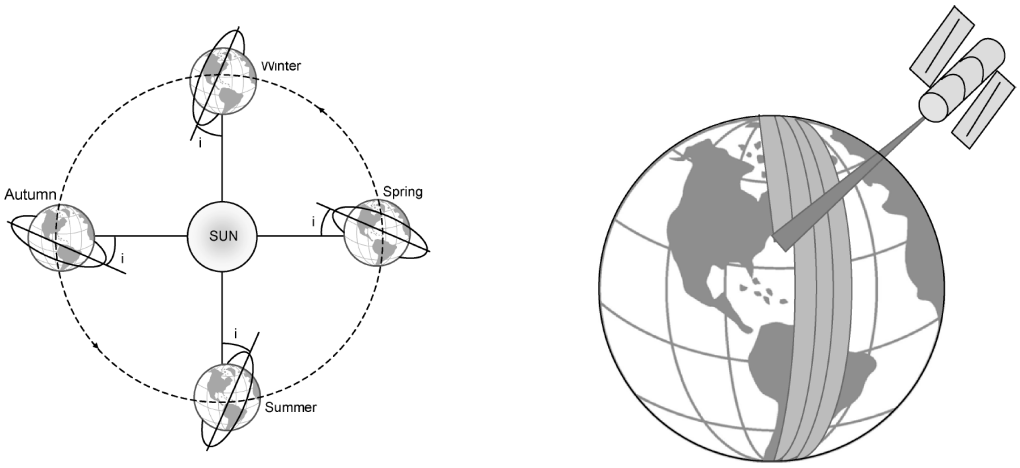


Figure 2.11: Sun-synchronous orbit and Earth coverage of sun-synchronous satellites [*Maini and Agrawal*, 2011]

As shown in figure 2.11 a sun-synchronous orbit lies in a plane that keeps a fixed angle with the Earth to sun direction. With the seasons, the orbit plane changes relative to the Earth's equator plane but not relative to the Earth to sun direction. Hereby the satellite passes a location at the same local solar time assuring similar illuminating conditions which only are affected by seasonal changes. The right picture of figure 2.11 shows how a satellite scans a slice of the Earth's surface at one orbit and at the following orbit the rotation of the Earth shifts the scan westward.

### 2.5.2 Limb sounding

The radiometers on board the Odin and Aura satellites scan the atmosphere at the limb. This means that the line of sight of the sensor is always above the ground looking tangentially through the atmosphere with the lowest altitude being the *tangent height* $z_o$ (shown on figure 2.12). The tangent point is located at the tangent height $z_o$ and at a distance $s_o$ from the sensor along the line of sight [*Urban et al.*, 2004a].

Integration of the radiative transfer equation needs to take into account the geometry of limb sounding. Here the length of the propagation path through a layer will be greater than the thickness of that layer, particularly near the tangent height.

The radiance measured by the instrument in the satellite are a function of temperature profile and extinction coefficient profiles. Therefore the propagation path is divided in

sections with constant temperature and constant extinction coefficients hereby defining the atmospheric layers. A point of the atmosphere can be traced by its altitude over the ground and by its position on the propagation path in respect to the tangent point.

If the atmospheric layers are assumed to be homogeneous and spherical symmetric, each layer contributes twice and the total intensity that the instrument receives is the sum of the N+1 layers [*Eriksson and Merino*, 1997].

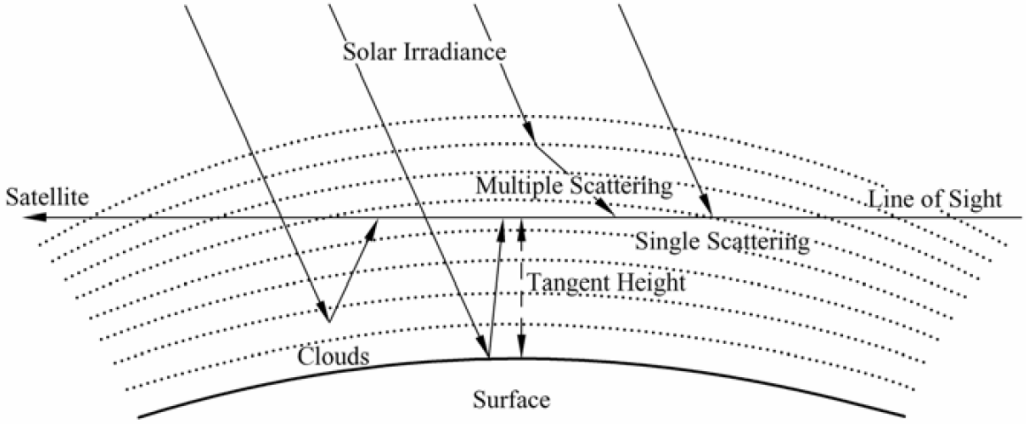


Figure 2.12: Limb sounding from a satellite. From *Flynn et al.* [2005]

The contribution from layers at high altitudes is small due to the small density of species. Since density decreases exponentially with height, at lower altitudes the emitted radiation is more intense. But at levels lower than a certain height the atmosphere is so optically thick that the increased radiation gets absorbed on its way up, making a small contribution at the receiver. Therefore an altitude layer is at an optimal height when a combination of density and attenuation above it make it contribute with the highest total radiance.

At limb sounding most of the radiation is created near the tangent height resulting in narrow weighting functions. These weighting functions give an indication of how good a vertical resolution can be achieved in a measurement as explained in the next section.

The horizontal resolution of limb sounding is dependent on the vertical resolution with a resolution of 2 Km corresponding to a path of 320Km in the layer near the tangent point.

Since a satellite like Odin moves at a speed of 7 Km/s and 90 seconds are spent on a vertical scan of the limb, the vertical profile is retrieved from a range of ±315 Km around the mean scan position of that orbit [*Urban et al.*, 2004b].

## 2.6 Retrieval methods

A physical system can be studied using the following three-step methodology:

- Parametrization of the system: discovery of a minimal set of model parameters whose values completely characterize the system. The choice of parameters is usually not unique.
- Forward model: discovery of the physical laws allowing us, for given values of the model parameters, to make predictions on the results of measurements on some observable parameters.
- Inverse model: use of the actual results of some measurements of the observable parameters to infer the actual values of the model parameters.

Here a summarized version of the three steps is presented, a theoretical description of the forward and inverse models is presented in detail by *Rodgers* [1976]; *Eriksson and Merino* [1997]; *Buehler et al.* [2005]; *Tarantola* [2005].

### 2.6.1 The forward model

If one has a large database containing atmospheric states and their measured spectra an atmospheric parameter can be retrieved. Instead of this look-up procedure, a forward model is a theoretical model that describes the physical relationship between the atmospheric state and the measured spectrum including the instrumental influence. In remote sensing the parameter wanted is indirectly retrieved from information received in form of electromagnetic waves.

In microwave radiometry, the indirect information is the emission of energy at a number of discrete frequencies that form a spectrum. The retrieved parameter is the vertical distribution of the concentration of the species of interest and the forward model describes the radiative transfer equation and the instrumental characteristics. The forward model must be as correct as possible and its error sources must be well known to characterize the retrieval.

The atmospheric radiative transfer is usually discretized by using a limited number of model parameters. The parameters are divided into the state vector $\mathbf{x}$ containing the parameters to be retrieved (the species profile of interest in our case) and the model parameter vector $\mathbf{b}$ representing the remaining parameters such as spectroscopic data of other species and temperature profile. The forward model $\mathbf{F}$ describes the relationship between the measured spectrum $\mathbf{y}$ and the atmospheric state:

$$\mathbf{y} = \mathbf{F}(\mathbf{x}, \mathbf{b}) + \varepsilon_y$$

The quantity $\varepsilon_y$ contains measurement errors such as thermal noise from the instrument and the received signal, and a finite width of the spectrometer channels and the antenna pattern.

The forward model can be approximated by linearization at a reference state in the atmosphere. This means that during the calculation of one species all other gases are assumed constant. At the reference state the reference profile $\overline{\mathbf{x}}$ must be close to the true profile $\mathbf{x}$, and the model parameters are estimated and included in the vector $\widehat{\mathbf{b}}$. By defining the matrices:

$$\mathbf{K_x} = \frac{\partial \mathbf{F}}{\partial \mathbf{x}}|_{\mathbf{x}=\overline{\mathbf{x}}} \qquad\qquad \mathbf{K_b} = \frac{\partial \mathbf{F}}{\partial \mathbf{b}}|_{\mathbf{b}=\widehat{\mathbf{b}}}$$

the forward model can be approximated by the first order Taylor expansion:

$$\mathbf{y} = \mathbf{F}(\overline{\mathbf{x}}, \widehat{\mathbf{b}}) + \mathbf{K_x}(\mathbf{x} - \overline{\mathbf{x}}) + \mathbf{K_b}(\mathbf{b} - \widehat{\mathbf{b}}) + \varepsilon_\mathbf{y}$$

$\mathbf{K}_x$ and $\mathbf{K}_b$ are known as the weighting functions of the forward model and represent the sensitivity of the forward model to small changes. The rows of $\mathbf{K}_x$ describe how a unit change of the species to be retrieved causes changes in the forward model and thereby in the spectrum or how changes of one point in the spectrum modify the profile. The rows of $\mathbf{K}_b$ describe the sensitivity of the forward model to small variations in the model parameters.

The forward model calculates a theoretical line spectrum of the true profile for each altitude. These altitude spectra are then added up to create a total spectrum for all altitudes that can be compared to a measured spectrum. If we imagine the forward model in reverse, then a measured spectra (which include all heights) can be decomposed into a linear combination of individual height spectra. From these altitude spectra the forward model calculates the species concentration at each height. This implies that the vertical profile of a species is influenced by the number of heights included, or how fine the vertical grid is.

### 2.6.2 The inverse model

The forward model has to be inverted to retrieve the altitude profile from a measurement. Due to measurement errors, the inversion of the instrumental part of the model is not unique. Therefore approximate solutions have to be found, based on fitting techniques as the least squares fit. The vertical profile to be retrieved is by nature a continuous function, but measuring techniques only allow a discrete number of points to be represented. The atmosphere is therefore divided in discrete layers with a selected thickness. The retrieval grid is usually coarse in respect to the absorption grid of the forward model. The retrieved vertical profile, $\widehat{\mathbf{x}}$, is related to the measurement by the inverse model, $\mathbf{I}$, or to the true profile by the transfer function, $\mathbf{T}$.

$$\widehat{\mathbf{x}} = \mathbf{I}(\mathbf{y}, \mathbf{b}, \mathbf{c}) = \mathbf{I}(\mathbf{F}(\mathbf{x}, \mathbf{b}), \mathbf{b}, \mathbf{c}) = \mathbf{T}(\mathbf{x}, \mathbf{b}, \mathbf{c})$$

where $\mathbf{c}$ is the vector of model parameters used in the retrieval but not in the forward model. The contribution functions describing the sensitivity of the solution to small changes are:

$$\mathbf{D_y} = \frac{\partial \mathbf{I}}{\partial \mathbf{y}} \qquad \mathbf{D_b} = \frac{\partial \mathbf{I}}{\partial \mathbf{b}} \qquad \mathbf{D_c} = \frac{\partial \mathbf{I}}{\partial \mathbf{c}}$$

where $\mathbf{D_y}$ represents sensitivity to changes in measurement spectrum, $\mathbf{D_b}$ sensitivity to the true model parameters (from the forward model), and $\mathbf{D_c}$ sensitivity to the model parameters of the retrieval. These contribution functions are generated by the retrieval method and not totally dependent on the radiative transfer and sensor characteristics. The inverse model can then be linearized around a reference state:

$$\widehat{\mathbf{x}} = \mathbf{I}(\overline{\mathbf{y}}, \widehat{\mathbf{b}}, \widehat{\mathbf{c}}) + \mathbf{D_y}(\mathbf{y} - \overline{\mathbf{y}}) + \mathbf{D_b}(\mathbf{b} - \widehat{\mathbf{b}}) + \mathbf{D_c}(\mathbf{c} - \widehat{\mathbf{c}})$$

where $\widehat{\mathbf{b}}$ and $\widehat{\mathbf{c}}$ are the model parameters at the reference state for the forward and the inverse model and $\overline{\mathbf{y}} = \mathbf{F}(\overline{\mathbf{x}}, \widehat{\mathbf{b}})$ is the estimated measurement spectrum at the reference state.

For non-linear problems an iteration process is used to get the retrieved profile:

$$\widehat{\mathbf{x}}^{\mathbf{i+1}} = \overline{\mathbf{x}} + \mathbf{D}_\mathbf{y}^\mathbf{i} \left( \mathbf{y} - \mathbf{F}(\widehat{\mathbf{x}}^\mathbf{i}, \widehat{\mathbf{b}}) + \mathbf{K}_\mathbf{x}^\mathbf{i}(\widehat{\mathbf{x}}^\mathbf{i} - \overline{\mathbf{x}}) \right)$$

Both $\mathbf{K}_x$ and $\mathbf{D}_y$ are recalculated at each iteration step and the process is stopped when the difference between two iterations $(\widehat{\mathbf{x}}^{\mathbf{i+1}} - \widehat{\mathbf{x}}^\mathbf{i})$ is smaller than an expected error.

### 2.6.3 Error characterization

The error sensitivity of the profile retrieval is not constant, and the error estimation method can put different weights on different parts of the spectrum to improve the accuracy. Error characterization can be achieved by the equation:

$$\widehat{\mathbf{x}} - \mathbf{x} = (\mathbf{A} - \mathbf{I})(\mathbf{x} - \overline{\mathbf{x}}) + \mathbf{D_y}\mathbf{K_b}(\mathbf{b} - \widehat{\mathbf{b}}) + \mathbf{D_y}\varepsilon_\mathbf{y}$$

where $\mathbf{A} = \mathbf{D_y}\mathbf{K_x}$ are called the averaging kernels, and $\mathbf{I}$ is the identity matrix. This equation splits the error in three terms representing the smoothing error, the forward model error and the measurement error, each them associated with the covariance matrices $\mathbf{S}_{\overline{\mathbf{x}}}, \mathbf{S_b}$ and $\mathbf{S}_\epsilon$.

The smoothing error of the first term is generated for limited vertical and horizontal resolution, including systematic and stochastic errors. It originates from the different

vertical resolutions of $\hat{\mathbf{x}}$ and $\mathbf{x}$, the first being a profile with degraded vertical resolution due to convolution with the averaging kernels.

The averaging kernels are matrix multiplications of the weighting function of the forward model for the selected species and the sensitivity to small changes of the measured spectrum. Together they describe how changes of concentration at a specific height affect other heights and can be seen as the spread in altitude. The altitude resolution of the fitted profile is determined from the full width at half maximum (FWHM) of the averaging kernels, as shown in figure 2.13.

In the case of limb sounding also averaging kernels for the horizontal plane are calculated defining the horizontal resolution. At limb sounding the integration is particularly sensitive to the resolution of the altitude grid and the length of the integration steps along the line of sight.

The forward model errors are produced by sources like the temperature profile, the spectroscopy data, the number of other species included and how the forward model is implemented.

The measurement errors are caused by inaccurate calibration, baseline ripple and thermal noise.

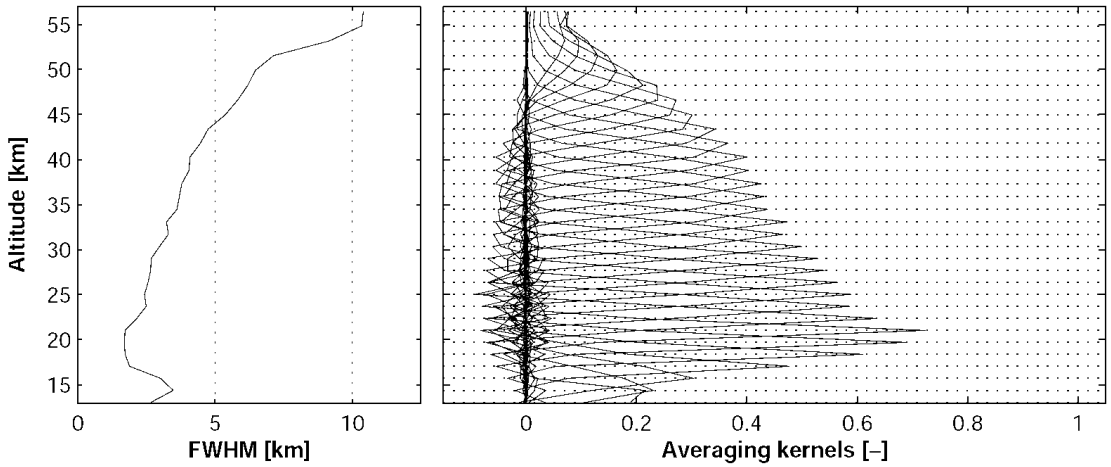


Figure 2.13: Full width at half maximum (FWHM) and averaging kernels for a hypothetical limb sensor measuring ozone emissions in the range 501.18-501.58 GHz. Adapted from *Eriksson et al.* [2005]

### 2.6.4 Optimal Estimation Method

The inversion of the spectra employs the optimal estimation method (OEM) developed by *Rodgers* [1976]. This algorithm utilizes the calculated spectrum from the forward model in conjunction with the measured spectrum, its covariance matrix and an a priori profile with

covariance matrix of its natural variations. The OEM method runs an iteration of least-squares fit until the deviation between measured and calculated spectra reach a predefined minimum. This method is efficient but can lead to unphysical profiles, and therefore an a priori profile of expected shape is used to guide the fitting process. The a priori profile is used at the parts where the measured profile is far from the expected a priori, with the reasoning that the measurement is affected by excessive noise. The a priori profile is generally utilized in the first iterations and thereafter the fitting is guided by the previous profiles.

# Chapter 3

# Odin

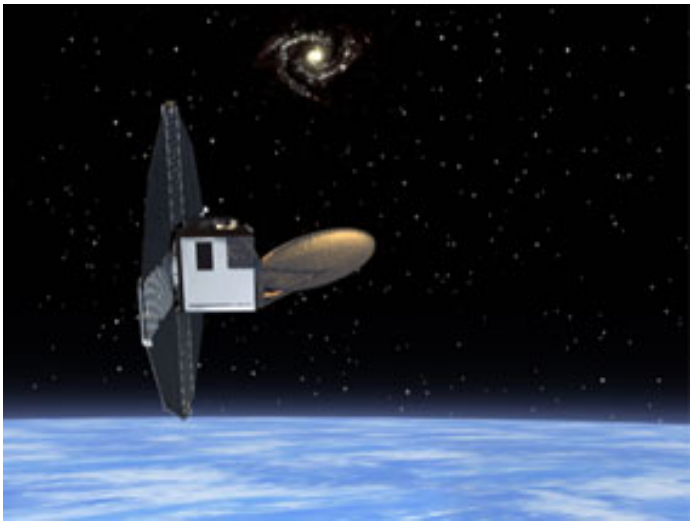

Figure 3.1: The Odin satellite. From the *Swedish Space Corporation* [2011]

## 3.1 Overview

The Odin satellite was developed by the Swedish Space Corporation (SSC) and launched in Feb 2001 as a joint venture between Sweden, Canada, France and Finland. It orbits the Earth about 15 times a day in a near polar, sun-synchronous circular orbit at an altitude of 600 Km with an inclination of $97.8^o$ and an ascending node at 18:00 local time. With an orbit close to the terminator line between night and day its solar panels are constantly directed towards the sun. Odin can de rotated and tilted in different directions. Half of the time it will be pointing towards the Earth scanning the atmosphere from 15 to 120 Km with up to 40 scans per orbit. The scans along the orbit have a spacing of about 500 Km. In this mode, Odin retrieves aeronomy data of ozone, monoxide, water vapor and

other constituents. The other half of the time it will be pointing out to space retrieving astronomical data, where it can be aiming continuously aiming at an object for up to 60 minutes. The Odin satellite carries a microwave radiometer featuring a telescope and five receivers in the mm and sub-mm range (SMR), and an optical spectrograph and Infrared Imaging System (OSIRIS) covering the range from UV to IR.

## 3.2 Sub Millimeter Radiometer (SMR)

In the aeronomy mode, the SMR measures atmospheric emissions in the sub millimeter range with a 1.1 m telescope pointing at the Earth's limb. The SMR uses 4 tuneable single-sideband Schottky diode heterodyne receivers and one fixed, with a back-end containing two high-resolution autocorrelator spectrometers (150 kHz-1 MHz). The frequency range of this instrument is a compromise between the aeronomy and astronomy communities covering the ranges 118.7, 486-504 and 541-581 GHz. The primary concern for the astronomical observations has been the sensitivity whereas the aeronomy observations focus on suppression of unwanted antenna lobes and receiver sidebands.

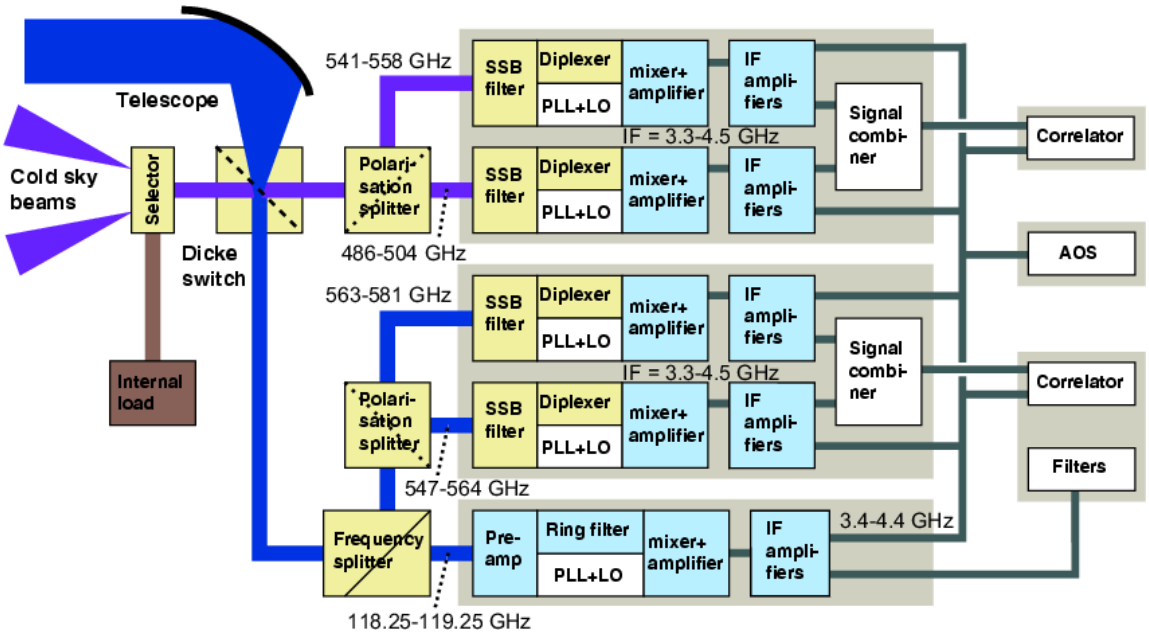


Figure 3.2: Block diagram of the SMR instrument. From *Frisk et al.* [2003]

Figure 3.2 shows the layout of the instrument with the signals traveling from left to right through different pathways depending on the frequency range. The high frequency signals from the telescope are fed through a Dicke switch, a set of single sideband filters (SSB), a diplexer (frequency domain) and a local oscillator, and a mixer to produce the intermediate frequency signals (IF). The IF signals are then amplified and routed to the back-end spectrometers (two autocorrelators and one acousto-optical (AOS) spectrometer).

An extensive description of the SMR instrument is given in the article by *Frisk et al.* [2003].

Within the aeronomy mode, there is a stratospheric mode where SMR scans at tangential heights from 7 to 70 Km with integration times of about one second (1.5 Km vertical resolution) in the stratosphere and 3.5 seconds in the mesosphere (6 Km vertical resolution). In this mode, profiles of $O_3$, $N_2O$ and ClO can be retrieved at the 501.8 GHz band. Ozone is measured at 20-50 Km in the 501.8 GHz band with a resolution of 2.5 Km and a precision of 25% per scan (0.5-1.5ppmv) [*Urban et al.*, 2004b]. In the stratomesospheric mode the SMR scans up to 110 Km at the limb with increased integration time retrieving profiles of CO and $O_3$ in the 576.9 GHz band.

The data is first processed to a level 1 as described by *Olberg et al.* [2003] and then to a level 2 with products described by *Merino* [2003]. The processing is done by using inversion techniques and the OEM, at the Chalmers University of Technology (Gothenburg, Sweden).

# Chapter 4

# Aura

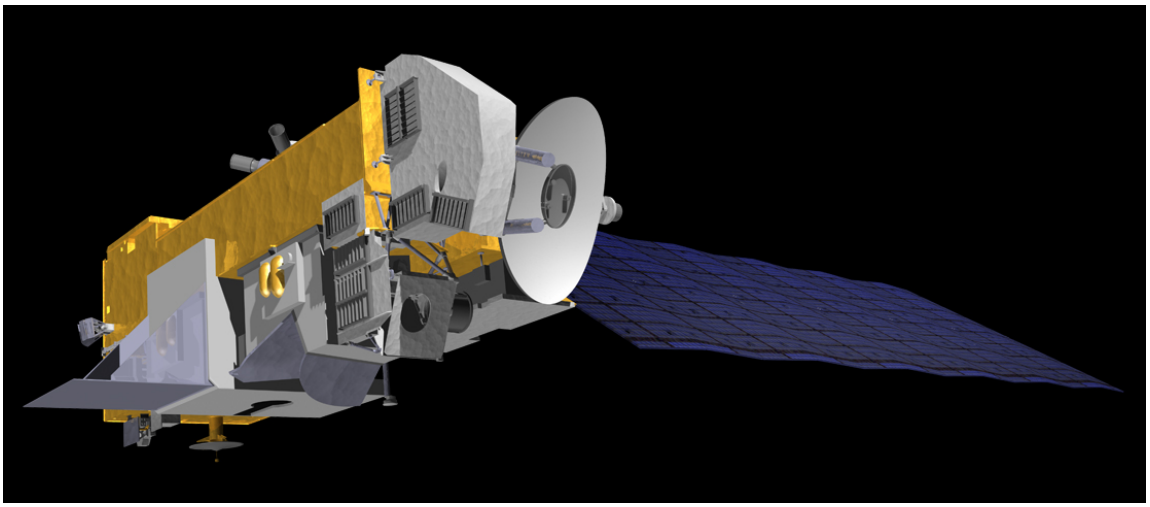

Figure 4.1: Artist's rendition of the Aura satellite [*NASA*, 2011]

## 4.1 Overview

Aura was launched in 2004 by the National Aeronautics and Space Administration (NASA) as a part of the Earth Science Projects Division, with the aim of monitoring the Earth's upper troposphere, stratosphere and mesosphere. The Aura satellite orbits the Earth about 15 times a day in a near-polar sun-synchronous orbit (-82$^o$ to +82$^o$) with a spacing between scans of 1.5$^o$ (about 165 Km) along the satellite track. The Aura orbit is at an inclination angle of 98$^o$ and at an altitude of 705 Km over the Earth with ascending node at 13:45 hours local time.

## 4.2 EOS Microwave Limb Sounder (MLS)

The Earth Observing System Microwave Limb Sounder (EOS MLS) on the Aura satellite measures the thermal emission in the millimeter and sub-millimeter range at the limb of the Earth. The Aura orbit causes a longitudinal separation between measurements of $10^o$-$20^o$ at middle and low latitudes and less spacing near the poles. Vertical profiles for up to 14 trace gases are retrieved from the MLS observations using the OEM algorithms as described by *Livesey* [2011]. The MLS retrieval algorithm includes a 2D method that subtracts overlapping sections of consecutive scans both vertically and horizontally

The instrument uses heterodyne radiometers to perform observations in broad spectral regions centered at 118, 190, 240 and 640 GHz, and 2.5 THz. The 240 GHz radiometer was chosen to measure the strong $O_3$ lines that lie in a spectral range where water vapor absorption in the upper troposphere is small. The 2.5 THz radiometer is at a clean spectral region with two strong OH lines.

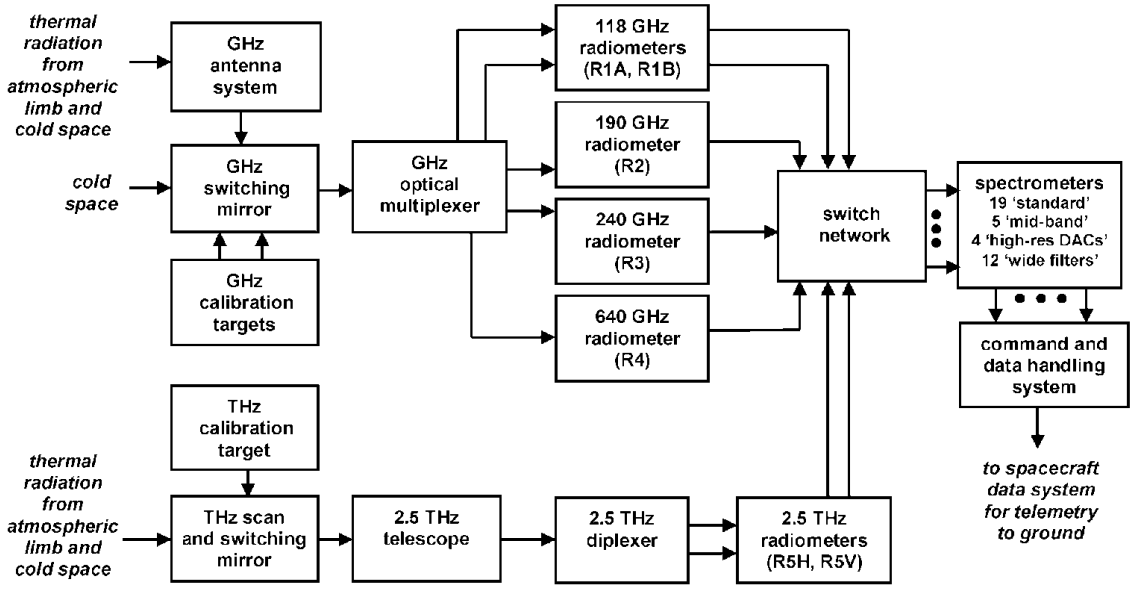


Figure 4.2: EOS MLS overall signal flow block diagrams from *Waters et al.* [2006]

The block diagram on figure 4.2 shows the incoming radiation from the vertical scans collected by a three-reflector offset antenna system that sends the signal to four radiometers. The GHz antenna system contains a mirror with vertical dimension of 1.6 m and for signals in the THz range a separate telescope and mirror of 25 cm is used.

The GHz antenna system is followed by a switching mirror for radiometric calibration, an optical multiplexer that separates the signal spatially with paths feeding the four GHz radiometers. These down-convert the incoming signals at radio frequencies to intermediate frequency bands (IF) of 3-21 GHz, and again down to 900 MHz. Thereafter, the broad IF signals are distributed by a switch network to four spectrometers. Each of them has

a different spectral resolution and bandwidth that separates the signals into channels. [*Waters et al.*, 2006].

The MLS version 3.3 $O_3$ standard product is taken from the 240-GHz retrieval with high sensitivities at the upper troposphere and at the mesosphere (261-0.02 h Pa).

The width of the averaging kernels on figure 4.3 show a vertical resolution for $O_3$ of about 2.5 Km in the upper troposphere and stratosphere degrading to 4-6 Km in the mesosphere. The horizontal resolution along the satellite track is of 300-450 Km in the stratosphere and of about 200-500 Km in the mesosphere. As seen from the figure, the fine vertical grid in the lower altitudes is at a cost of poorer horizontal resolution.

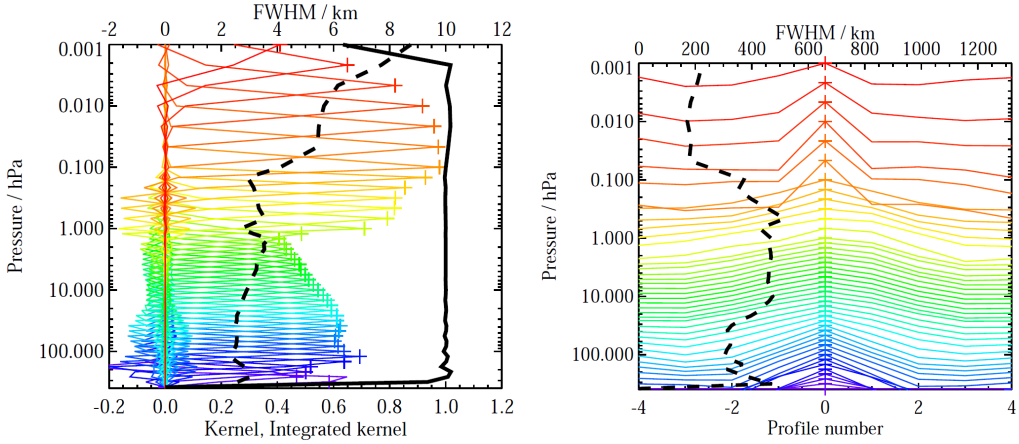


Figure 4.3: Typical averaging kernels for the MLS v3.3 $O_3$ at the equator as a function of retrieval levels. The dashed black line indicates the resolution from the FWHM of the kernels and the solid black line shows the integrated area under each kernel. Values near unity imply that the majority of information for that point has come from the measurements and not a priori information. On the left, vertical averaging kernels and resolution were integrated from five profiles along the track. On the right the horizontal averaging kernels and resolution were integrated in the vertical direction. From *Livesey* [2011]

The precision (scan to scan) of the $O_3$ profiles is 7 % at the stratopause worsening gradually to more than a 100% at the mesopause.

The OH standard product is measured by the THz radiometer in the 2.5 THz spectral region. The nighttime vertical resolution is higher than at daytime with values of about 2.5 Km at the stratosphere and mesosphere as shown in figure 4.4. The horizontal resolution derived from the FWHM is less than 200 Km equivalent to the width of $1.5^o$ (165 Km) along the satellite track. Above 70 Km the faster scan rate of the instrument degrades slightly the vertical resolution.

The relative precisions for an OH zonal mean in $10^o$ latitude bins is better than 10% with one day of data from the middle stratosphere to the mesopause.[*Livesey*, 2011]

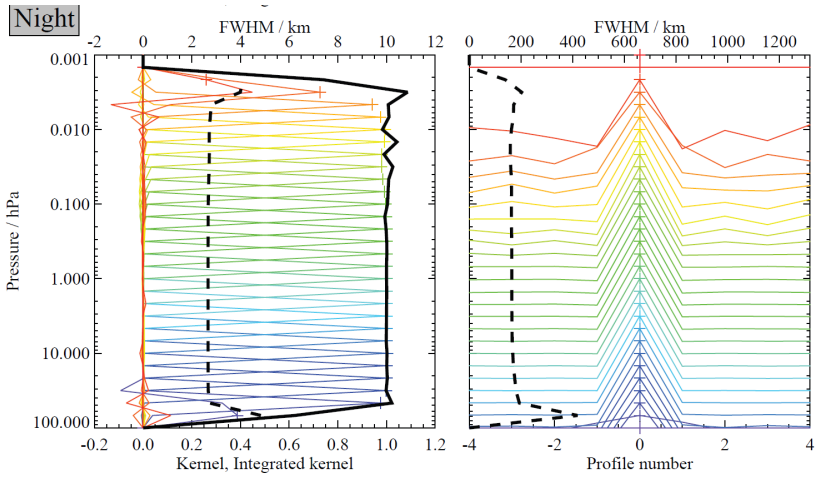


Figure 4.4: Typical averaging kernels for the MLS v3.3 OH at 35$^o$N for nighttime as a function of retrieval levels. The dashed black line indicates the resolution from the FWHM of the kernels and the solid black line shows the integrated area under each kernel. Values near unity imply that the majority of information for that point has come from the measurements and not a priori information. On the left, vertical averaging kernels and resolution were integrated from five profiles along the track. On the right the horizontal averaging kernels and resolution were integrated in the vertical direction. From *Livesey* [2011]

# Chapter 5

# Results

The $O_3$ and OH data of an eleven-day period obtained from the Odin/SMR and Aura/MLS instruments was analyzed in three different ways:

- Polar and cylindrical plots of the Southern hemisphere. Plotted in geographic and geomagnetic coordinate systems.
- Zonal mean plots. Plotted as a function of geomagnetic latitude.
- Time series plots. Plotted at geomagnetic latitude $62^o$ S. For comparison with ground-based data from the Troll station.

The choice of coordinate system is a relevant issue in the study of particle precipitation. On one hand the EEPs precipitate in symmetric rings around the geomagnetic poles where the earths magnetic field lines end. On the other hand the terminator line is symmetric around the geographic poles and the photochemical processes involving solar radiation occur here. Most literature covered concerning EEP precipitation uses geographic coordinate systems but in this project all the data has been translated to geomagnetic coordinates with the aim to compare maps of ozone depletion with the geographic extent of precipitation events.

## 5.1 Data processing

All tools for data processing and plotting on this project were developed on Matlab 7.11.0 (R2010b).

The data analysis of this project was done for the period 17-27 of July. A five-day period prior to the peak of the storm (17-21 of July) was selected to normalize the data of the six days after the storm (22-27 of July). The post-storm data is presented both as absolute values, and as relative changes compared to the five-day pre-storm period.

The main program allows a selection of different species, spectral frequencies and periods of time depending on the satellite.

The daily HDF-EOS data (Hierarchical Data Format - Earth Observing System) from the Odin/SMR [*Chalmers University of Technology*, 2011] and the Aura/MLS [*Jet Propulsion Laboratory*, 2011a] instruments was read and analyzed by a subroutine that rearranges the data into new structures containing selected parameters. The organization of the reported data from the satellites differs, each requiring separate selection and processing.

### 5.1.1 Odin/SMR

The SMR level 2 data of Odin uses the HDF-EOS library 2.5. The raw data is stored in a single file per orbit containing 40-45 scans each. The selected day is compared to the average modified julian date for each scan and saved if it matches and if the Quality flag is set to zero (good retrieval). Good retrieval means a good convergence of the retrieval and a measurement response greater than 0.75 ensuring that little data comes from apriori values. For latitudes on the southern hemisphere a conversion to geomagnetic coordinates is made on each scan. The conversion subroutine first converts the geographic coordinates to geocentric coordinates. Employing the IGRF (International Geomagnetic Reference Field) coordinates for the geomagnetic North pole year 2009, the conversion from geocentric to geomagnetic coordinates is carried out. This conversion applies the cosine and sine rules to a spherical triangle and checks for obtuse angles to determine the quadrant. The coordinate translation was verified by comparison with the online calculator at WDC of Geomagnetism, Kyoto [*WDC for Geomagnetism*, 2009b]. Finally a new structure file is created that includes relevant information for this project such as geomagnetic latitude and longitude, solar zenith angle, altitudes and mixing ratios.

The 501.8 GHz ozone line from the Odin/SMR instrument was retreived in the Stratospheric mode and therefore has limited data at altitudes of the middle mesosphere. The Odin/SMR instrument also provides a mesospheric mode with the 557.0 GHz ozone line but due to switching between modes data for the period of interest was unavailable. Since the Odin satellite orbit follows the terminator line of the earth, the retrieved ozone data spans the solar zenith angles from about $100^o$ to $120^o$.

### 5.1.2 Aura/MLS

The retrieved MLS Level 2 (v3.3) data of Aura is in HDF-EOS version 5 format. It contains the geophysical products reported along the instrument track generated from the Level 1 data. The data is reported on a daily basis (from midnight to midnight, universal time) and named with the date of the observation. The species selected for this project were $O_3$ at the 240 GHz spectral region and OH at the 2.5 THz spectral region. Each data point is selected if it has met a *Quality* and *Convergence* requirement as described by *Livesey* [2011]. The *Quality* measures the fit achieved by the Level 2 algorithms to the relevant radiances and needs to pass a threshold. The *Convergence* reports the degree of fitting to

the radiances compared to an expected linear fit. The pressure data grid is converted to altitude by interpolation to the altitude grid used in the Odin/SMR data.

## 5.2 Particle precipitation

A Coronal Mass Ejection (CME) of the sun produced EEPs that arrived at the Earth's atmosphere on the 22 of July 2009 causing a moderate geomagnetic storm. This event was registered by the WDC of Geomagnetism, Kyoto, showing a decrease of the DST-index down to -79 nT. In figure 5.1 the DST-index variations are displayed for the month of July 2009. The figure shows a dip for the 22 of July which corresponds to a moderate storm, lasting for one and a half day and followed by a recovery phase.

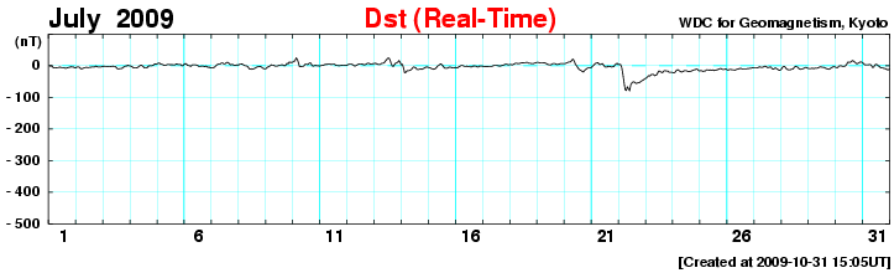


Figure 5.1: Hourly Equatorial DST-index of July 2009.[*WDC for Geomagnetism*, 2009a]

Figure 5.2 shows the geographic extent of precipitating electrons (>30 keV) and protons (80-240 keV) that was registered by NOAA satellites in the period 22-24 July 2009. The precipitation of electrons and protons show the highest amount near the poles following the lines of magnetic longitude. The large area of precipitation over South America is related to the South Atlantic Anomaly (SAA), an area of weak magnetic field. Field strength variations around the poles leads to an uneven longitudinal distribution of precipitation.

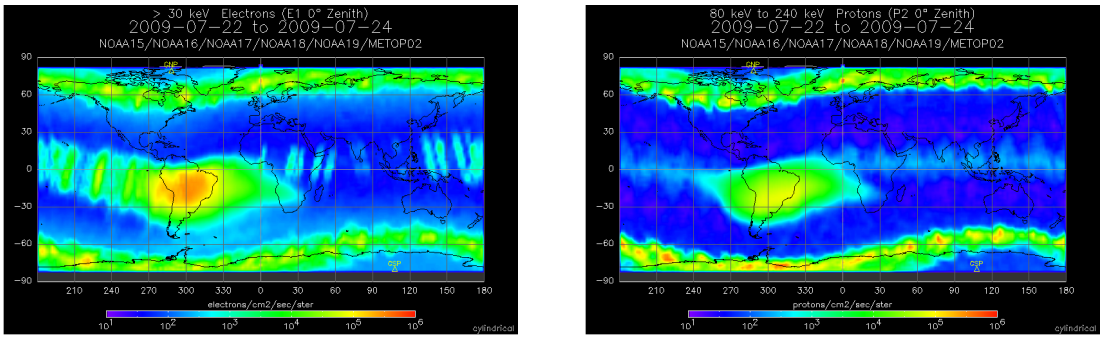


Figure 5.2: Geographic maps of precipitating electrons (>30 keV) and precipitating protons (80-240 keV) in the period 22-24 July 2009 observed by NOAA satellites [*NOAA*, 2010]

## 5.3 SH polar and cylindrical ozone maps

The ozone data retrieved by the Odin/SMR and Aura/MLS instruments was first linearly interpolated vertically to the selected level. Then the horizontally irregulary spaced data sampled along the orbital tracks was interpolated using a linear Delaunay triangulation method to a uniform grid. The grid resolution was of one degree latitude by one degree longitude covering the latitudes 0 to 90$^o$ S and longitudes 180W to 180E. Only data points of solar zenith angles greater than 105 $^o$ representing night time values were plotted.

The $O_3$ mixing ratio of the five-day period prior to the storm is depicted in figure 5.3. The polar and cylindrical maps are drawn at an altitude level of 72 Km and in geomagnetic coordinates. The polar map is centered at the geomagnetic south pole and rotated such that the zero degree magnetic longitude meridian points to the north. Note the coastlines and a black spot marking the location of the Troll station. Areas of white are mostly caused by missing data and interpolation over the poles is likely to be misleading. The satellites pass at geographic latitudes not greater than about 80$^o$ S and therefore interpolation of data over the poles can happen between points with a spacing of up to 20$^o$ latitude.

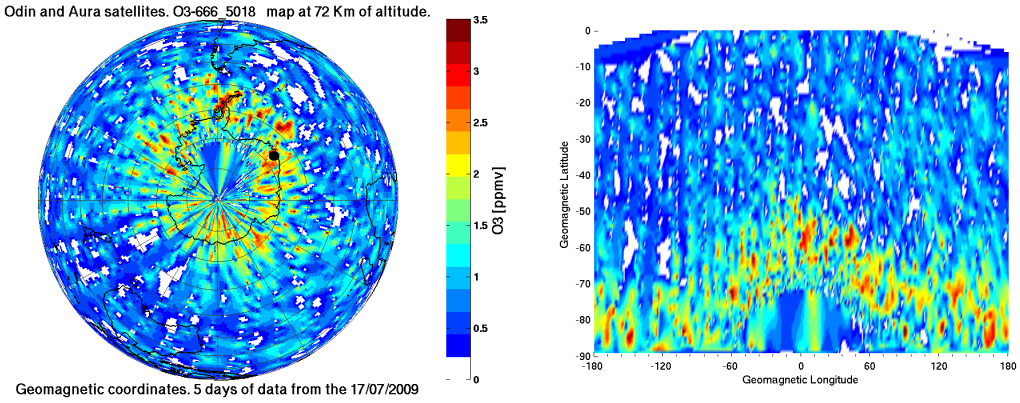


Figure 5.3: SH polar and cylindrical maps of ozone mixing ratio for the 17-21 July 2009 at 72 Km altitude. Geomagnetic coordinates

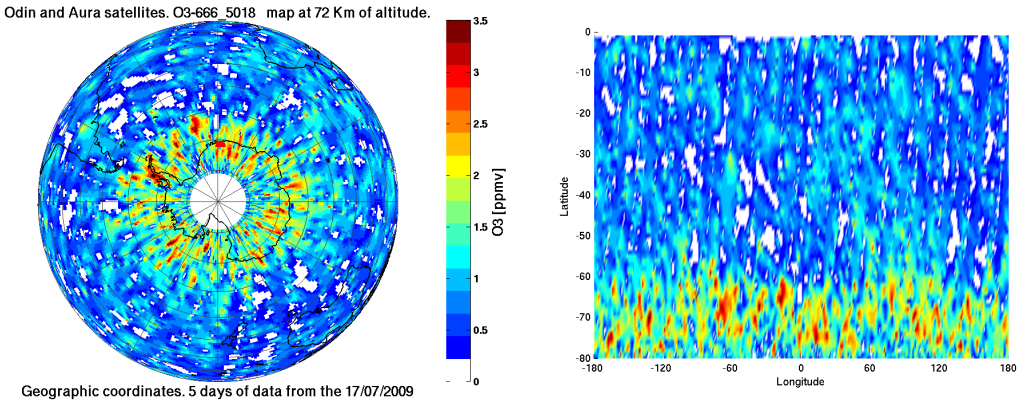


Figure 5.4: SH polar and cylindrical maps of ozone mixing ratio for the 17-21 July 2009 at 72 Km altitude. Geographic coordinates

Figure 5.3 shows ozone mixing ratios of up to 3.5 in the areas of maximum vmr. This area appears to be an asymmetric band at geomagnetic latitudes extending from $90^o$ S to $50^o$ S. Plotting the same data in maps using geographic coordinates (figure 5.4) we see that the area of maximum ozone mixing ratios is located in a belt around the geographic south pole at geographic latitudes $70^o$ S to $\pm$ $10^o$. This indicates that there is a coherent structure in geographic coordinates.

In figure 5.5 the daily polar and cylindrical ozone maps for the 23-24 July 2009 after the storm are depicted as relative changes in percent from the values prior to the storm. That is the post-storm value subtracted the pre-storm value and divided by the pre-storm value, all multiplied by hundred. Even though there seems to be an overall depletion of ozone in the MMM (more blue than red) no distinct pattern was found. Areas of depletion are not uniformly connected containing many scattered patches of increase. Only a couple of days are shown here but a look through the plots of the days that follow (Appendix C) leads to a similar conclusion. Altitudes from 65 to 75 were studied analogously (not presented here) and a change from percent to vmr was also tested still with no recognizable pattern. The reason for these scattered maps can be due to the large geographic variability of mesospheric ozone and due to the limited number of satellite observations.

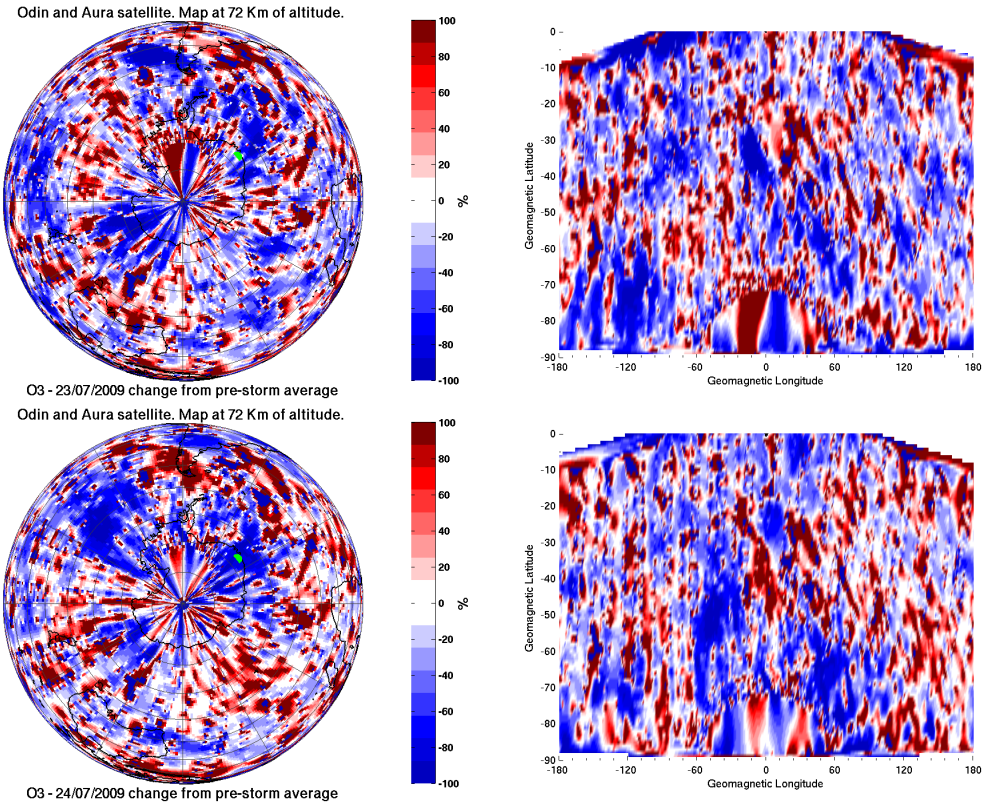


Figure 5.5: Daily polar and cylindrical ozone maps (23-24 July 2009) in percentage change from the five day average pre-storm at altitude 72 Km. All plots are in geomagnetic coordinates and after the storm

All the daily polar and cylindrical ozone maps for the eleven-day period are found in

Appendix C in both geographic and geomagnetic coordinates.

## 5.4 Zonal means

The $O_3$ and OH data retrieved by the Odin/SMR and Aura/MLS instruments were first linearly interpolated to a vertical grid of altitudes in the interval 50-90 Km with 5 Km distance between grid-points. The data was then averaged in bins of five degrees geomagnetic latitude for each altitude level and finally plotted with the pseudo-color matlab routine assigning colors to a rectangular array of cells and using linear interpolation between them. It has to be pointed out that the zonal means after the storm can be slightly shifted in geographic latitudes and altitude in respect to the pre-storm average due to seasonal changes (changes in the terminator line). In geomagnetic latitudes this effect causes a slight mearing of the data.

### 5.4.1 O3

Figure 5.6 shows the zonal mean of ozone in vmr for an average of five days pre-storm (17-21 July 2009). The highest mixing ratios are seen at the mesopause and the stratopause but also at the middle mesosphere for geomagnetic latitudes higher than $65^o$ S. At about 80 km of altitude the figure shows a minimum that prevails down to low geomagnetic latitudes.

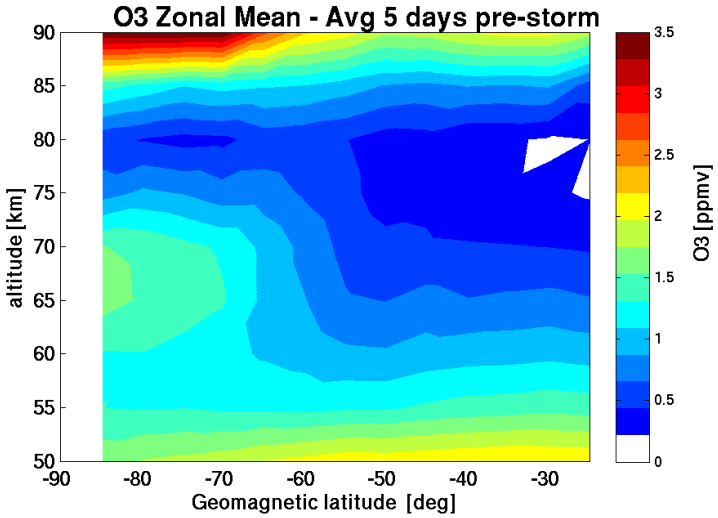


Figure 5.6: Ozone zonal mean in ppmv. Average of the five days pre-storm (17-21 July 2009)

The following figures 5.7 and 5.8 show the daily zonal means of the days after the storm in absolute values and in percentage change from the five-day pre-storm period. The two are presented together since a percentage change can be misleading if the absolute value is small.

A serious increase of ozone at altitudes above 80 Km (values of up to 50%) is visible from the 22th of July to the 26th of July extending gradually from high to low geomagnetic latitudes ($30^o$ S).

From the 23 to the 26 July 2009 a gradual decrease of ozone of the order 30-50% is observed at altitudes 67-77 Km starting at latitude $60^o$ S and later extending to both high and mid geomagnetic latitudes. The ozone depletion starts to recover on the 27th where the loss seems to drift downwards in altitude and only affect high geomagnetic latitudes. From the 24th to the 26th a substantial loss is also seen at altitudes under 75 Km for mid/low latitudes ($< 70^o$ S).

Another feature that can be observed in the figures is what appears to be a vertical oscillation of the maximum at the mesopause with an amplitude of about 5km.

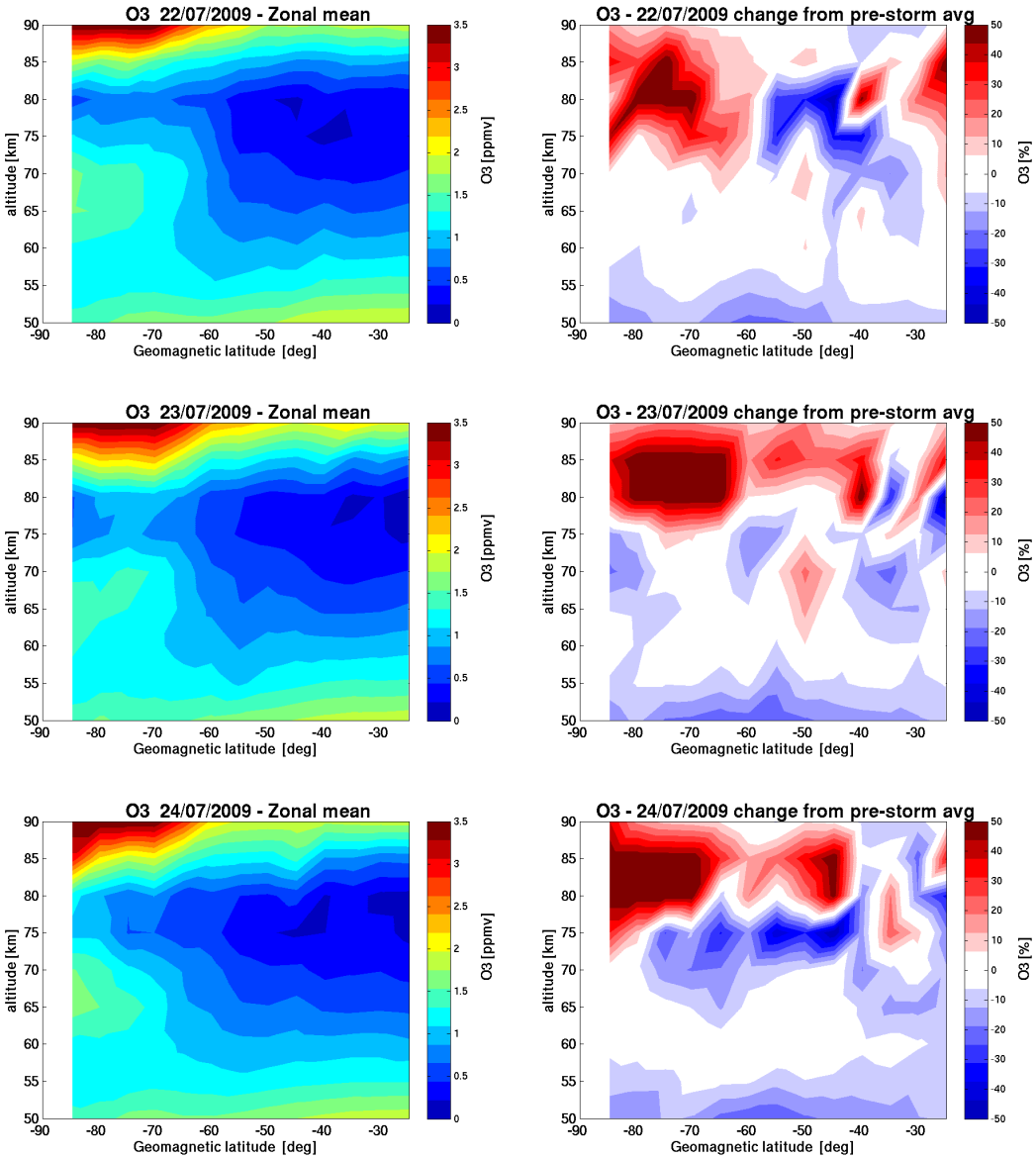


Figure 5.7: O3 daily zonal means (22-24 July 2009) in ppmv after the storm and percentage change from the five day average pre-storm

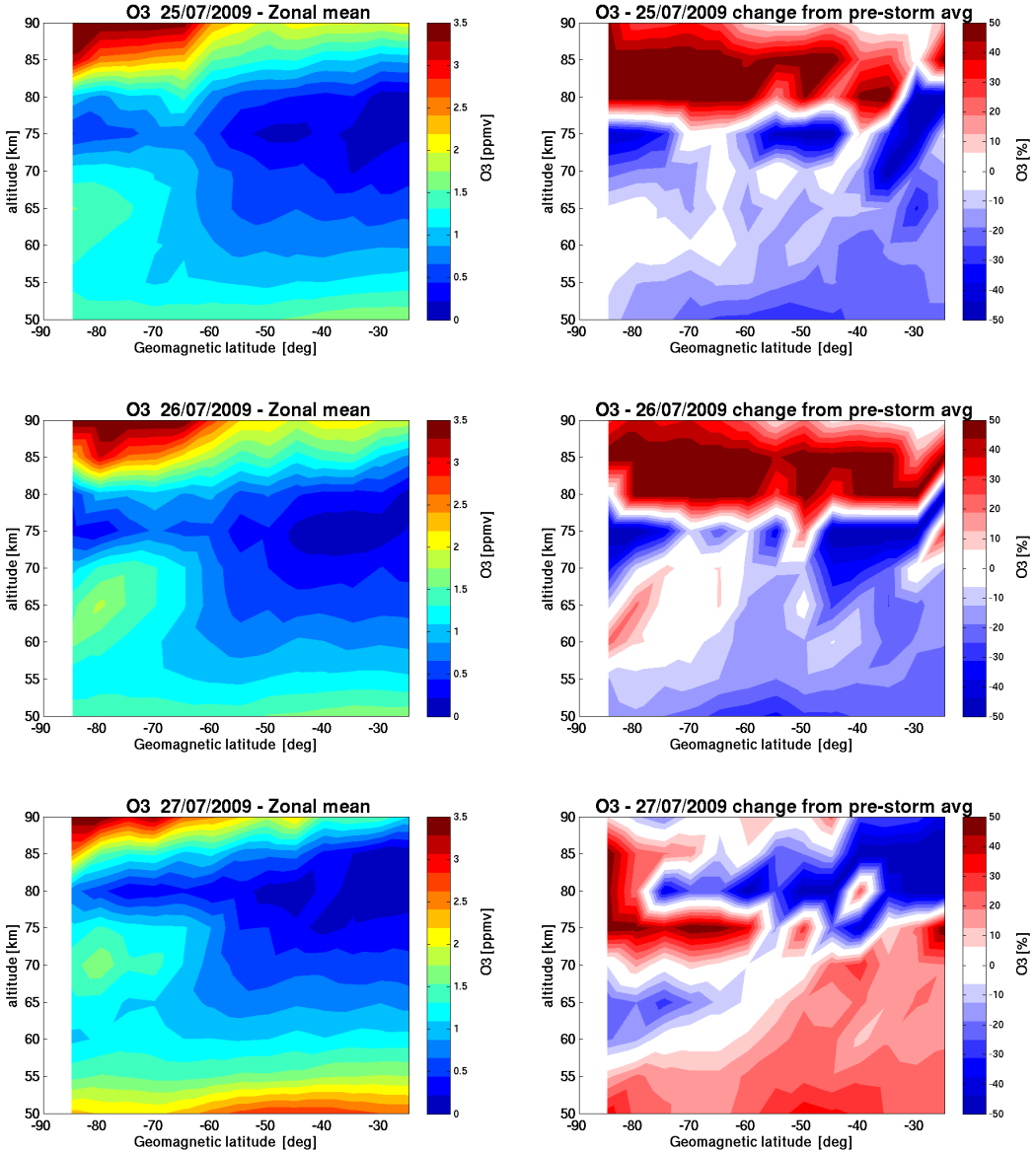


Figure 5.8: O3 daily zonal means (25-27 July 2009) in ppmv after the storm and percentage change from the five day average pre-storm

### 5.4.2 OH

The OH data from the Aura/MLS instrument is reported in vmr and has not been converted to the standard density units ($10^6$ cm$^{-3}$) for consistency with the ozone retrievals. Figure 5.9 shows the zonal mean of hydroxyl in vmr for an average of five days pre-storm (17-21 July 2009). High mixing ratios of OH are shown at altitude levels around 80 Km extending from high to low geomagnetic latitudes. The vmr values are particularly high at lower geomagnetic latitudes for this level. There also seems to be a vertical symmetry about this level for high geomagnetic latitudes ($> 60^o$ S) and a latitudinal gradient to lower latitudes. The figure also show a characteristic 'bump' of low concentrations of OH at altitudes 70 to 75 Km between latitudes $70^o$ S and $60^o$ S.

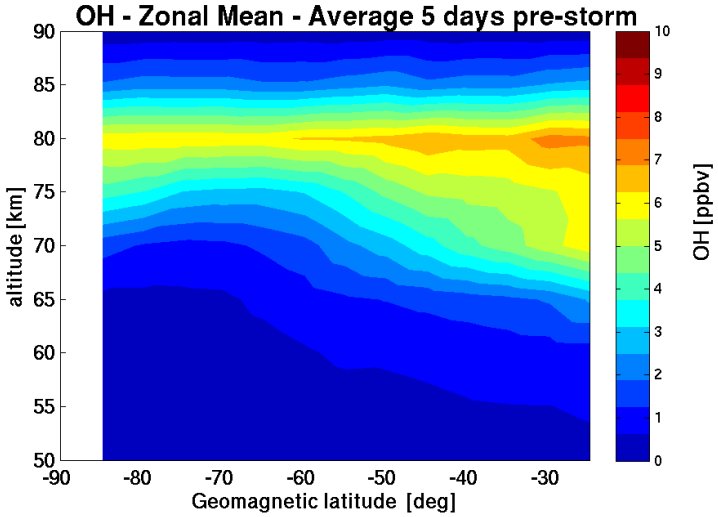


Figure 5.9: OH zonal mean in ppbv. Average of the five days pre-storm (17-21 July 2009)

The figures of the following pages (figures 5.10 and 5.11) display the data after the storm in vmr and in relative change, that is, subtracted the five-day pre-storm average and divided by the pre-storm average. The change is represented as values in ppbv and not in percent to better quantify changes of significant difference in vmr. An increase from 0.1 ppbv to 0.2 ppbv would show a 100% increase in percent but only a minor increase in mixing ratio. This makes the plots look 'cleaner' with patches only visible for the major changes.

The figures on the left columns from the 22-26 of July 2009 show a latitudinal gradient starting at the pole for altitudes up to 80 Km caused by the disappearance of the earlier mentioned 'bump' which then reappears the 27th of July. The figures on the right columns display relative changes of hydroxyl and show a significant increase at levels 70 to 75 Km for latitudes $70^o$ S to $60^o$ S just after the storm. The increased mixing ratios at this level are at their maximum the day after the storm and seem to gradually fade the following days. The 27th of July there is no visible hydroxyl increase at high latitudes and the low

mixing ratios (the 'bump') at these levels reappear.

From both the left and right column of the figures it is clear that the amount of hydroxyl decreases by 1ppbv and more above the 80 Km altitude level compared to the pre-storm average. As the days pass this loss deepens and extends to levels from 75 to 90 Km, still being present six days after the storm.

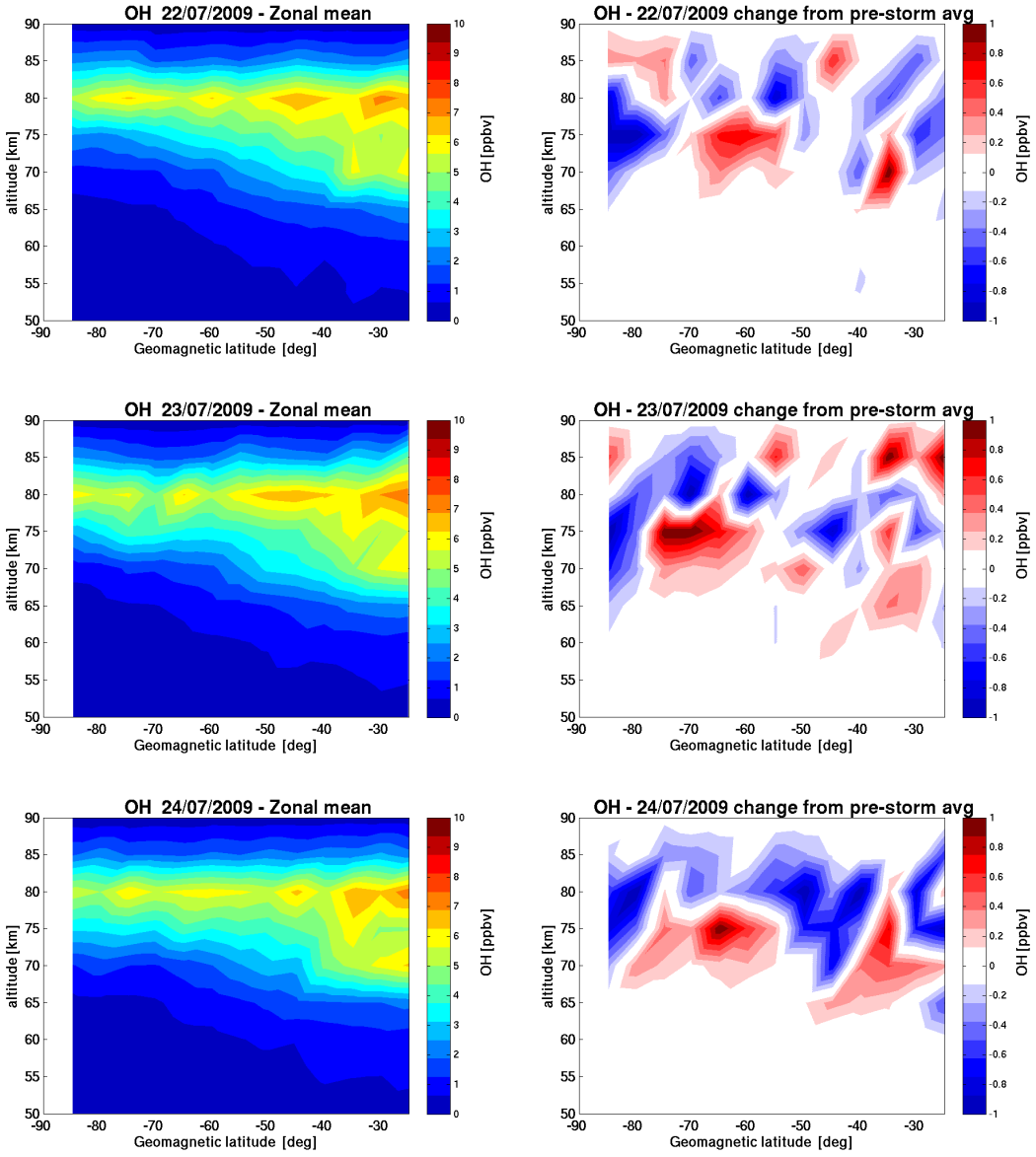


Figure 5.10: OH daily zonal means (22-24 July 2009) in ppbv after the storm and absolute change in ppbv from the five day average pre-storm

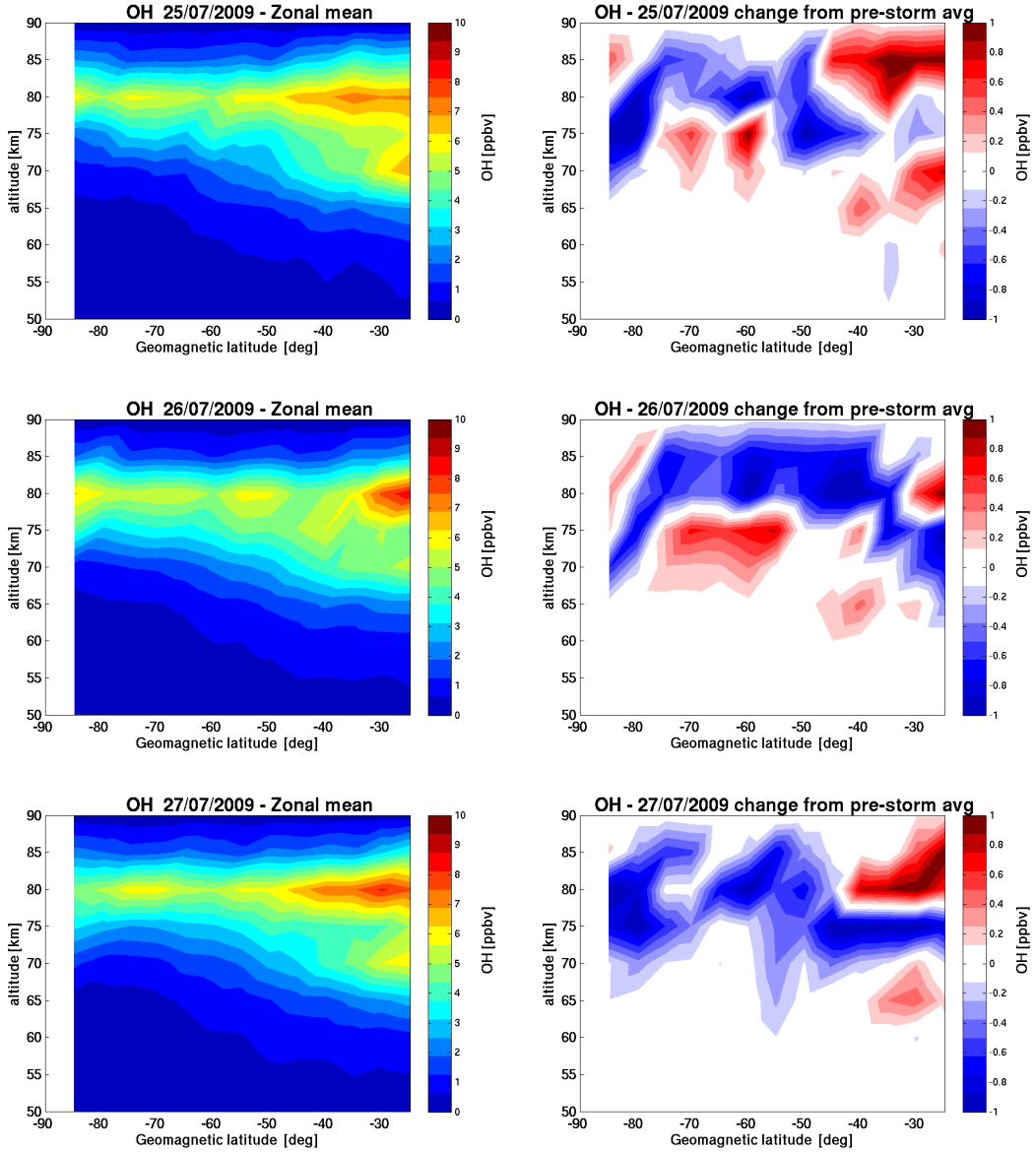


Figure 5.11: OH daily zonal means (25-27 July 2009) in ppbv after the storm and absolute change in ppbv from the five day average pre-storm

## 5.5 Time series

The time series of O3 and OH are presented at the selected geomagnetic latitude $62^o$ S on figure 5.12 in vmr and percentage change. At this geomagnetic latitude ground-based observations have been carried out for the same time period from a microwave radiometer (Troll station). The $O_3$ and OH data retrieved by the Odin/SMR and Aura/MLS instruments were linearly interpolated to a vertical grid as for the zonal means. The data were then averaged in bins of whole days and finally plotted to a rectangular array of cells and interpolated. Compared to the zonal means these plots display more discontinuities due to greater data variability from day to day. The figures could have been made on a shorter time period with higher temporal resolution (hours) for species with short lifetimes such as O3 and OH, but would then be dominated by diurnal variability.

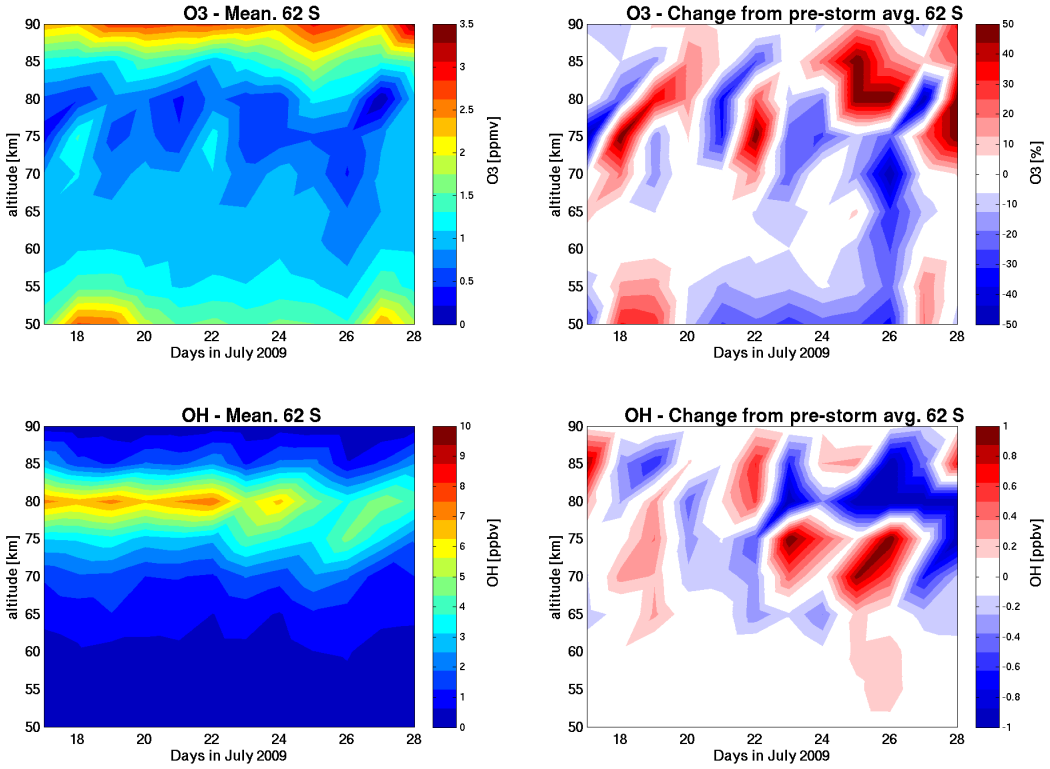


Figure 5.12: On first column daily means (17-28 July 2009) of O3 and OH at geomagnetic latitude $62^o$ S plotted in time. Second column shows difference plots from the five day average pre-storm (17-21 July 2009) in percent (O3) and absolute change (OH).

The two figures on the left column show similar patterns if we think of the OH plot as the inverse of the O3 plot. O3 losses at levels around 80 Km match the high amount of OH at these levels. The high mixing ratios of ozone at the mesopause and stratopause are coincident with very low levels of hydroxyl at these levels. Even though a symmetry around the 80 Km level seems to be maintained for hydroxyl over the observed time period,

this is not the case for ozone. The ozone loss seems to descend gradually down to altitudes of about 60 Km.

The figures on the right column show a percentage change for ozone and change in vmr for hydroxyl. On July 22 there seems to be a considerable increase of ozone at levels 70-80 Km turning to a loss of about 20 % in the following two days. This loss descends to levels about 55-75 Km reaching a 50 % decrease from the 25-27 of July, and finally disappears by the 28th of July. An ozone increase of up to 50 % is seen on levels about 77-90 Km which lasts from the 24 to the 26 of July 2009. The figure of hydroxyl-changes reveals a considerable increase at the levels 67-77 Km for two days after the storm. Another significant increase of hydroxyl is observed at slightly lower levels lasting from the 25th to the 26th of July 2009. The two patches of increased hydroxyl can be localized about the same altitudes and time periods as the previously mentioned ozone losses. The presented time series are consistent with the zonal means displayed in figures 5.7, 5.8 and figures 5.10, 5.11 for the selected latitude.

# Chapter 6

# Discussion

The SH polar and cylindrical maps for ozone for the five days pre-storm (figures 5.3 and 5.4) show the features of ozone at an altitude of 72 Km. The areas of highest concentration are consistent with calculations of the MMM by *Hartogh et al.* [2004] which suggest a latitudinal band of 15 degrees near the polar night terminator at heights 66-76 Km.

When the storm of the 22 July 2009 precipitates over the south pole, the overall relative change of ozone for geomagnetic latitudes greater than $60^o$ S seems to be up to 50 % at an altitude level of 72 Km (figure 5.5). The geographical variability of ozone and restricted satellite coverage, made it difficult to observe storm effects on ozone in a latitudinal/longitudinal scale. But the overall tendency of ozone depletion for magnetic latitudes greater than $60^o$ S proposed a different way to plot the data, displaying it in the form of zonal means for geomagnetic latitudes.

For ozone, the zonal mean of the five day average prior to the storm (figure 5.6) shows the second ozone maximum at about altitude level 90 Km. The strong latitudinal gradients near this level has previously been reported by [*Barth et al.*, 1983] suggesting as an explanation a downward transport of $O_x$ from the thermosphere caused by vertical mixing [*Solomon et al.*, 1982]. The high values near the stratopause are caused by the extension of the first maximum from the stratosphere. The MMM is also seen as a an area of high ozone centered at altitude levels 65-70 Km for latitudes higher than $65^o$ S.

The post-storm zonal means of ozone show a distinct increase (more than 50%) above 80 Km and a decrease of 30-50% below, lasting for four days at magnetic latitudes greater than $60^o$ S. The ozone depletion remains at this level a couple of days and then descends into the polar vortex.

The large increase of ozone at the 80-90 Km levels is caused by the big amount of atomic oxygen created in the mesosphere/thermosphere during particle precipitation. The effect on mesospheric ozone and oxygen of auroral events has nicely been described by *Maeda and Aikin* [1968]. Precipitating electrons of energies of more than 100 keV can cause significant changes on mesospheric ozone and atomic oxygen by molecular oxygen

dissociation. Furthermore, lower energy electrons cause ionization of $O_2$ which in turn is destroyed by the associative reaction:

$$O_2^- + O \rightarrow O_3 + e \tag{6.1}$$

Obviously this reaction is totally dependent on the atomic oxygen concentration and can therefore not continue in the polar winter regions without transport from sunlit areas or from continuous EEP precipitation. Figure 6.1 shows the calculated dissociation rate of molecular oxygen for a low and a moderate energy precipitation event at different heights. The dissociation rate is seen to be zero for altitudes below 80 Km for low energy electrons

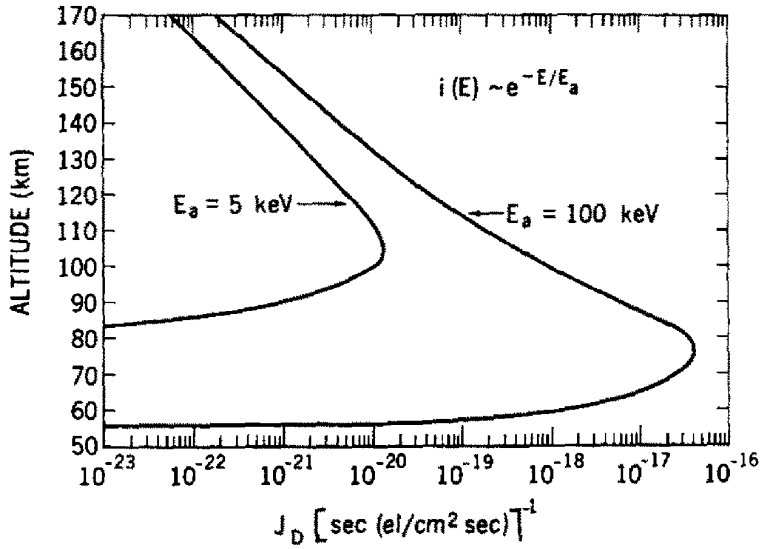


Figure 6.1: Rate of $O_2$ dissociation by auroral electrons with energies 5 keV and 100 keV. [*Maeda and Aikin*, 1968]

(5 keV) and as the electron energy is increased to 100 keV high dissociation rates are seen down to 55 Km.

From the day the storm sets on, the rise of the hydroxyl concentration at levels 70-75 Km indicate an instantaneous increase of $HO_x$ by the ionization effect. The increased OH production vanishes as quick as the storm is over. Most of the ions created by EEP precipitation from $O_2$ and $N_2$ end up as $O_2^+$ ions [*Verronen et al.*, 2006]. $HO_x$ is produced via $O_4^+$ by hydration and recombination and depends on water cluster ions. The number of odd hydrogen radicals created per $O_2^+$ ion above 75 Km varies depending on the ionization rate, the water vapor density and the amount of atomic oxygen. For reasonable values of the ionization rate the $HO_x$ produced per ionization is about two for altitude levels below 60 Km and about one for altitudes around 80 Km (assuming an ionization rate of $10^3$ $cm^{-1}$ $sec^{-1}$). The ionization rate of $HO_x$ falls with altitude as the densities of $H_2O$ and $O_2$ decrease [*Solomon et al.*, 1982]. This effect is seen on the data (figures 5.10 and 5.11) for mid- to high latitudes where the highest hydroxyl increases happen under 80 Km as previously reported by *Verronen et al.* [2006].

By comparison of the daily changes of hydroxyl and ozone following the storm, there is a high concordance between areas of rising hydroxyl and areas of ozone depletion. This is seen most clearly at altitudes above 80 Km where a decrease in hydroxyl causes ozone to raise by up to 50 %. Under 80 Km the ozone depletion is also occurring at latitudes with increased hydroxyl production. The fading effect on the MMM after the storm for the ozone mixing ratios is in agreement with previous findings for high energetic solar storms where the MMM totally disappears [*Jackman et al.*, 2001; *Rohen et al.*, 2005; *Seppala et al.*, 2006]. Due to a low concentration of $HO_x$ at latitudes near the polar night terminator, a moderate energetic precipitation event can produce amounts of $HO_x$ comparable to what can produced naturally at daylight *Sofieva and et al.* [2009]. The zonal means indicate that hydroxyl causes the initial ozone loss, but vanishes quickly. Nevertheless, the ozone loss persists and descends in the polar vortex indicating that another species (probably $NO_x$) is causing the continuing depletion.

The time series for geomagnetic latitude 62 $^o$S (figure 5.12) reveal an immediate ozone increase at 75 Km height on the day of the storm followed by a loss for the four days that follow. This loss seems to descend gradually in altitude down to 60 Km. The hydroxyl concentration increases in roughly the same altitudes for these days, again suggesting that the ozone depletion is a result of catalytic cycles with OH.

The ground-based data from a microwave radiometer located at Troll, Antarctica (-72$^o$ S, 2.5$^o$E, 1000m) is compared to the obtained satellite data. The relative change of ozone in percent is shown on figures 6.2 and 6.3 for July and August 2009. The time period studied in this project is inside the black frame and the onset of the storm is displayed with a blue line. The changes are calculated from an average of five days prior to the storm to be compared with the data in this project.

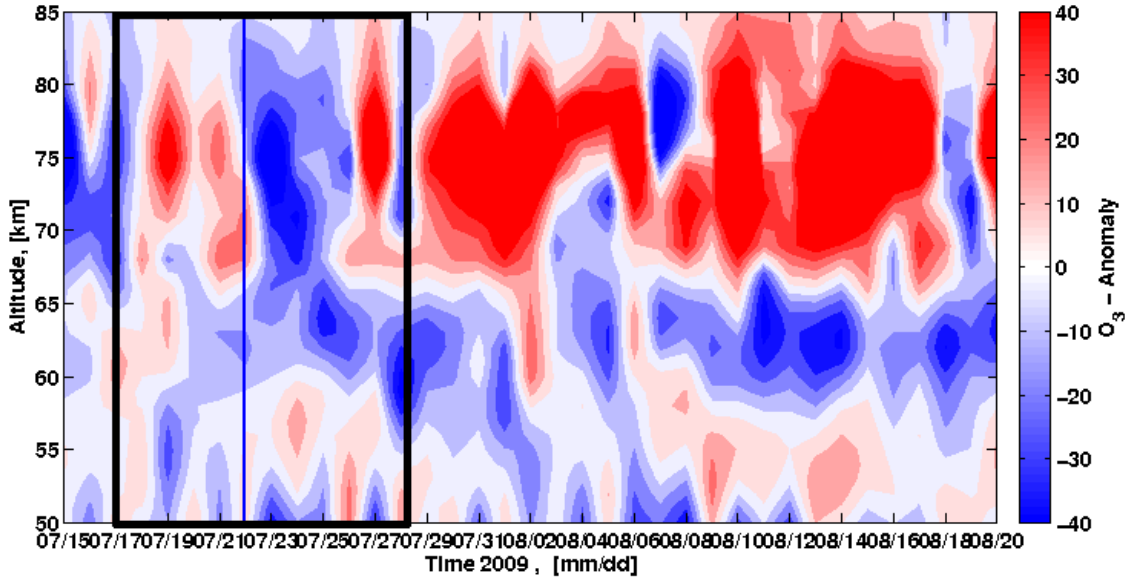


Figure 6.2: Changes of ozone over Troll station registered by a ground-based microwave radiometer in July-August 2009. Provided by Marianne Daae.

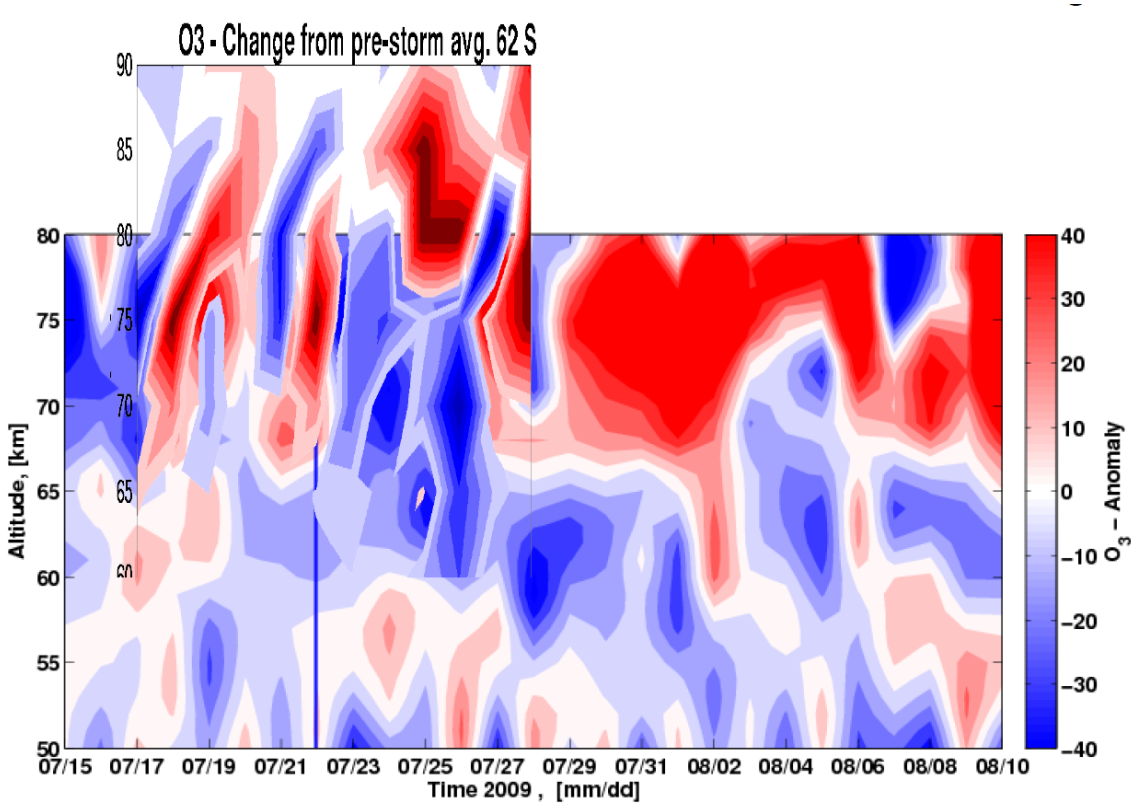


Figure 6.3: Changes of ozone over Troll station registered by a ground-based microwave radiometer in July-August 2009 compared to the time series of geomagnetic latitude $62^o$ S.

Comparison with figure 5.12 reveals good agreement in the ozone loss in the altitude range 60-80 Km for the days following the storm. The increased values of ozone at level 70-90 Km is also visible in both data sets. All in all it seems like ground-based and satellite observations are consistent, both showing an ozone loss of about 30-50% following the geomagnetic storm of the 22 of July.

The observed depletion of ozone following the moderate storm on the 22 July 2009, suggests that a weakening of ozone not only happens for very energetic solar events as reported by *Jackman et al.* [2001]; *Rohen et al.* [2005]; *Seppala et al.* [2006]. The increase/decrease in ozone is associated with a decrease/increase of OH in the days the storm lasts. The extent of the ozone and hydroxyl changes occur from geomagnetic latitudes greater than $60^o$ S extending into the polar cap.

Immediately after the storm a remarkable increase of ozone is observed above 80 Km remaining for four days and extending gradually to low geomagnetic latitudes which could be caused by $NO_x$.

This thesis shows that smaller EEP events can produce perturbations on the mesospheric ozone through a hydroxyl production increase. This topic should be studied more in depth since EEPs happen with greater frequency than the much more reviewed SEP events.

# Chapter 7

# Conclusion and future work

Ozone depletion following the storm on the 22 July 2009, was first observed from the ground-based microwave radiometer at Troll, Antarctica (-72$^o$ S, 2.5$^o$E, 1000m). In this thesis the ozone depletion has been further studied with $O_3$ and OH data retrieved from two low earth orbiting satellites (Odin and Aura).

Geographic maps of ozone over Antarctica at an altitude level of 72 Km showed decreases of up to 50% for the days following the storm. The ozone maps were plotted in geographic and geomagnetic coordinates to see if they matched the precipitation boundaries. Geographical variability of ozone and sparse satellite coverage made it difficult to observe storm effects on a latitudinal/longitudinal scale.

Zonal means of ozone, displayed depletion of up to 30-50% at altitudes below 80 Km for geomagnetic latitudes greater than 60$^o$. This depletion was most pronounced two days after the storm ceased, and the loss gradually descended in altitude and intensity, moving poleward. The storm created a large increase of ozone (50%) above 80 Km due to increased atomic oxygen and a decrease of hydroxyl production. OH zonal means showed an almost instantaneous increase on the 22 July 2009 for altitudes 70-75 Km and geomagnetic latitudes greater than 50$^o$. This increase peaked at the second day of the storm and then dropped in intensity as the storm ceased.

Comparison of the zonal means of $O_3$ and OH reveal high concordance between areas of rising hydroxyl and areas of ozone depletion, suggesting that the increase of OH during the storm is the main cause of $O_3$ depletion. The extent of the $O_3$ and OH changes occur from geomagnetic latitudes greater than 60$^o$ S and extend into the polar regions.

The altitude descent of the ozone depletion seen some days after the storm, cannot be caused by OH alone since the raised production vanishes quickly. The reason can be ionized-induced NO, that with its longer lifetime is transported downwards in the polar vortex causing catalytic destruction of ozone.

Time-series plots made for geomagnetic latitude 62 $^o$S reveal an immediate raise in

ozone concentrations at 75 Km height on the day of the storm followed by a descending loss for the four days that follow. The hydroxyl concentration increases in roughly the same altitudes, suggesting that the ozone depletion is connected to catalytic cycles with OH.

The time series plots were compared to ground-based data from a microwave radiometer located at Troll. The comparisons revealed good agreement for the ozone loss in the altitude range 60-80 Km in the days following the storm. Increased values of ozone at levels 70-90 Km were also visible in both data sets. All in all it seems like ground-based and satellite observations are consistent, both showing an ozone loss of about 30-50% following the geomagnetic storm of the 22 of July.

To get a deeper understanding on the ozone depletion effects of particle precipitation, suggestions for further work could be:

- Enhance the time series and study other events of similar characteristics with the goal to make a statistical analysis that confirms the findings.
- Gain more knowledge about the time and space distribution of the different types of energetic particles and their ionization effect. Arrive at a parametrization of energetic particles and their deposition in the atmosphere that can be included in models.
- Study the influence of particle precipitation on other species such as $NO_x$.
- In this work daily analysis with fixed sampling locations does not only reflect the particle precipitation and photolysis effects on ozone. The influence of planetary waves, tidal waves and other dynamical processes could also be taken into account. Due to the dynamic nature of the mesosphere-thermosphere, these mechanisms could be studied by models with a Lagrangian approach that follows a parcel in its motion

# References


Aikin, A., and H. Smith, Mesospheric constituent variations during electron precipitation events, *Journal of geophysical research*, *104*, 26, 1999.

Andrews, D., *An Introduction to Atmospheric Physics*, Cambridge University Press, 2000.

Barth, C., D. Rusch, R. Thomas, G. Mount, G. Rottman, G. Thomas, R. Sanders, and G. Lawrence, Solar Mesosphere Explorer: scientific objectives and results, *Geophysical research letters*, *10*(4), 237–240, 1983.

Brasseur, G., and S. Solomon, *Aeronomy of the Middle Atmosphere - Chemistry and Physics of the Stratosphere and Mesosphere*, Springer, 2005.

Buehler, S., P. Eriksson, T. Kuhn, A. von Engeln, and C. Verdes, Arts, the atmospheric radiative transfer simulator, *Journal of Quantitative Spectroscopy and Radiative Transfer*, *91*(1), 65–93, 2005.

Bychkov, V., G. Golubkov, and A. Nikitin, *The Atmosphere and Ionosphere: Dynamics, Processes and Monitoring*, Springer Verlag, 2010.

Chalmers University of Technology, S., Odin smr website, `http://odin.rss.chalmers.se/`, 2011.

Codrescu, M., T. Fuller-Rowell, R. Roble, and D. Evans, Medium energy particle precipitation influences on the mesosphere and lower thermosphere, *Journal of geophysical research*, *102*(A9), 19,977–19, 1997.

Daae, M., The effect of precipitating electrons on middle atmospheric ozone durig enhanced geomagnetic activity, project FY8902, 2010.

Eriksson, J., and F. Merino, On simulating passive observations of the middle atmosphere in the range 1-1000 GHz, *Dep. Radio and Space Science, Chalmers University, Goteborg*, *179*, 1997.

Eriksson, P., C. Jiménez, and S. Buehler, Qpack, a general tool for instrument simulation and retrieval work, *Journal of Quantitative Spectroscopy and Radiative Transfer*, *91*(1), 47–64, 2005.

Flynn, L., C. Seftor, J. Larsen, and P. Xu, The Ozone Mapping and Profiler Suite (OMPS), *NOAA Satellite and Information Services*, 2005.

Frisk, U., et al., The Odin satellite. I. Radiometer design and test, *Astronomy and Astrophysics*, *402*, L27–L34, 2003.

Froidevaux, L., J. Waters, W. Read, L. Elson, W. Read, D. Flower, and R. Jarnot, Coauthors, 1996: Validation of UARS Microwave Limb Sounder ozone measurements, *J. Geophys. Res*, *101*(10), 017–10, 1996.

Grenfell, J., R. Lehmann, P. Mieth, U. Langematz, and B. Steil, Chemical reaction pathways affecting stratospheric and mesospheric ozone, *Journal of geophysical research*, *111*(D17), D17,311, 2006.

Hartogh, P., C. Jarchow, G. Sonnemann, and M. Grygalashvyly, On the spatiotemporal behavior of ozone within the upper mesosphere/mesopause region under nearly polar night conditions, *Journal of Geophysical Research, USA*, *109*(D18), 17 pp. –, 2004.

Houghton, J., *Physics of atmospheres*, Cambridge University Press, 2002.

Jackman, C., R. McPeters, G. Labow, E. Fleming, C. Praderas, and J. Russell, Northern Hemisphere atmospheric effects due to the July 2000 solar proton event, *Geophys. Res. Lett*, *28*(15), 2883–2886, 2001.

Janssen, M., *Atmospheric remote sensing by microwave radiometry*, Wiley, 1993.

Jet Propulsion Laboratory, N., Microwave limb sounder website, `http://mls.jpl.nasa.gov/`, 2011a.

Jet Propulsion Laboratory, N., Molecular spectroscopy, `http://spec.jpl.nasa.gov/`, 2011b.

Kaufmann, M., O. Gusev, K. Grossmann, F. Martin-Torres, D. Marsh, and A. Kutepov, Satellite observations of daytime and nighttime ozone in the mesosphere and lower thermosphere, *Journal of geophysical research*, *108*(D9), 4272, 2003.

Kelly, M., The Earths Ionosphere, Int. Geophys. Ser., vol. 43, 1989.

Kleinknecht, N., Millimeter-wave radiometer observations of middle atmospheric ozone in antarctica, Master's thesis, Technische Universität München, 2010.

Livesey, N. e. a., Earth observing system microwave limb sounder, version 3.3 level 2 data quality and description document, *Tech. rep.*, Jet Propulsion Laboratory, California, technical report D-33509, 2011.

Maeda, K., and A. Aikin, Variations of polar mesospheric oxygen and ozone during auroral events, *Planetary and Space Science*, *16*(4), 371–384, 1968.

Maini, A., and V. Agrawal, *Satellite technology: principles and applications*, Wiley, 2011.

Marsh, D., A. Smith, G. Brasseur, M. Kaufmann, and K. Grossmann, The existence of a tertiary ozone maximum in the high-latitude middle mesosphere, *Geophysical Research Letters, USA*, *28*(24), 4531 – 4, 2001.

Merino, F. e. a., *Aeronomy Level 2 data products. Version 1.2*, 2003.

NASA, Aura mission website, `http://www.nasa.gov/mission_pages/aura/main/index.html`, 2011.

NOAA, N. G. D. C., Hourly equatorial dst values (real-time) july 2009, `http://satdat.ngdc.noaa.gov/sem/poes/data/plots/maps/png/2009/07/cylindrical/`, 2010.

Olberg, M., et al., The Odin satellite, *Astronomy and Astrophysics*, *402*(3), 35–38, 2003.

Rodgers, C., Retrieval of atmospheric temperature and composition from measurements of thermal radiation, *Reviews of Geophysics and Space Physics*, *14*(4), 609–624, 1976.

Rohen, G., et al., Ozone depletion during the solar proton events of October/November 2003 as seen by SCIAMACHY, *J. Geophys. Res*, *110*, A09S39, 2005.

Rostoker, G., Geomagnetic indices, *Reviews of Geophysics*, *10*(4), 935–950, 1972.

Saetre, C., J. Stadsnes, H. Nesse, A. Aksnes, S. Petrinec, C. Barth, D. Baker, R. Vondrak, and N. Oestgaard, Energetic electron precipitation and the NO abundance in the upper atmosphere: A direct comparison during a geomagnetic storm, *J. Geophys. Res*, *109*(A9), 2004.

Salby, M., *Fundamentals of Atmospheric Physics*, Academic Press, 1995.

Seppala, A., P. Verronen, V. Sofieva, J. Tamminen, E. Kyrola, C. Rodger, and M. Clilverd, Destruction of the tertiary ozone maximum during a solar proton event, *Geophys. Res. Lett*, *33*, L07,804, 2006.

Sofieva, V., and et al., Spatio-temporal observations of the tertiary ozone maximum, *Atmospheric Chemistry and Physics*, *9*(13), 2009.

Solomon, S., P. Crutzen, and R. Roble, Photochemical coupling between the thermosphere and the lower atmosphere 1. Odd nitrogen from 50 to 120 km, *Journal of Geophysical Research*, *87*(C9), 7206–7220, 1982.

Sonnemann, G., M. Grygalashvyly, P. Hartogh, and C. Jarchow, Behavior of mesospheric ozone under nearly polar night conditions, *Advances in Space Research, UK*, *38*(11), 2402 – 7, 2006.

Sonnemann, G., P. Hartogh, C. Jarchow, M. Grygalashvyly, and U. Berger, On the winter anomaly of the night-to-day ratio of ozone in the middle to upper mesosphere in middle to high latitudes, *Advances in Space Research, UK*, *40*(6), 846 – 54, 2007.

Swedish Space Corporation, S., Odin ssc website, `http://ssc.se/products-services/satellite-systems/satellite-missions/odin-1`, 2011.

Tarantola, A., *Inverse problem theory and methods for model parameter estimation*, Society for Industrial Mathematics, 2005.

Todaro, R., Stratospheric ozone - an electronic textbook, `http://www.ccpo.odu.edu/~lizsmith/SEES/ozone/oz_class.htm`, 2003.

Urban, J., P. Baron, N. Lautie, N. Schneider, K. Dassas, P. Ricaud, and J. De La Noe, Moliere (v5): A versatile forward-and inversion model for the millimeter and submillimeter wavelength range, *Journal of Quantitative Spectroscopy and Radiative Transfer*, *83*(3-4), 529–554, 2004a.

Urban, J., et al., The northern hemisphere stratospheric vortex during the 2002–03 winter: Subsidence, chlorine activation and ozone loss observed by the odin sub-millimetre radiometer, *Geophysical research letters*, *31*(7), L07,103, 2004b.

Verronen, P., A. Seppala, E. Kyrola, J. Tamminen, H. Pickett, and E. Turunen, Production of odd hydrogen in the mesosphere during the January 2005 solar proton event, *Geophys. Res. Lett*, *33*, L24,811, 2006.

Waters, J., et al., The earth observing system microwave limb sounder (EOS MLS) on the Aura satellite, *Geoscience and Remote Sensing, IEEE Transactions on*, *44*(5), 1075–1092, 2006.

Wayne, R., *Chemistry of atmospheres*, Oxford University Press, 2000.

WDC for Geomagnetism, K., Hourly equatorial dst values (real-time) july 2009, `http://wdc.kugi.kyoto-u.ac.jp/dst_realtime/200907/index.html`, 2009a.

WDC for Geomagnetism, K., Transformation of coordinates., `http://wdc.kugi.kyoto-u.ac.jp/igrf/gggm/index.html`, 2009b.

# Appendix A

# Zonal Means

# A.1 O3

## A.1.1 Pre-storm values

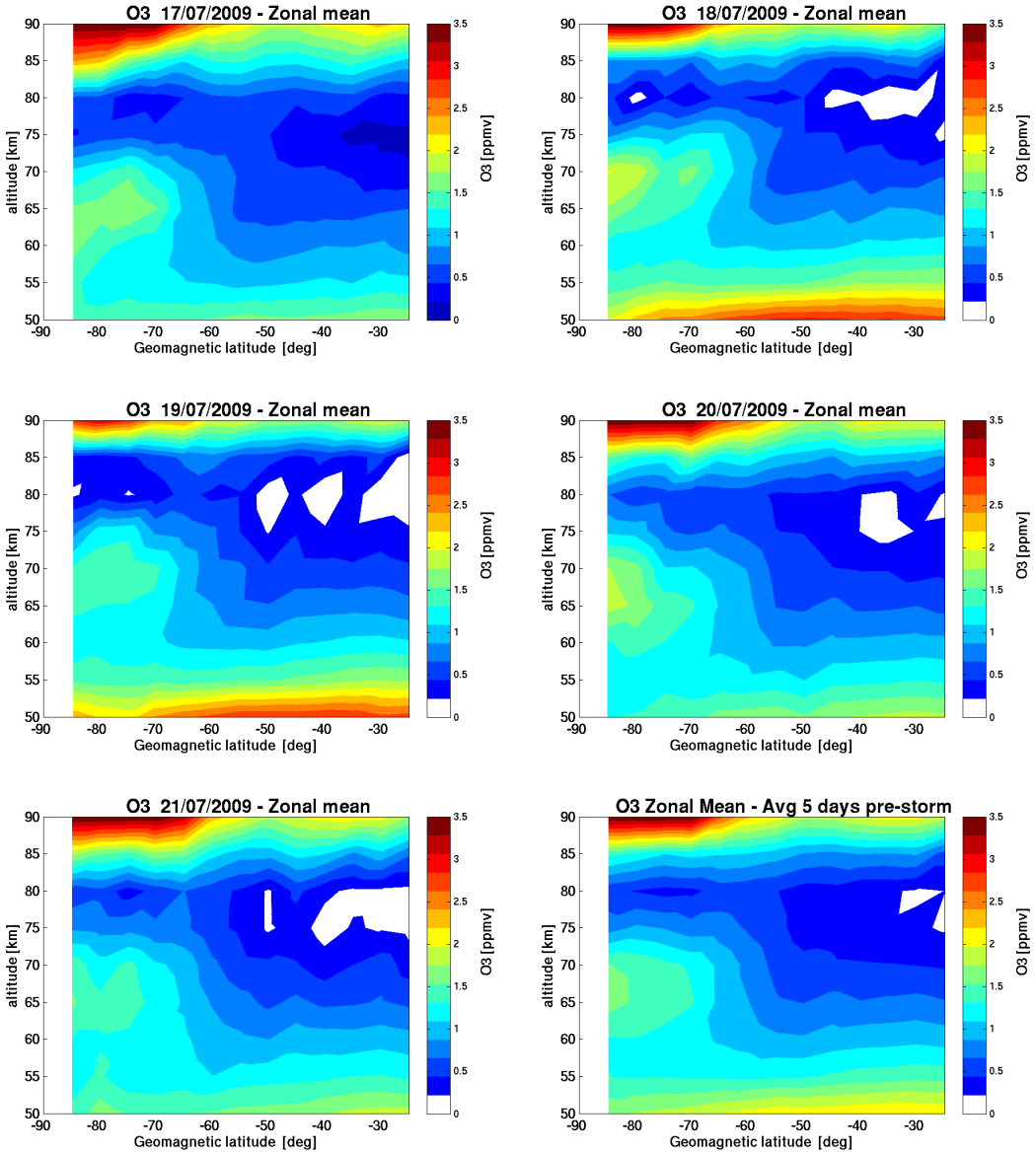


Figure A.1: O3 daily zonal means (17-21 July 2009) in ppmv before the storm and average of the five days

### A.1.2 Post-storm values

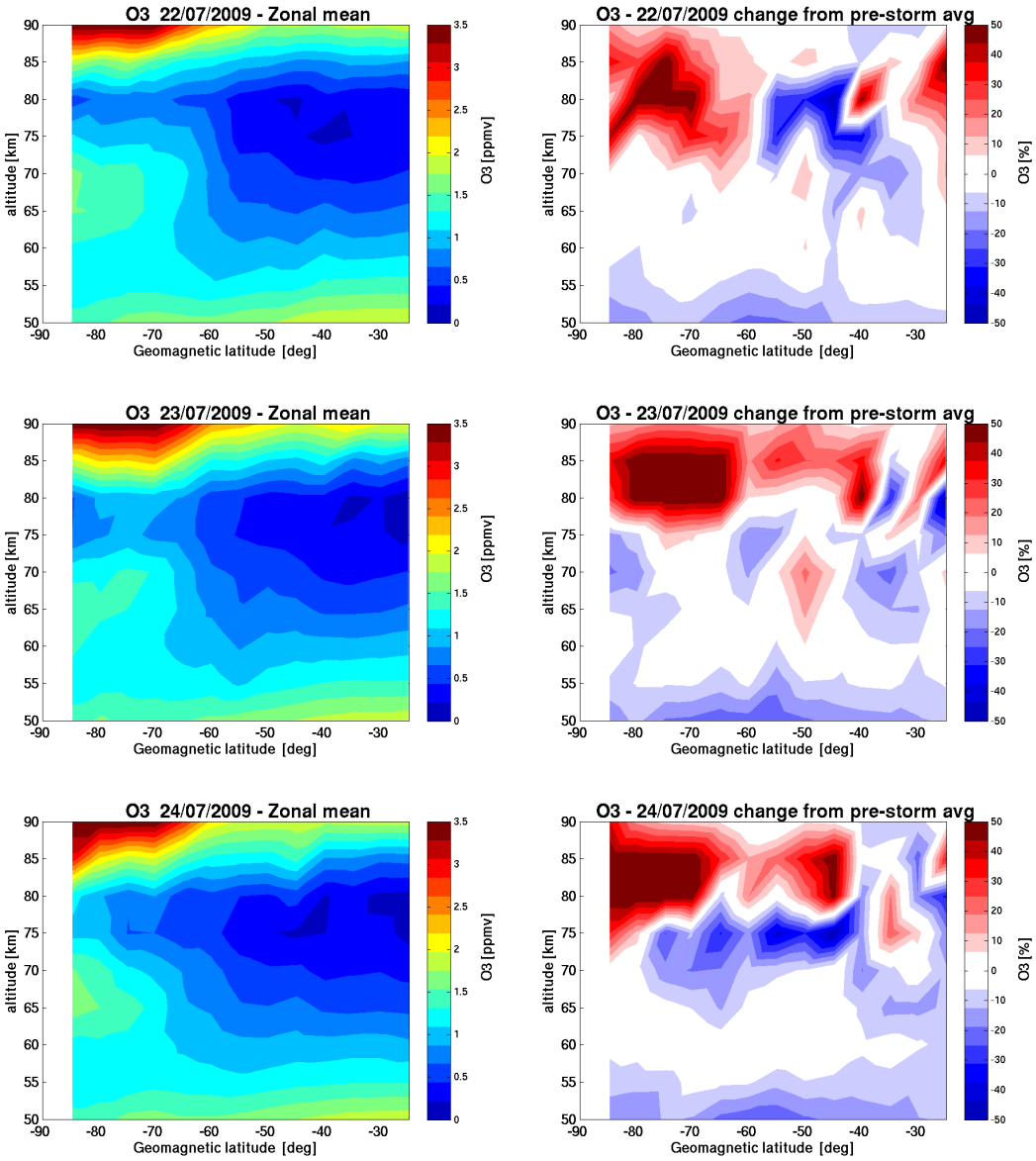


Figure A.2: O3 daily zonal means (22-24 July 2009) in ppmv after the storm and percentage change from the five day average pre-storm

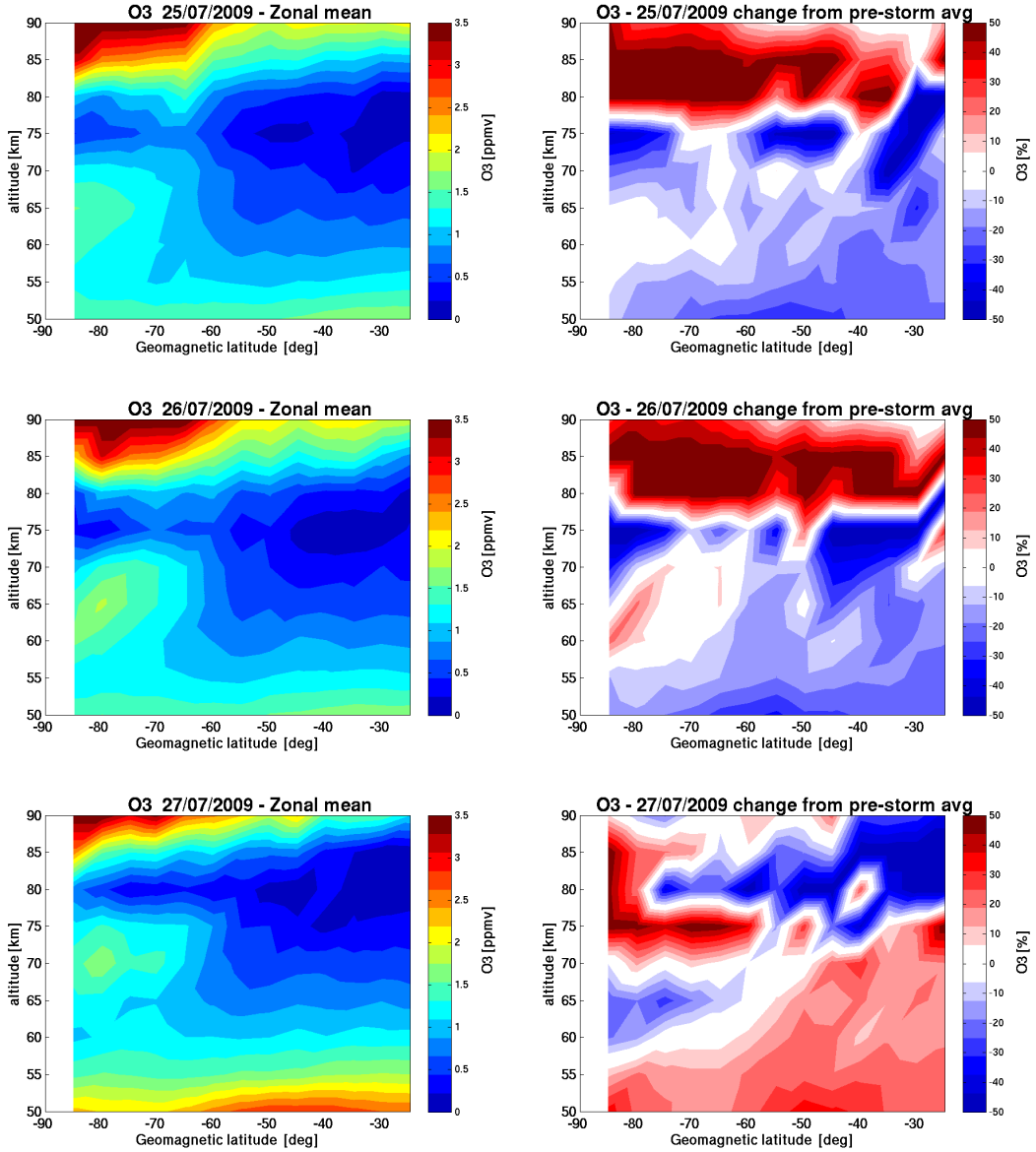


Figure A.3: O3 daily zonal means (25-27 July 2009) in ppmv after the storm and percentage change from the five day average pre-storm

## A.2 OH

### A.2.1 Pre-storm values

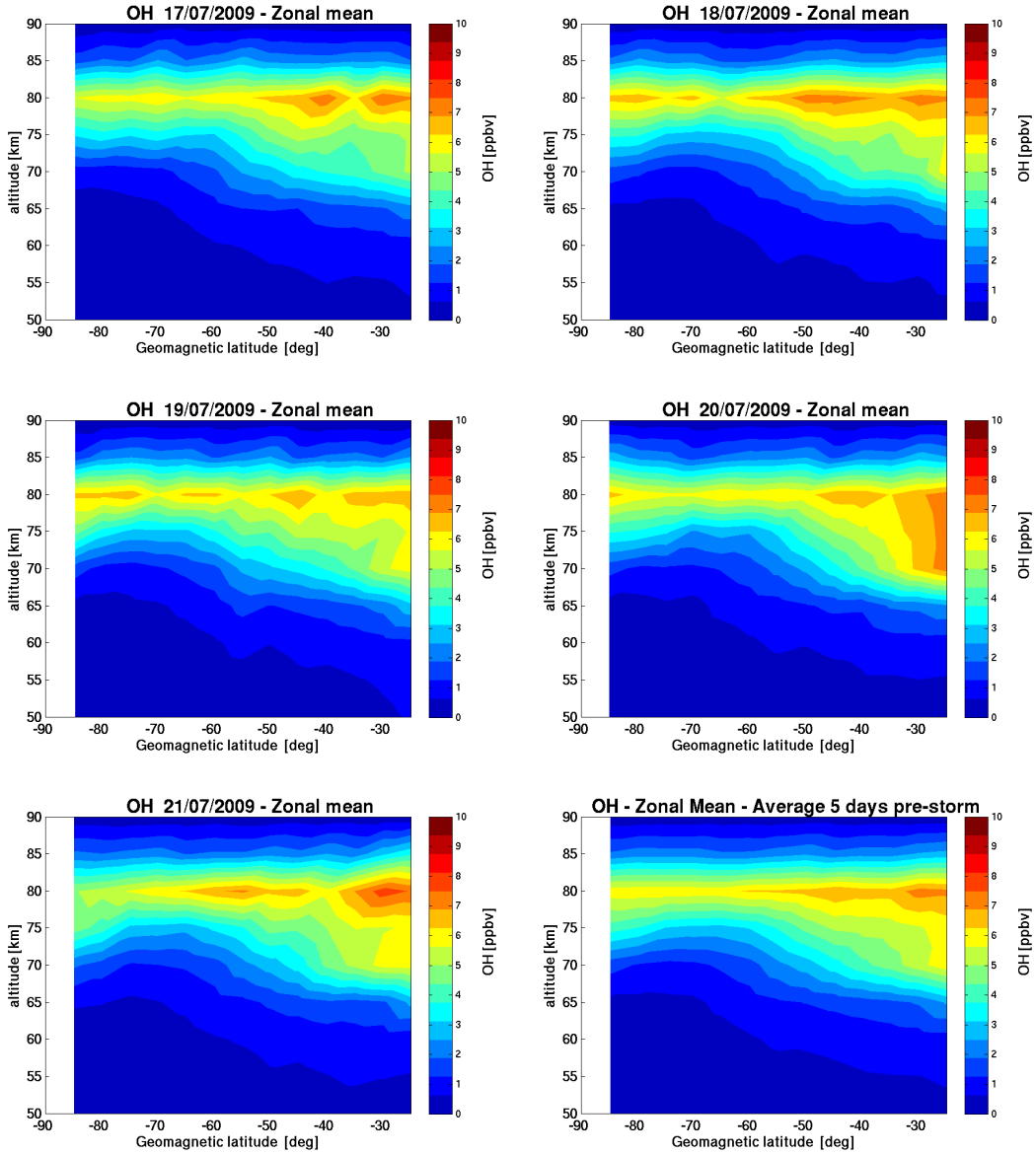


Figure A.4: OH daily zonal means (17-21 July 2009) in ppbv before the storm and average of the five days

### A.2.2 Post-storm values

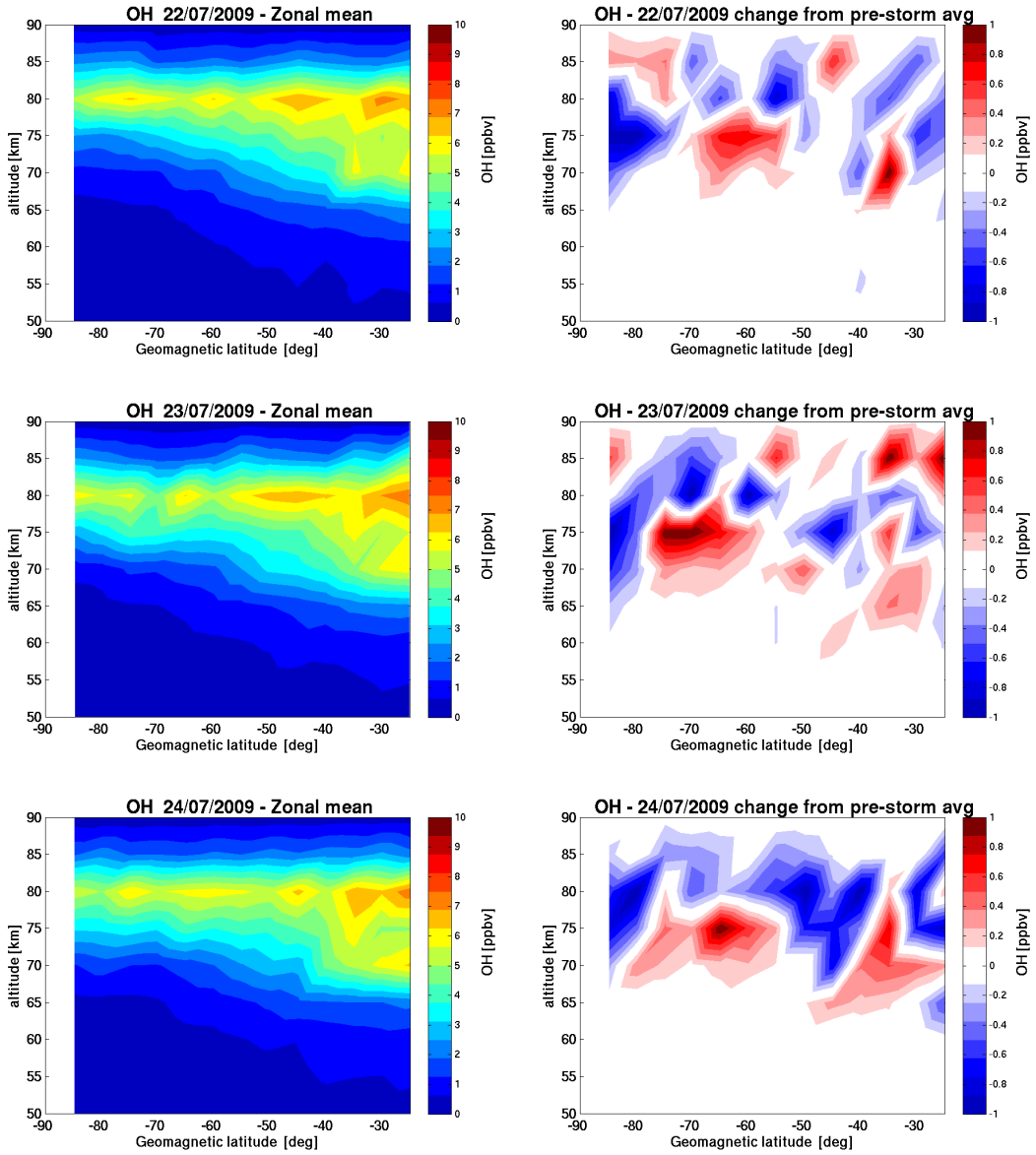


Figure A.5: OH daily zonal means (22-24 July 2009) in ppbv after the storm and absolute change in ppbv from the five day average pre-storm

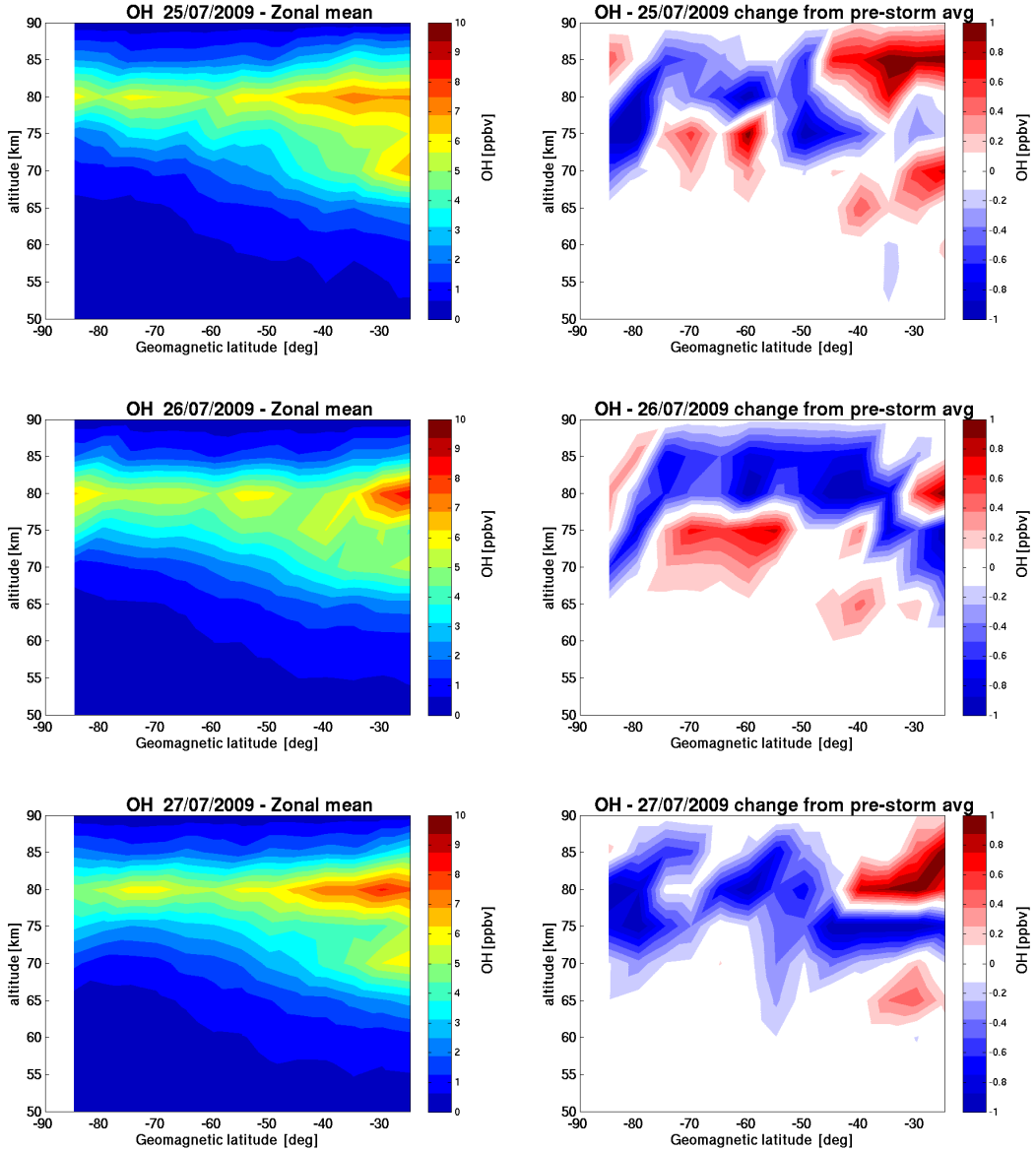


Figure A.6: OH daily zonal means (25-27 July 2009) in ppbv after the storm and absolute change in ppbv from the five day average pre-storm

# Appendix B

# Time series

## B.1 O3 and OH

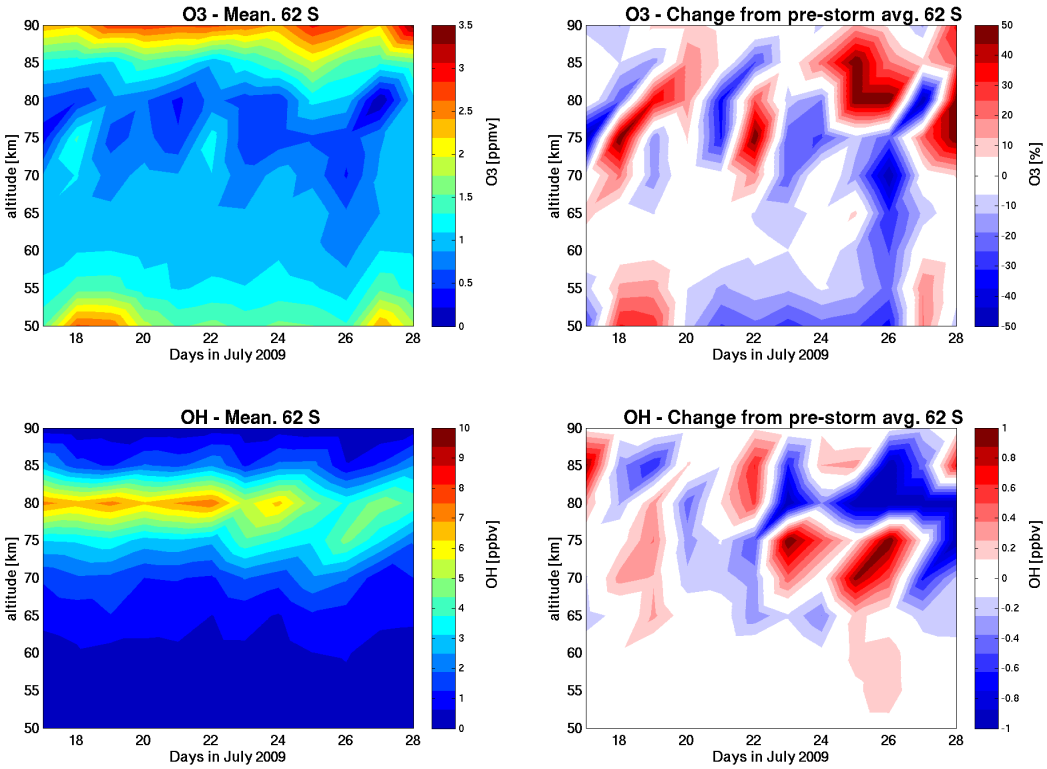


Figure B.1: On first column daily means (17-28 July 2009) of O3 and OH at geomagnetic latitude $62^o$ S plotted in time. Second column shows difference plots from the five day average pre-storm (17-21 July 2009) in percent (O3) and absolute change (OH).

# Appendix C

# SH polar and cylindrical ozone maps

## C.1 Geomagnetic coordinates

### C.1.1 Pre-storm values

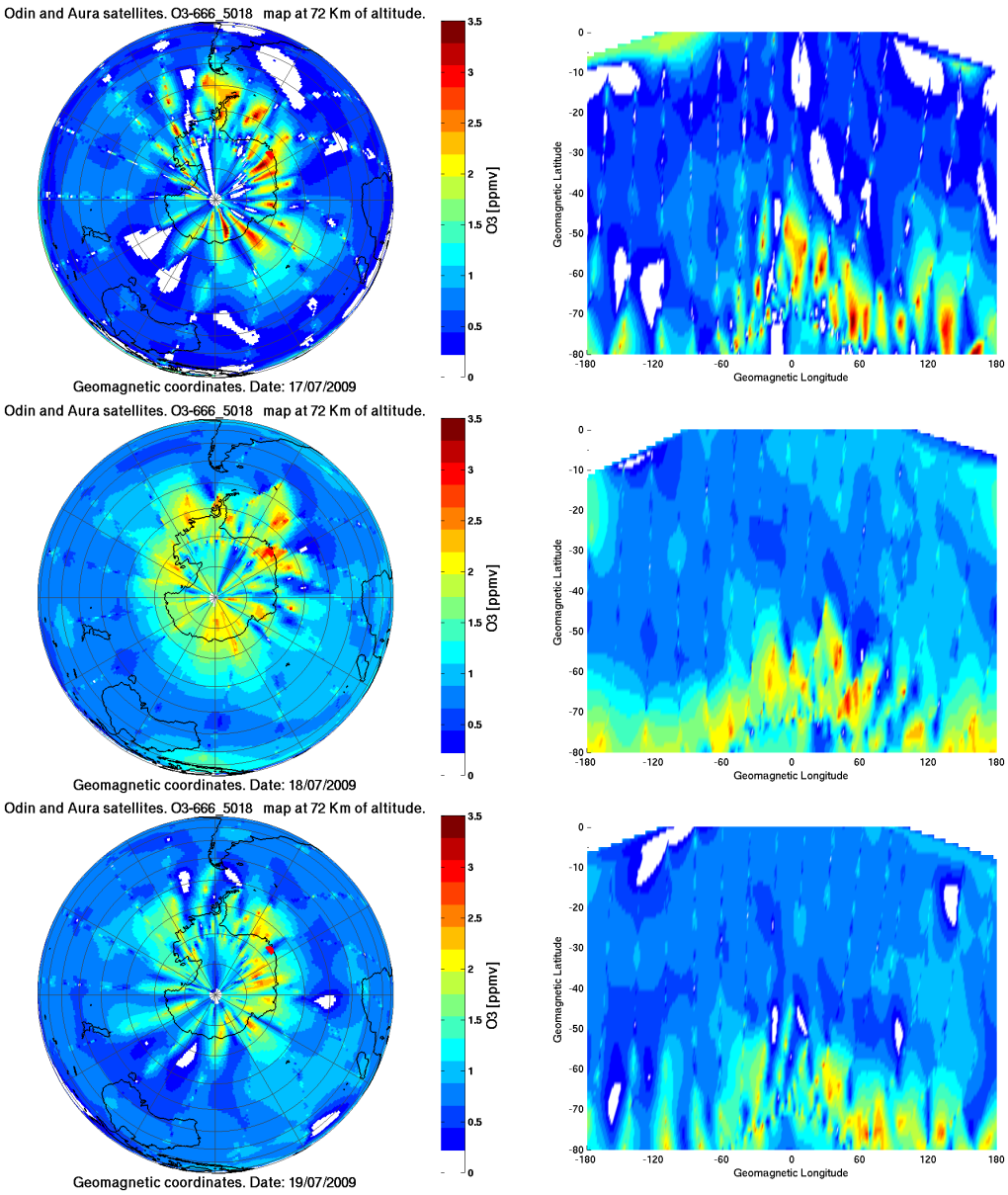


Figure C.1: Daily polar and cylindrical ozone maps (17-19 July 2009) in ppmv at altitude 72 Km. All plots are in geomagnetic coordinates and before the storm

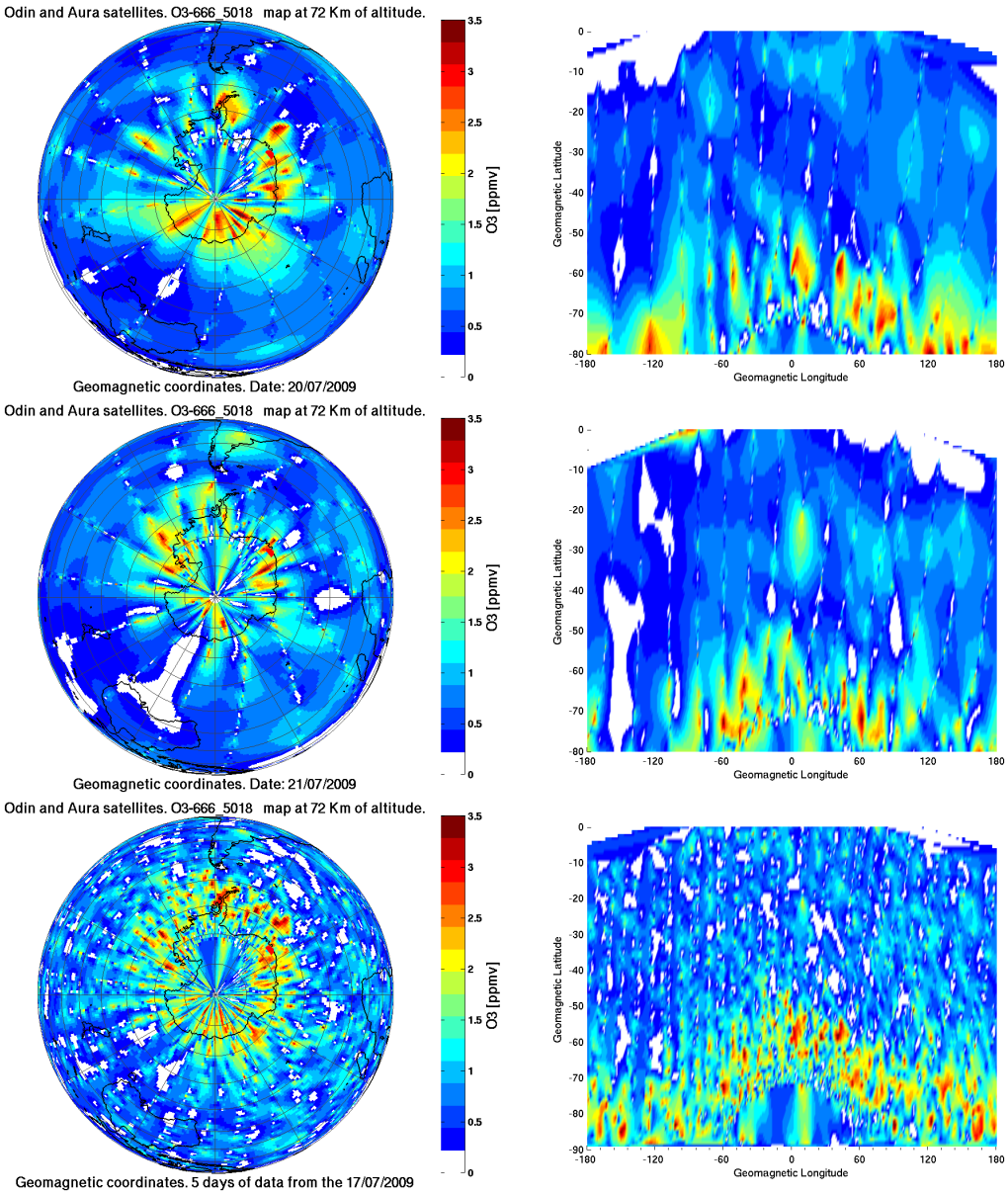


Figure C.2: Daily polar and cylindrical ozone maps (20-21 July 2009) in ppmv at altitude 72 Km and data of five days (17-21 July 2009) in one plot. All plots are in geomagnetic coordinates and before the storm

### C.1.2 Post-storm values

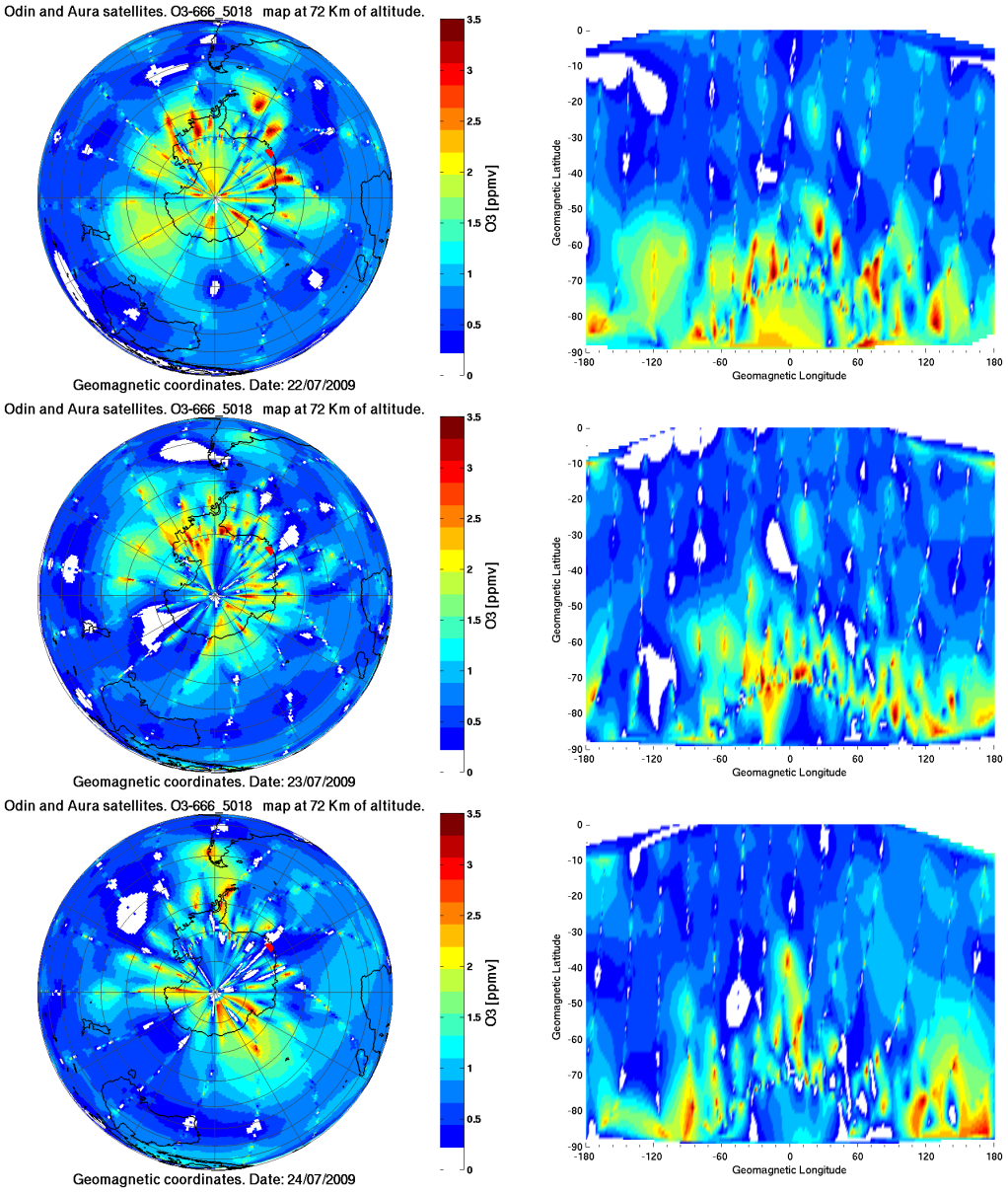


Figure C.3: Daily polar and cylindrical ozone maps (22-24 July 2009) in ppmv at altitude 72 Km. All plots are in geomagnetic coordinates and after the storm

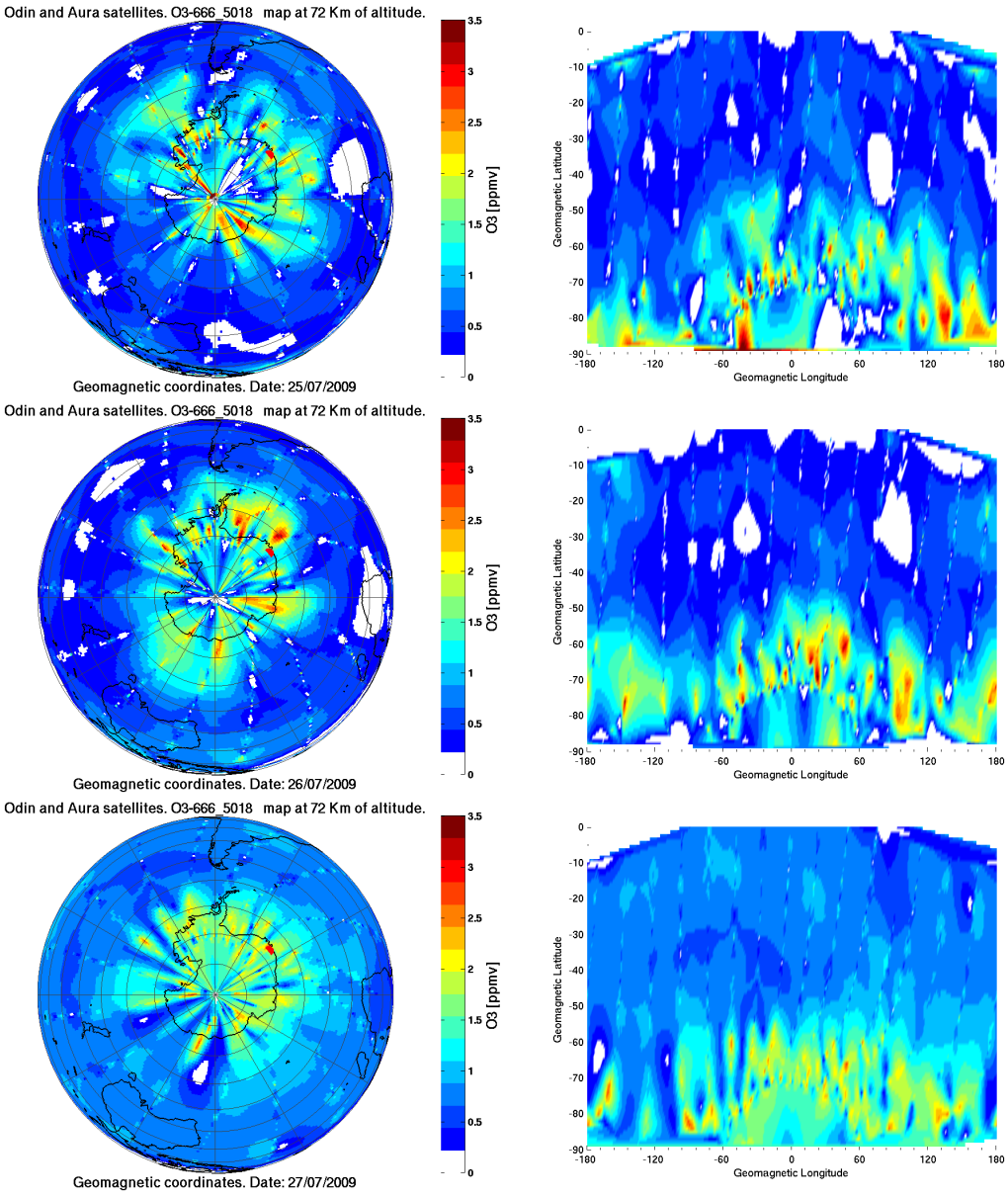


Figure C.4: Daily polar and cylindrical ozone maps (25-27 July 2009) in ppmv at altitude 72 Km. All plots are in geomagnetic coordinates and after the storm

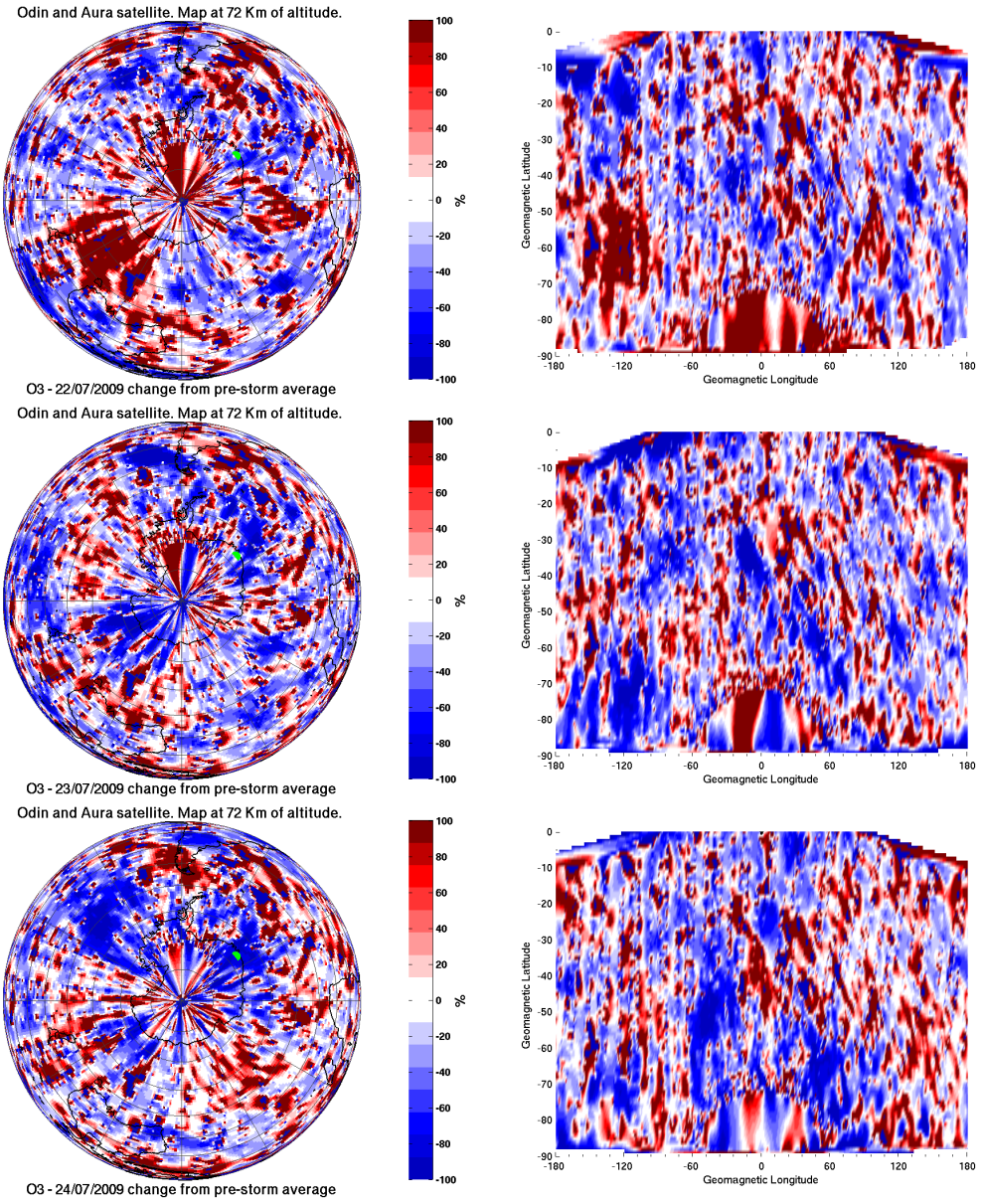


Figure C.5: Daily polar and cylindrical ozone maps (22-24 July 2009) in percentage change from the five day average pre-storm at altitude 72 Km. All plots are in geomagnetic coordinates and after the storm

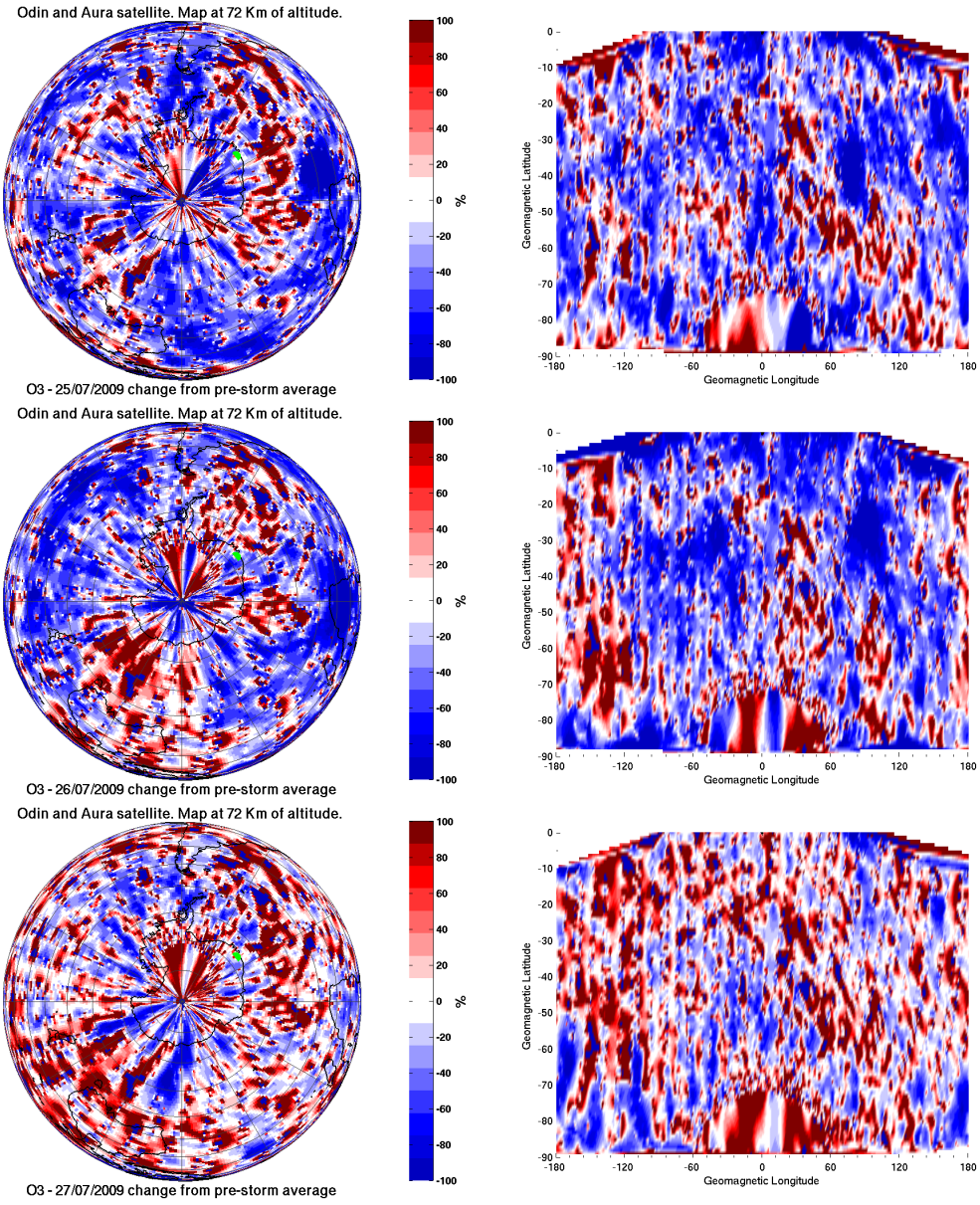


Figure C.6: Daily polar and cylindrical ozone maps (25-27 July 2009) in percentage change from the five day average pre-storm at altitude 72 Km. All plots are in geomagnetic coordinates and after the storm

## C.2 Geographic coordinates

### C.2.1 Pre-storm values

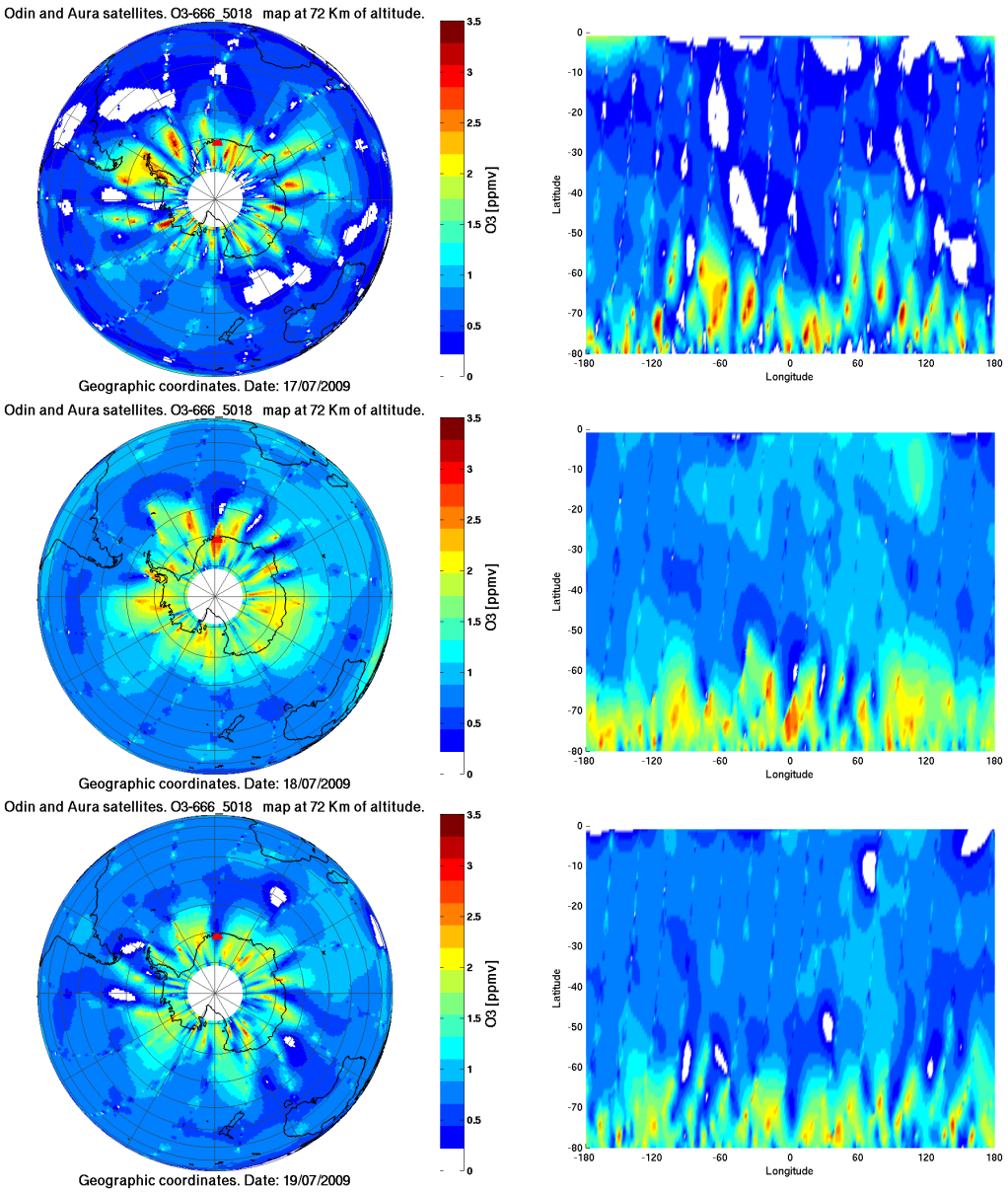


Figure C.7: Daily polar and cylindrical ozone maps (17-19 July 2009) in ppmv at altitude 72 Km. All plots are in geographic coordinates and before the storm

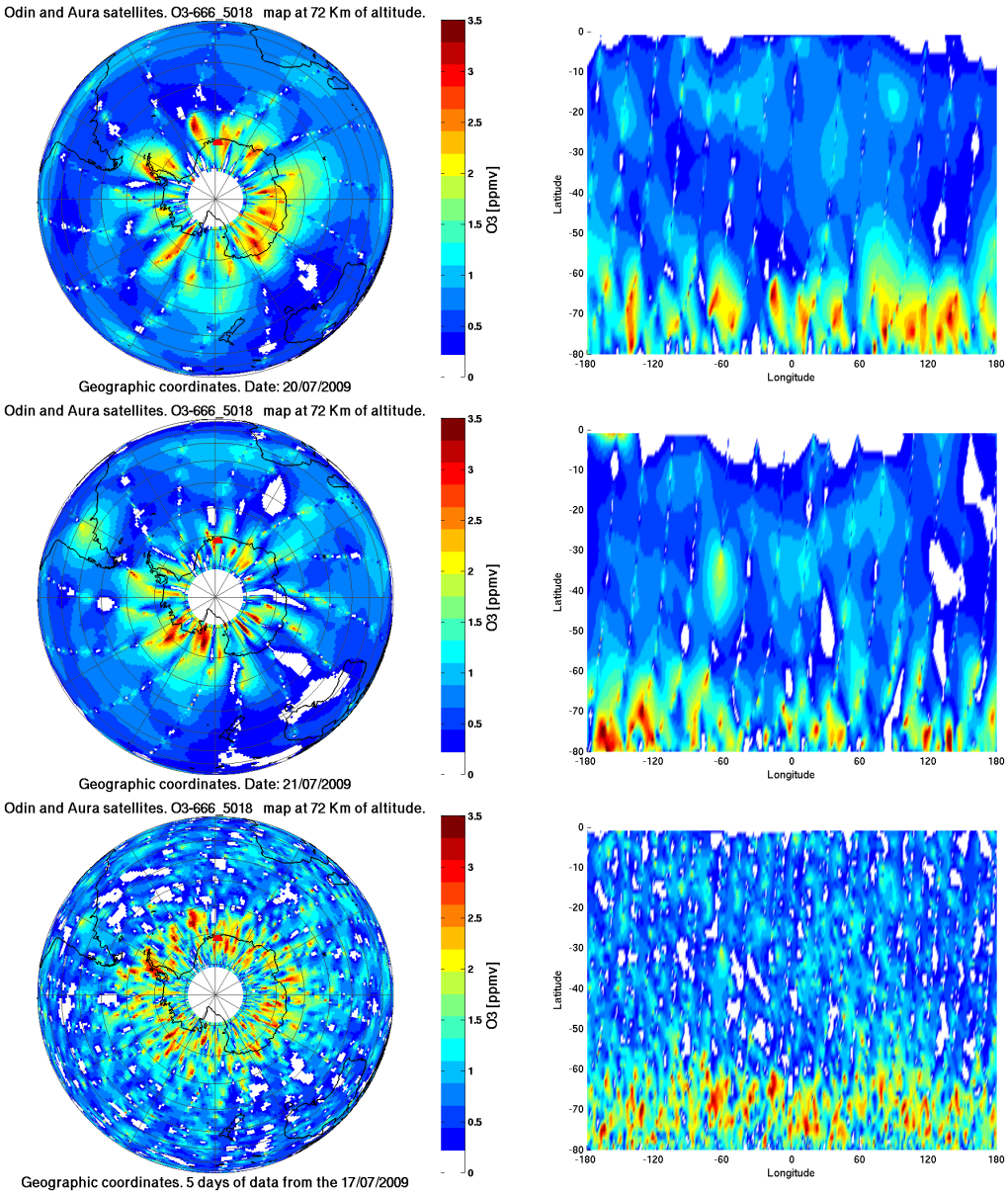


Figure C.8: Daily polar and cylindrical ozone maps (20-21 July 2009) in ppmv at altitude 72 Km and data of five days (17-21 July 2009) in one plot. All plots are in geographic coordinates and before the storm

### C.2.2 Post-storm values

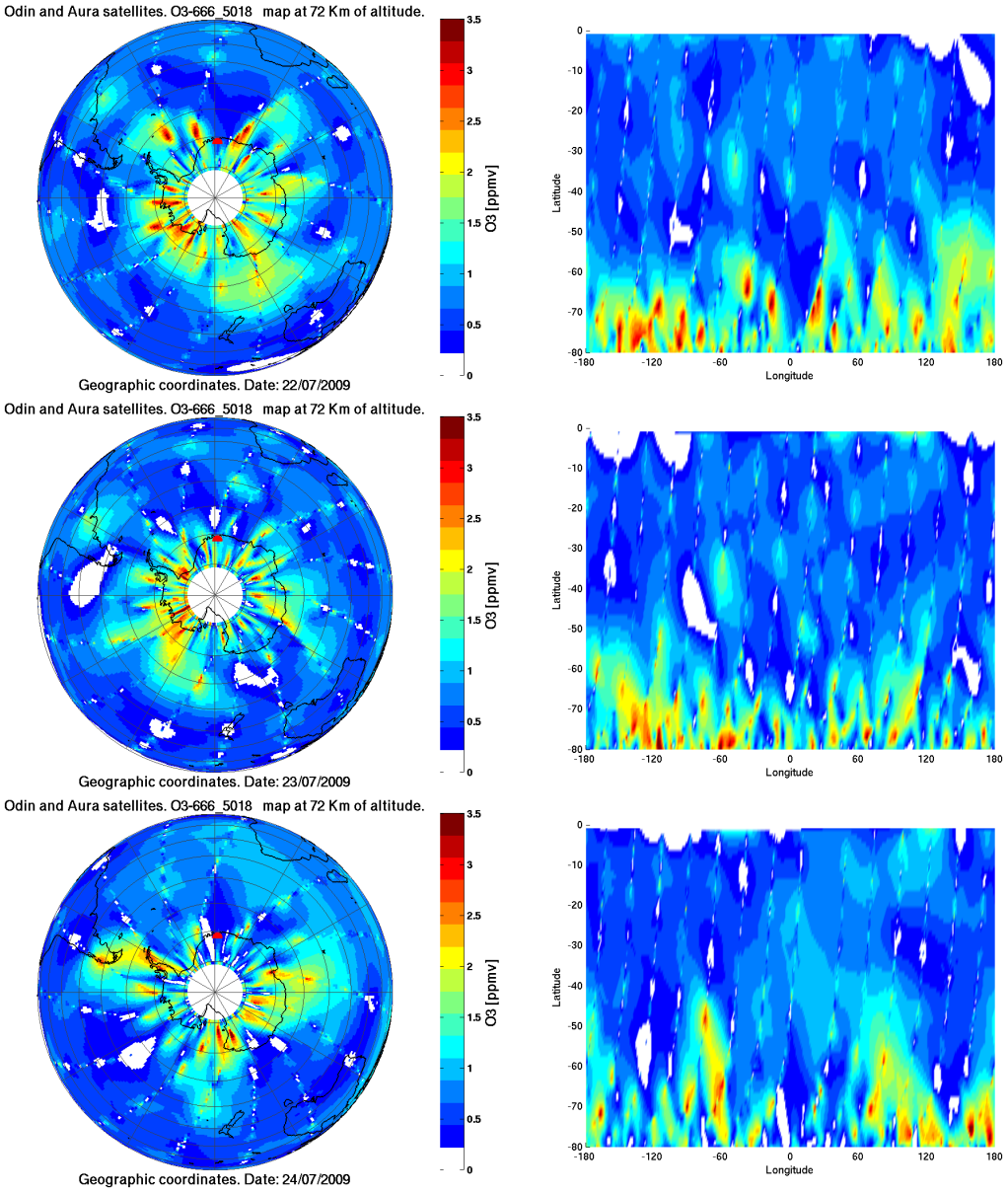


Figure C.9: Daily polar and cylindrical ozone maps (22-24 July 2009) in ppmv at altitude 72 Km. All plots are in geographic coordinates and after the storm

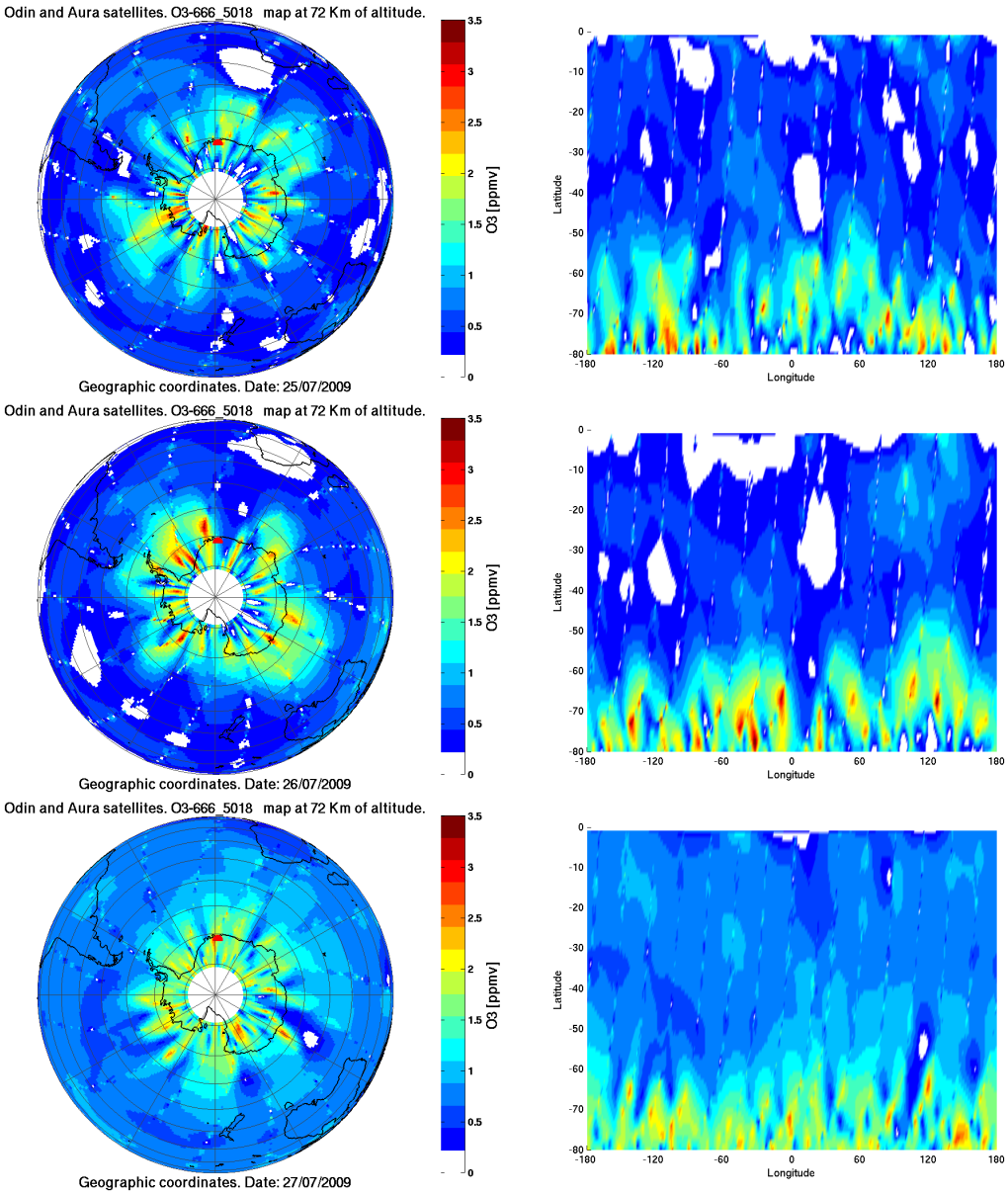


Figure C.10: Daily polar and cylindrical ozone maps (25-27 July 2009) in ppmv at altitude 72 Km. All plots are in geographic coordinates and after the storm